# DEVELOPMENT OF SOFTWARE TOOLS FOR IMPROVED $^{1}$H MAGNETIC RESONANCE SPECTROSCOPIC IMAGING

by

**Sevim Cengiz**

B.S., in Biomedical Engineering, Erciyes University, 2013

M.S., in Biomedical Engineering, Boğaziçi University, 2016

Submitted to the Institute of Biomedical Engineering

in partial fulfillment of the requirements

for the degree of

Doctor

of

Philosophy

Boğaziçi University

2022

# ACKNOWLEDGEMENTS

This study would not have been possible without the help of my advisor, Assoc. Prof. Dr. Esin Öztürk Işık, in many ways. I would like to thank Dr. Öztürk-Işık for all the help and advice, for all the patience, and for giving me this opportunity to study on development of software tools for improved $^{1}$H magnetic resonance spectroscopic imaging, which also helped me improve myself, gain knowledge, and widen my horizons. Moreover, I would like to thank my thesis committee Assoc. Prof. Dr. Maria Valdes Hernandez, Prof. Dr. İbrahim Hakan Gürvit, Prof. Dr. Bora Garipcan, and Prof. Dr. Ahmet Ademoğlu for their encouraging comments.

I am also thankful to my lovely spouse, Ilter, for all the support he gave me during this period. I'm also thankful to my son, Tony Ilker Cengiz, and my daughter, Elisa Cengiz, for being my sunshine to find my way when I was lost. My mom, Hatice Nalcaci, my dad, Ahmet Nalcaci, my brother, Osman Nalcaci, my-mother-in-law, Neriman Cengiz, my-father-in-law, Sezai Cengiz, and my-brother-in-law, Yasin Cengiz all supported me to take care of my kids while I was busy with my PhD work. I would like to also extend my gratitude to my colleagues, Dilek Betul Arslan, Muhammed Yildirim, Abdullah Bas, Asim Samli, Gokce Hale Hatay, and Sena Azamat for their guidance and friendship.

This study was supported by TÜBİTAK 1001 grant #115S219, Istanbul University Scientific Research Projects Unit project #1567/42362, and Bogazici University BAP 10844SUP grant.

# ACADEMIC ETHICS AND INTEGRITY STATEMENT

I, Sevim Cengiz, hereby certify that I am aware of the Academic Ethics and Integrity Policy issued by the Council of Higher Education (YÖK) and I fully acknowledge all the consequences due to its violation by plagiarism or any other way.

Name :

Signature:

Date:

# ABSTRACT

## DEVELOPMENT OF SOFTWARE TOOLS FOR IMPROVED $^{1}$H MAGNETIC RESONANCE SPECTROSCOPIC IMAGING

Proton magnetic resonance spectroscopic imaging ($^{1}$H-MRSI) provides a non-invasive, spatially resolved evaluation of brain metabolism. In the first part of this study, an open-source data analysis software, which includes modules for visualization of raw $^{1}$H-MRSI data and LCModel outputs, chemical shift correction, tissue fraction calculation, metabolite map production, and registration onto standard MNI152 brain atlas while providing automatic spectral quality control, is presented. In the second part of this study, we investigated metabolic changes of mild cognitive impairment in Parkinson's disease (PD-MCI) using $^{1}$H-MRSI data. This could be summarized mainly as 'posterior cortical metabolic changes' related with cognitive dysfunction. In the last part of this thesis, the spatial resolution of $^{1}$H-MRSI images were increased using super resolution convolutional neural networks (SRCNN) and enhanced deep residual networks for single image super-resolution (EDSR) models trained with the anatomical MR images. Our results indicated that deep learning based super resolution models would contribute to reconstructing higher resolution $^{1}$H-MRSI. This thesis contributed to the literature in terms of developing Oryx-MRSI, which provides an unprecedented detailed data analysis pipeline for $^{1}$H-MRSI, identifying metabolic correlates of PD-MCI, which might aid the clinicians for the diagnosis of MCI, and implementing deep learning based super resolution approaches that might increase the spatial resolution of $^{1}$H-MRSI.

**Keywords:** Parkinson's disease, mild cognitive impairment, proton magnetic resonance spectroscopic imaging, super resolution, deep learning, convolutional neural networks, open-source software.

# ÖZET

## İYİLEŞTİRİLMİŞ $^1$H MANYETİK REZONANS SPEKTROSKOPİK GÖRÜNTÜLEME İÇİN YAZILIM ARAÇLARININ GELİŞTİRİLMESİ

Proton manyetik rezonans spektroskopik görüntüleme ($^1$H-MRSG), beyin metabolizmasının invazif olmayan, uzamsal olarak çözümlenmiş bir değerlendirmesini sağlar. Bu çalışmanın ilk bölümünde, ham $^1$H-MRSG verilerinin ve LCModel çıktılarının görselleştirilmesi, kimyasal kayma düzeltme, doku fraksiyonu hesaplaması, metabolit haritası üretimi ve otomatik spektral kalite kontrolü sağlayarak MN152 beyin atlasına registrasyon yapan açık kaynaklı bir veri analiz yazılımı sunulmaktadır. Bu çalışmanın ikinci bölümünde, $^1$H-MRSG verileri kullanarak Parkinson hastalığında hafif kognitif bozukluğun (PH-HKB) metabolik değişikliklerini araştırdık. Bu bilişsel işlev bozukluk ile ilgili 'posterior kortikal metabolik değişiklikler' olarak özetlenebilir. Bu tezin son bölümünde, $^1$H-MRSG görüntülerinin uzamsal çözünürlüğü süper çözünürlüklü evrişimli sinir ağlarının (SRCNN) ve tek görüntü süper cözünürlük için gelişmiş derin artık ağların (EDSR) kullanılarak artırıldı. Sonuçlarımız, derin öğrenme tabanlı süper çözünürlüklü modellerin, daha yüksek çözünürlüklü $^1$H-MRSG'nin yeniden yapılandırılmasına katkıda bulunacağını gösterdi. Bu tez, $^1$H-MRSG için benzeri görülmemiş ayrıntılı bir veri analiz hattı sağlayan Oryx-MRSI'ın geliştirilmesi, klinisyenlere HKB tanısı için yardımcı olabilecek PD-HKB'nin metabolik bağlantılarını tanımlayan ve $^1$H-MRSG'nin uzamsal çözünürlüğünü artırabilecek derin öğrenme tabanlı süper çözünürlük yaklaşımlarının uygulanması açısından literatüre katkıda bulunmuştur.

**Anahtar Sözcükler:** Parkinson hastalığı, hafif kognitif bozukluk, proton manyetik rezonans spektroskopik görüntüleme, süper çözüünürlük, derin öğrenme, konvolüsyonel sinir ağları, açık kaynak yazılım.

# TABLE OF CONTENTS

# LIST OF FIGURES

# LIST OF TABLES

# LIST OF SYMBOLS

| | |
|---|---|
| $\Delta$E | Energy Difference |
| $\Delta$x | Chemical Shift Amount |
| $B_0$ | Magnetic Field Strength |
| $BW_x$ | Bandwidth of RF Excitation Pulse |
| C | Metabolite Concentration |
| $C_0$ | Initial Metabolite Concentration |
| $f_0$ | Larmor Frequency |
| $G_x$ | Gradient Strength |
| h | Planck Constant |
| J | Joule |
| K | Boltzmann's Constant |
| $N_{up}$ | Spin Numbers Aligned to $B_0$ |
| $N_{down}$ | Spin Numbers Aligned Anti-paralel to $B_0$ |
| $T_1$ | Spin-Lattice Relaxation Time |
| $T_2$ | Spin-Spin Relaxation Time |
| $\gamma$ | Gyromagnetic Ratio |
| $\omega$ | Reference Compound |
| $\omega_{ref}$ | Frequency of Reference Compound |
| $\sigma$ | Chemical Shift |
| $V_{CSF}$ | Volume Fraction of the CSF |
| $X_l$ | Length of the Voxel |

# LIST OF ABBREVIATIONS

| | |
|---|---|
| 3D | Three-dimensional |
| A | Anterior |
| AC | Anterior Commissure |
| ACC | Anterior Cingulate Cortex |
| ACE-R | Addenbrooke's Cognitive Examination Revised |
| AD | Alzheimer's Disease |
| Ala | Alanine |
| ANOVA | Analysis of Variance |
| AP | Anterior Posterior |
| ASL | Arterial Spin Labeling |
| Asp | Aspartate |
| CBF | Cerebral Blood Flow |
| CC | Cranial-Caudal |
| Cho | Choline |
| CON | Cingula-Opercular Networks |
| Cr | Creatine |
| CRLB | Cramer-Rao Lower Bounds |
| CSF | Cerebrospinal Fluid |
| CT | Computed Tomography |
| dACC | Dorsal Anterior Cingulate Cortex |
| DICOM | Digital Imaging and Communications in Medicine |
| DMN | Default Mode Network |
| DTI | Diffusion Tensor Imaging |
| EDSR | Enhanced Deep Residual Networks for Single Image Super-Resolution |
| EMCL | Extramyocellular |
| F | Foot |
| FH | Foot Head |
| FID | Free Induction Decay |

| | |
|---|---|
| fMRI | Functional Magnetic Resonance Imaging |
| FOV | Field Of View |
| FSL | FMRIB Software Library |
| FT | Fourier Transform |
| FWHM | Full Width at Half Maximum |
| GABA | $\gamma$-Aminobutyric Acid |
| GDS | Geriatric Depression Scale |
| GM | Gray Matter |
| Glc | Glucose |
| Gln | Glutamine |
| Glu | Glutamate |
| Gly | Glycine |
| Glx | Glutamate+Glutamine |
| GSH | Glutathione |
| H | Head |
| Hz | Hertz |
| ICNs | Intrinsic Connectivity Networks |
| IMCL | Intramyocellular |
| JLO | Benton's Judgment of Line Orientation Test |
| jMRUI | Java-Based Magnetic Resonance User Interface |
| KNN | K-Nearest Neighbor |
| L | Left |
| Lac | Lactate |
| LCModel | Linear Combination of Model |
| LPS | Left, Posterior, Superior |
| LR | Left Right |
| MAE | Mean Absolute Error |
| MDS-UPDRS | Movement Disorder Society Unified Parkinson's Disease Rating Scale |
| mI | Myo-inositol |
| MMSE | Mini Mental State Examination |
| MNI | Montreal Neurological Institute |

| | |
|---|---|
| MR | Magnetic Resonance |
| MRI | Magnetic Resonance Imaging |
| ms | Millisecond |
| MSE | Mean Square Error |
| NAA | N-Acetyl Aspartate |
| NAAG | N-Acetylaspartylglutamate |
| NIfTI | Neuroimaging Informatics Technology Initiative |
| P | Posterior |
| PC | Posterior Commissure |
| PCC | Posterior Cingulate Cortex |
| PCr | Phosphocreatine |
| PD-CN | Parkinson's Disease with Cognitively Normal |
| PDD | Parkinson's Disease with Dementia |
| PD-MCI | Parkinson's Disease with Mild Cognitive Impairment |
| PET | Positron Emission Tomography |
| PPM | Parts Per Million |
| PRESS | Point Resolved Spectroscopy |
| PSNR | Peak Signal to Noise Ratio |
| PVE | Partial Volume Effects |
| R | Right |
| ReLU | Rectified Linear Unit |
| RMSE | Root Mean Square Error |
| RF | Radio Frequency |
| RL | Right-Left |
| ROI | Region of Interest |
| rs-fMRI | Resting State Functional Magnetic Resonance Imaging |
| Sec | Second |
| SDMT | Symbol Digit Modalities |
| SE | Spin Echo |
| sI | Scyllo-inositol |
| SMA | Supplementary Motor Area |

| | |
|---|---|
| Smote | Synthetic Minority Over-Sampling Technique |
| SMN | Sensorimotor Network |
| SNK | Student-Newman-Keuls |
| SNR | Signal to Noise Ratio |
| STD | Standard Deviation |
| STE | Stimulated Echo |
| STEAM | Stimulated Echo Acquisition Mode |
| SR | Super Resolution |
| SRCNN | Super Resolution Convolution Neural Network |
| SVM | Support Vector Machine |
| T1w MRI | T1 weighted MRI |
| T2w MRI | T2 weighted MRI |
| Tau | Taurine |
| tCho | Total Choline |
| tCr | Total Creatine |
| TE | Echo Time |
| TFE | Turbo Field Echo |
| TM | Mixing Time |
| tNAA | Total N-AcetylAspartate and N-Acetylaspartylglutamate |
| TR | Repetition Time |
| UPDRS | Unified Parkinson Disease Rating Scale |
| VAN/SN | Ventral Attention/Salience Networks |
| WCST | Wisconsin Card Sorting Test |
| WM | White Matter |
| WSL | Windows Subsystem for Linux |

# 1. INTRODUCTION

Magnetic resonance imaging (MRI) is a non-invasive technique using non-ionizing radiation to generate anatomical images of the body. Therefore, it is one of the safest technologies for the diagnosis and monitoring of several diseases compared to other imaging modalities like positron emission tomography (PET) and computed tomography (CT). MR images are commonly used for diagnosis of many diseases such as multiple sclerosis, spinal cord disorders, stroke, and tumors [7]. Using MRI, several images with different contrasts, such as T1-weighted (T1w), T2-weighted (T2w), diffusion tensor imaging (DTI), fluid attenuated inversion recovery (FLAIR), arterial spin labeling (ASL), and proton magnetic resonance spectroscopic imaging ($^1$H-MRSI), could be generated. Each MR modality has its own advantages. For instance, T2w FLAIR images display brain tumor and surrounding edema as a hyperintense region [8]. Additionally, ASL is one of the main techniques employed for the cerebral blood flow (CBF) measurement in diseases, particularly such as cerebrovascular disease, dementia, and brain tumors [9]. DTI could reveal white matter tracts in the brain and could be used to assess the local effects of a tumor on the integrity of the white matter [10]. Moreover, integration of DTI and functional MRI (fMRI) in new navigation systems provides topographical characterization and the volumetric assessment of the functional and anatomical connections of the brain [10].

Unlike other MRI modalites, MRS technique provides invaluable metabolic information. The creatine (Cr) metabolite levels provide information about the energy metabolism, and has been reported to be higher in mixed or nonspecific multiple sclerosis lesions [11]. N-Acetylaspartate (NAA) is another MR spectroscopic metabolite that is an indicator of neuronal viability. The NAA peak intensity has been observed to be smaller in the brain tumor regions than in the normal brain tissue [12]. Also, lower NAA levels and a lower NAA over creatine (Cr) ratio have been reported in the literature as possible findings of cognitive impairment secondary to neuronal loss and dysfunction in Parkinson's disease (PD) [13], [14], [15], [16], [17]. On the other hand,

choline (Cho) is a marker of membrane synthesis and degradation, which has been observed to be higher in brain tumors [12]. Additionally, higher Cho levels and higher Cho/Cr have been reported in Parkinson's disease with mild cognitive impairment (PD-MCI) [14], [15]. Moreover, myo-inositol (mI) has been indicated as a marker of gliosis, and higher mI levels have been reported in MCI as one of the early biomarkers for progression [18], [19], [20]. Overall, MRS is a powerful technique that can be used in clinical diagnosis and disease treatment planning of several diseases including brain tumors, multiple sclerosis, and neurodegenerative diseases such as PD [21], [22].

PD is the second most common neurodegenerative disorder. A study estimated the number of patients with PD as 4.7 million in the most populous five countries in Western Europe in 2005, and it is projected that this number will reach up to 9.3 million by 2030 [23]. PD is currently diagnosed via motor symptoms, including resting tremor, rigidity, and bradykinesia [24]. Additionally, non-motor symptoms, such as cognitive impairment, anxiety, depression, apathy, anosmia, autonomic symptoms such as urinary incontinence, constipation, and sleep disorders, accompany and sometimes even precede the motor symptoms in PD and have an adverse effect on the quality of life [25]. MCI has been reported in 18.9 % to 38.2 % of PD patients, depending on arbitrarily predefined standard deviations of neuropsychological test scores [26]. Moreover, MCI is one of the key risk factors for dementia, and 60 % of PD-MCI patients eventually develop dementia (PDD) as the last stage of cognitive decline [27], [28], [29]. So, determining objective and sensitive indicators of early PD-MCI has been needed. As MR spectroscopic data provides metabolic changes in the brain, defining MRS based biomarkers of PD-MCI has been a key research topic, and might contribute to slowing down progression to dementia if successful treatments might become available in the future.

Although $^{1}$H-MRSI provides valuable chemical information, it still has some limitations preventing its wider use in the clinics. In MRS, the relative or absolute concentrations of tissue metabolites are calculated within a specific anatomical region of interest (ROI), which is called a spectroscopic voxel. A voxel within the brain might contain three fundamental tissue components, gray matter (GM), white matter (WM),

and cerebrospinal fluid (CSF). Tissue contents within a spectroscopic voxel have direct effects on the MRS data quantification results, such as a voxel having more water content (more CSF compared to the GM and WM tissue types) would have reduced peak intensities [30]. Therefore, partial volume effect (PVE) should be taken into account for a proper MRS quantification.

Either single-voxel or multi-voxel acquisition can be performed for spectroscopy. Single voxel is located at one volume of interest (VOI), which is more practical in comparison to the multi-voxel MRS imaging (MRSI) even though multi-voxel MRSI covers a larger portion of the brain that might enable better tumor boundary definition for treatment planning [12]. However, multi-voxel $^{1}$H-MRSI is still challenging due to the chemical shift displacement artifact, which happens due to the frequency differences between the metabolites. This artifact results in spatial misregistration for all metabolites except the reference frequency metabolite, which is usually set as NAA. On the other hand, the location of other metabolites is shifted with different amounts in three dimensions. Chemical shift displacement is higher for lower radio frequency (RF) bandwidths [31], [32], [33], [34] and the correction of this is needed to provide accurate and reliable interpretation of MRSI data.

Another challenge of $^{1}$H-MRSI is analyzing it with other MRI modalities. MRS data is often acquired from a restricted portion of the brain, and the resultant MRS metabolite maps that could be generated at different frequencies do not cover the whole brain. Therefore, it is not straightforward to analyze MRS values at different brain regions like the other MR modalities. One solution to conduct region of interest (ROI) analysis for MRSI along with other MRI modalities is creating metabolite maps and overlay them onto anatomic MRI and common brain atlases for data analysis [2].

The quality evaluation of each spectrum is another issue for an accurate interpretation of MRS data. A visual quality evaluation of all voxels of MRSI data is usually impractical, necessitating the use of automated techniques to exclude poor MR spectroscopic data for an accurate data quantification [2].

Another problem of $^{1}$H-MRSI is low spatial resolution, which is usually around ten times lower than the anatomical MR images. The spectral metabolites of interest are found at much lower concentrations than water in the body, so larger voxel sizes are used in $^{1}$H-MRSI to get a better SNR. Even if SNR is not a concern, increasing spatial resolution of $^{1}$H-MRSI might be desirable, which results in a long scan time. Another low-cost approach with no scan time or SNR penalty is using post-processing super resolution techniques that might help with increasing the spatial resolution of $^{1}$H-MRSI. The term "super resolution (SR)" describes a technique designed to improve the spatial resolution of images. Many image processing methods have been developed to increase the spatial resolution of natural images [35], satellite images [36], and medical imaging [37]. Learning based image super resolution methods use a training model for determining a mapping between lower and higher resolution images. The majority of conventional post-processing techniques for super-resolution MRSI use model-based regularization with anatomical MRI [38], [39], which frequently generates painfully slow reconstructions. Recently, a few data-driven deep learning-based image super-resolution methods have been presented and shown promising results for super-resolving MRSI metabolic maps [40], [41], [42].

The present work endeavors to elucidate some of the current limitations ongoing with $^{1}$H-MRSI. This dissertation has three aims that has been presented chapter by chapter, which are as follows:

1. to present an open-source user-friendly advanced three-dimensional (3D) $^{1}$H-MRSI data analysis program, called Oryx-MRSI,

2. to use Oryx-MRSI software for the multivoxel $^{1}$H-MRSI data analysis of PD patients to determine metabolic correlates of MCI, and

3. to improve the resolution of $^{1}$H-MRSI data using deep learning.

# 2. BACKGROUND

This chapter provides basic information about MRI and MRSI followed by a short introduction of PD. Possible biomarkers that can be helpful to detect PD-MCI using MRS are also discussed. Lastly, super-resolution with deep learning in MRSI is discussed.

## 2.1 Magnetic Resonance Imaging

MRI is a non-invasive imaging technique that can be used safely in the diagnosis and follow-up of several diseases, which does not use harmful ionizing radiation. As a consequence, even kids can be scanned with MRI without causing any harm.

An MR system is comprised of six different components. Each component has its own role to acquire the final MR image. In this system, a magnet produces the main magnetic field ($B_0$), shim coils provide a homogenous magnetic field, an RF coil excites and receives the MR signal, a gradient coil is used for spatial localization, and a computer processes the signal to visualize the final image. Once a patient is within an MR scanner, protons inside the human body align either parallel or anti-parallel to the direction of $B_0$, according to basic MRI physics. Protons also precess with a specific frequency called the Larmor frequency around the axis of the main magnetic field. Larmor frequency is calculated as shown in Eq. 2.1 [43],

$$f_0 = \frac{\gamma B_0}{2\pi} \tag{2.1}$$

where the gyromagnetic ratio and the external static magnetic field are represented by $\gamma$ and $B_0$, respectively.

The energy required to stay parallel or anti-parallel to the external magnetic

field differ by $\Delta E$ and is calculated as [43],

$$\Delta E = \frac{\gamma h B_0}{2\pi} \tag{2.2}$$

where h is the Planck constant (6.626x10-34J/sec).

The relative number of spins at the higher energy state relative to the lower energy state in thermal equilibrium is given in Eq. 2.3 [43], where the number of spins aligned parallel to $B_0$ (this state is preferred due to the need for lower energy) and the number of spins aligned anti-parallel to $B_0$ (requires higher energy) are indicated as $N_{up}$, and $N_{down}$, respectively. The Boltzmann's constant, given as k, is equal to 1.381 x $10^{-23}$ $J.K^{-1}$. Lastly, temperature in Kelvin is represented by T.

$$\frac{N_{up}}{N_{down}} = e^{-\frac{\Delta E}{kT}} \tag{2.3}$$

The difference in the number of spins at two alignments creates a net magnetization, M. In order to excite spins resonating at a desired frequency range, an RF pulse is applied perpendicular to the external magnetic field. As a result, the magnetization gets rotated away from the $B_0$ direction. As soon as the RF energy is removed, spins revert back to the equilibrium condition, where M is parallel to $B_0$ while creating a magnetic flux detectable by the RF coil. The signal that is acquired during this return is called the "free induction decay (FID)" signal. FID signal is in time domain, which is then converted into the frequency domain by a Fourier transform (FT). The application of multiple RF pulses is necessary to create an MR image. A pulse sequence is used to control the application of RF pulses along with the gradients, which are necessary to perform spatial localization. Depending on the order and the timing of RF and gradient pulses, several MR imaging modalities could be generated, including T1-weighted, T2-weighted, DTI, FLAIR, ASL and MR spectroscopy using the same MRI equipment.

## 2.2 Magnetic Resonance Spectroscopy

MRS offers spectroscopic details on the metabolic activity taking place in the region of interest in addition to the grey-scale anatomical picture produced from MRI device. In other words, MRS utilizes frequency to encode metabolic information, whereas MRI basically utilizes frequency to encode spatial information. The MR spectroscopic signal is known as a spectrum. The ability to see metabolites as discrete peaks is possible after the transfer of FID data into the frequency domain.

### 2.2.1 Magnetic Resonance Spectroscopic Imaging

Magnetic resonance spectroscopy can be acquired at a single-voxel or multi-voxel. A single VOI is used in single-voxel MRS method to produce an MR spectrum, whereas many adjacent volumes are used in multi-voxel MRS method to produce spectra. This method is often preferred to cover a wider area than single-voxel MRS method.

#### 2.2.1.1 Chemical Shift

The chemical environment, which has the potential to shift the resonant field, affects the resonant frequency in addition to $\gamma$ and the external $B_0$ field. This phenomenon, known as chemical shift, results from the mobility of the surrounding electrons shielding the electron from the external magnetic field. Differences in resonant frequency can be expressed as,

$$\omega = \gamma B_0(1 - \sigma) \tag{2.4}$$

where $\sigma$ is the chemical shielding constant [43]. As expressed in Eq. 2.4, the

frequency shift caused by the chemical environment is proportional to $B_0$. The chemical shifts can be defined in parts per million (ppm) as [43],

$$\delta = 10^6 * \frac{\omega - \omega_{ref}}{\omega_{ref}} \tag{2.5}$$

where $\omega$ and $\omega_{\text{ref}}$ represent the compound frequency and the reference frequency, respectively. The chemical shift is denoted in ppm instead of Hertz (Hz), because the frequency then becomes independent of the external magnetic field strength.

When nuclei are particularly near to another nuclei, their magnetic fields interact, causing J-coupling or spin-spin coupling. J-coupling results in changes of the phase of the MR spectroscopic signal over time. The external magnetic field strength has no effect on the J-coupling strength, which is measured in Hz.

Some other factors, such as the longitudinal (T1) and transverse (T2) relaxation times, proton density, and diffusion, that affect the main contrast in MR imaging can also have an impact on how a spectrum appears. The echo time (TE) is another key element in spectral appearance. The term "TE" describes the interval of time between the first RF pulse application and the data acquisition. The repetition time (TR), which is the time distance between the consecutive blocks in a pulse sequence, also affects the spectrum. The time interval between the final two 90°RF pulses in a Stimulated Echo Acquisition (STEAM) sequence is referred to as mixing time (TM) [44].

Even though $^{1}$H-MRS is the most widely utilized MRS technique, phosphorus ($^{31}$P), carbon ($^{13}$C), nitrogen ($^{14}$N), sodium ($^{23}$Na), and fluorine ($^{19}$F) MRS could also be acquired. The majority of clinical MRI scanners are equipped with $^{1}$H-MRS protocols, so additional hardware is not required for $^{1}$H-MRS data acquisition while all other nuclei require special RF coils and multi-nuclei data acquisition packages.

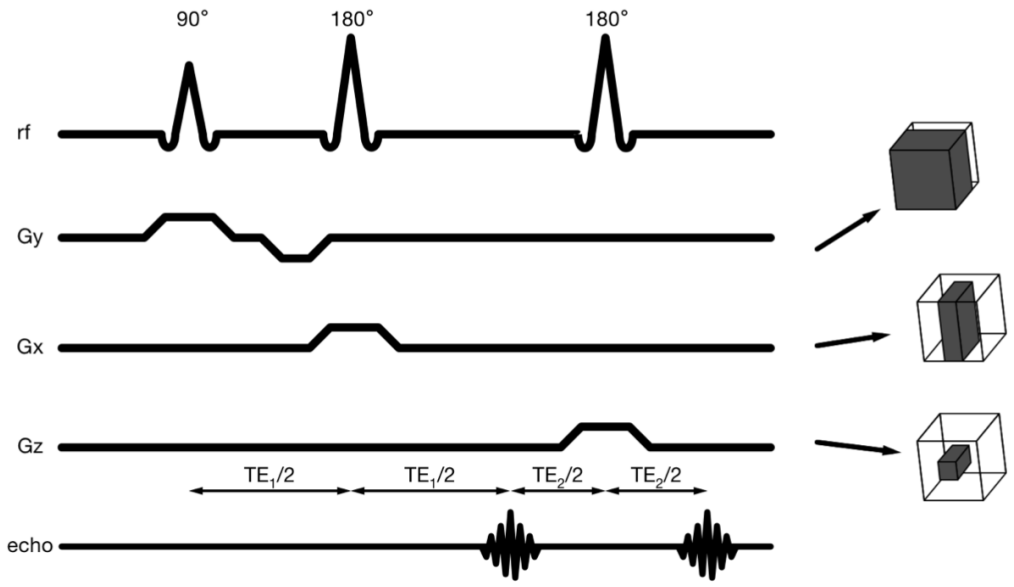


**Figure 2.1** PRESS sequence diagram [1].

#### 2.2.1.2 Data Acquisition

The two most prominent and preferred $^{1}$H MR spectroscopy acquisition sequences are Point Resolved Spectroscopy (PRESS) and STEAM. PRESS makes use of three slice-selective RF pulses with flip angles of 90°, 180°, and 180 applied along with three gradients in all three orthogonal directions. Figure 2.1 shows a schematic illustration of the PRESS pulse sequence for a single voxel spatial localization.

A 90 RF pulse and a gradient along y axis are applied to excite the spins for the selection of a slice along the y axis. After a time TE1/2, a 180 RF pulse and another gradient along the x axis excite the spins to get a column along x and y axes. The first echo happens at TE1. A second 180 RF pulse and the last gradient along the z axis are applied to excite the spins at a specific location along the z axis after a time TE1+TE2/2. The second 180 RF pulse is followed by a delay of TE2/2 before the second echo occurs, which is then sampled. Finally, the selected voxel's spectrum is generated.

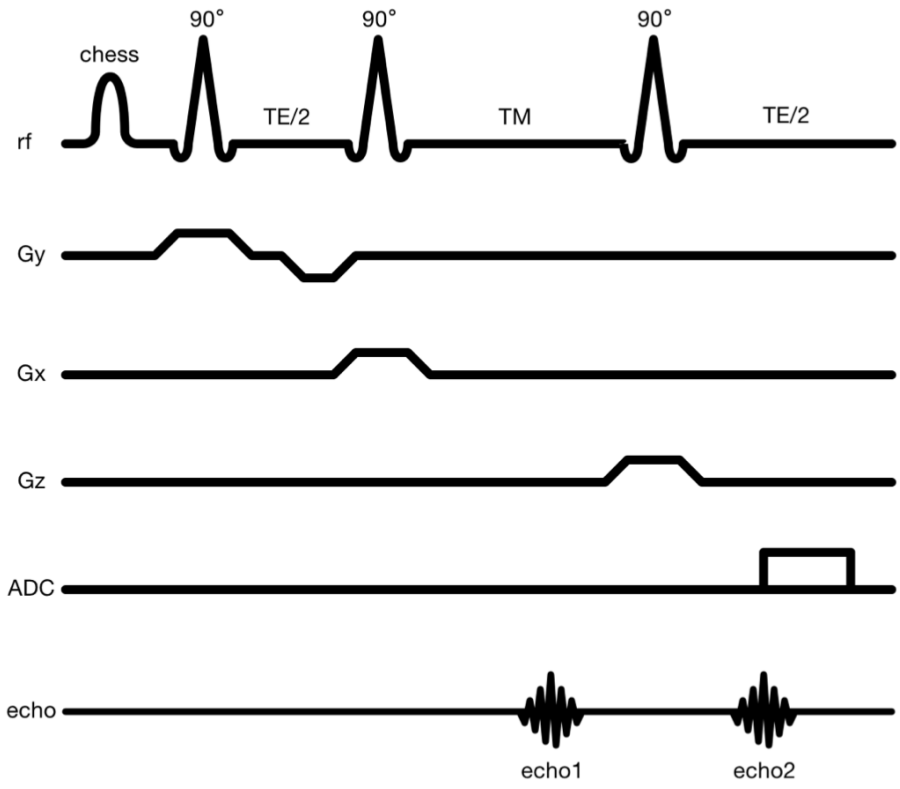


**Figure 2.2** STEAM sequence diagram [1].

Three 90 slice selective pulses along the x, y, and z axes are used in the spatial localization technique known as STEAM. Three 90 RF pulses are employed with TE/2 and TM time delays. The three 90 RF pulses are applied along with the gradients Gx, Gy, and Gz similar to the PRESS method. The echo is captured TE/2 after the last RF pulse. From the point where three localizations overlap, a spectrum is obtained. Figure 2.2 shows a schematic illustration of the STEAM pulse sequence for a single voxel.

When a higher SNR is required, PRESS is preferred over STEAM. STEAM is utilized when short TE is preferred and the chemical shift artifact is at its minimum. TE for STEAM can be as short as 20 ms, whilst TE for PRESS can range from 30 ms up to high TEs like 288 ms.

#### 2.2.1.3 Chemical Shift Artefact

As discussed in section 2.2.1.1, the protons are shielded by the electrons causing frequency changes depending on the shielding factor. When an RF pulse is applied at a specific frequency range in the presence of a gradient, the spatial position of the excited slice varies for metabolites with different resonant frequencies. This variation is related to the difference in the precessional frequencies between metabolite protons and the applied gradient [43]. Due to their various resonance frequencies, VOI for various metabolites then gets shifted relative to another metabolite. The shift amount $\Delta x$ can be calculated as [43],

$$\Delta x = \frac{\Delta \omega}{\gamma G_x} \tag{2.6}$$

where $G_x$ is the gradient strength and $\Delta x$ is the frequency difference. Also, the chemical shift amount can be expressed as [43]:

$$\Delta x = X_l * \frac{\Delta \omega}{BW_x} \tag{2.7}$$

where $BW_x$ is the RF excitation pulse bandwidth and $X_l$ is the width of the total excited spectral region in the given direction. Figure 2.3 shows an example of chemical shift displacement of water and NAA.

#### 2.2.1.4 MR Spectroscopic Metabolites

Alanina (Ala)

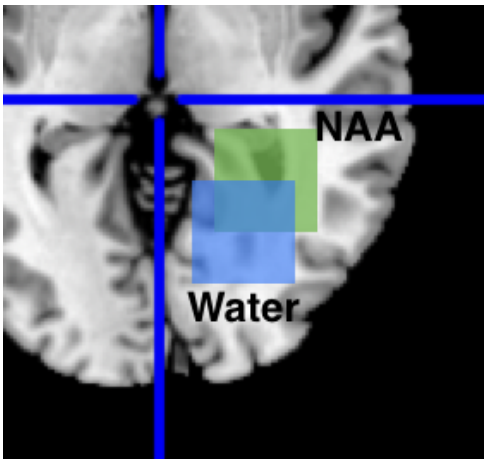


**Figure 2.3** An example of chemical shift displacement of water and NAA.

The level of Ala, an amino acid with a 0.5 mM concentration in normal tissue, rises in the human brain in malignancies such as gliomas or meningiomas. It possesses two resonances. The first one is a quartet found at 3.77 ppm and the second one is a doublet that overlaps the resonances at 1.47 ppm [45].

Aspartate (Asp)

As a neurotransmitter, Aspartate (Asp) is an excitatory amino acid. It can not cross the blood-brain barrier. Glucose and various precursors make up aspartame. In the brain, Asp levels range from 1-2 mM. Three doublets of doublets are present on its spectrum. There is one doublet-of-doublets at 3.89 ppm, and there are two more doublets-of-doublets at 2.65 ppm and 2.80 ppm [45], [46].

$\gamma$-Aminobutyric acid (GABA)

It is an inhibitory neurotransmitter, and the human brain has about 1 mM GABA. 1.89 ppm, 2.28 ppm, and 3.01 ppm are the places of the three resonances of GABA. Under particular circumstances, such as a combination of strong magnetic fields and spectral fitting [45], [47], the detection of GABA levels is achievable. Neuropsychological problems [48], depression [49], [50], epilepsy [51], and panic disorder [52] can all be accompanied by changes in GABA concentrations.

Creatine and Phosphocreatine (PCr)

The combined levels of creatine and phosphocrestine (tCr) is the indicator of energy metabolism. tCr has two singlet resonances, the first one is at 3.03 ppm, while the second one is at 3.93 ppm. In the human brain, Cr and PCr concentrations range from 4.0 to 5.5 mM and 4.5 to 6.0 mM, respectively. However, there is a slight distinction between the white matter and gray matter concentration values. Between Cr and PCr, there are methyl resonance differences. It is nearly hard to reliably separate these two metabolites because methyl resonances are very tiny. However, at a stronger magnetic field (7T or greater), methyl resonances can be substantial enough for a trustworthy separation of metabolites.

Choline

Cho, phosphorylcholine (PCh), and glycerophosphorylcholine (GPC), together known as total choline (tCho), is detected as a singlet at 3.2 ppm. Changes in tCho are closely connected to changes in membrane composition [45]. Cho peak elevation may be a sign of demyelination, gliosis, ischemia, brain injury, malignancy, or Alzheimer's disease. However, a decreasing amount may serve as a biomarker for liver disease and stroke at its early stages [53], [54], [55].

Glucose (Glc)

There are five hydroxyl groups among the seven protons that make up glucose (Glc). Glc has two anomers, which coexist in aqueous solutions, with the former having an equilibrium concentration of 36 % and the latter having a concentration of 64 %. Glc serves as an energy store [45], [56], [57].

Glutamate (Glu)

Glutamate is an excitatory neurotransmitter that serves as both a precursor and GABA storage that is an inhibitory neurotransmitter. Additionally, it is crucial for the

production of proteins, big peptides, and very small metabolites. Since the resonance groups of Glu are positioned at 2.04 ppm, 2.35 ppm, and 3.74 ppm, they may overlap with resonances of NAA, Gln, and GABA [45]. Although Glu and Gln levels can not be distinguished at magnetic field strengths of standard clinical MRI scanners, high magnetic field strengths of 7T can assist with resolving these metabolites.

Glutamine (Gln)

Glutamine is one of the amino acids and has resonance groups located between 2 and 3.8 ppm with a concentration of 2-4 mM. Low magnetic field strengths make it impossible to discriminate between Glu and Gln, therefore their peaks are frequently measured combined and given the name Glx [58].

Glycine (Gly)

It is a neurotransmitter that acts as an inhibitor and is found throughout the central nervous system. Gly can be transformed into Cr. Gly has a singlet peak at 3.55 ppm. It overlaps with mI, making it challenging to measure the level of glycine alone [45].

Lactate (Lac)

Lactic acid is the result of anaerobic glycolysis. Regular in vivo MRS is unable to detect lactate because of its low concentration and overlap with lipid in normal human brain. Lactate can be seen, though, if its concentration rises as a result of diseases like tumors, trauma, strokes, and hyperventilation, or with special MR spectral editing sequences. Lac has a doublet at 1.31 ppm and a quartet at 4.10 ppm [45].

Myo-Inositol (mI)

Myo-inositol is one of the cyclic sugar alcohols that has four resonance groups. They are a smaller triplet at 3.27 ppm, a triplet at 3.52 ppm, a triplet at 3.61 ppm,

and a final triplet at 4.05 ppm. mI is a storage form for glucose and plays a critical role in cell proliferation. By combining short TE with a strong magnetic field, mI can be easily detected. The peak level of mI are high in demyelination and gliosis [45].

N-Acetylaspartate (NAA) N-Acetylaspartylgluatamate (NAAG)

Reduced levels of this amino acid, which serves as a marker for neuronal density, are indicative of cell loss in conditions such malignancies [59], [60], stroke [61], [62], and multiple sclerosis [63], [64]. Additionally, acute metabolic abnormalities, such hypoxia and ischemia, have been related to reduced NAA levels. The major singlet resonance of N-Acetyl Aspartate is found at about 2.01 ppm, whereas that of N-Acetylaspartylgluatamate (NAAG) is at 2.04 ppm. In the human brain, NAA concentrations range from 7 to 16 mM and NAAG concentrations from 0.6 to 3 mM. Only a strong magnetic field can separate NAAG, which has multiple peaks that overlap with those of NAA and glutamate.

Scyllo-Inositol (sI or s-Ins)

Scyllo-inositol (sI) is another cyclic sugar alcohol, which is a kind of abundant isomer of inositol that comes after mI. The level of sI in the human brain rises in persistent alcoholism and has a singlet at 3.34 ppm [65], [66].

Taurine (Tau)

An amino acid called Taurine (Tau) plays a part in the osmoregulation and modulation of neurotransmitter function. Two triplets at 3.25 ppm and 3.42 ppm are seen in the Tau spectra. It is hard to identify Tau at lower magnetic field strengths, because it overlaps with mI and Cho [67].

#### 2.2.1.5 Software Packages

$^{1}$H-MRSI has been one of major MRI modalities for the diagnosis, follow-up and treatment planning of several diseases, including brain tumors and neurological disorders [68], [69]. Despite the vast amount of information provided by $^{1}$H-MRSI, it is still not widely employed in clinical settings. As a result, there has been a major effort for improving the clinical utility of $^{1}$H-MRSI with recent developments in data acquisition, processing, and quantitative analysis aspects [70], [71], [72]. Additionally, several studies employed machine learning techniques to denoise and enhance the MRS data [73], [74]. As part of these extensive efforts, open-source command-line scripts or software with user-friendly graphical user interfaces (GUIs) have been released in the past few years [75], [76], [77], [78], [79], [80], [81], [82], [83], [84], [85], [86], [87], [88], [89]. LCModel is one of the most popular MRS data quantification tools, which estimates metabolite concentration and metabolite to total creatine ratios for a range of metabolites, including macromolecules and lipids, and it recently became open source [75]. On the other hand, jMRUI [83] and Tarquin [87] offer customizable GUI-based tools for spectral visualization and quantification. Metabolite Imaging and Data Analysis System (MIDAS) provides whole-brain MRSI data visualization, processing, and analysis. Additionally, Osprey is a new open-source MRS data analysis software that currently supports single-voxel MRS data analysis [77]. Moreover, FSL-MRS is another Python-based open-source tool that provides data quantification of single-voxel MRS and 2D MRSI after converting the data into the NIfTI format [76]. More recently, MRspant has been released, which is an automated R-based MR spectroscopic data analysis tool for reading, visualizing, and processing MRS data [78]. The available features and limitations of these software packages are listed in detail in Table 2.1.

**Table 2.1**
The features of available software for processing and analyzing MR spectroscopic data.

| | GUI | MRSI Visualization | NIfTI-MRS | Metabolite Maps | Spectra Quality Control | Chemical Shift Correction | Fraction Calculation | Registraion | Atlas/voxel-based Statistics |
|---|---|---|---|---|---|---|---|---|---|
| **LCModel [75]** | Yes | Yes | No | No | No | No | No | No | No |
| **FSL-MRS [76]** | No | Yes | Yes | Yes | No | No | Yes | No | No |
| **Osprey [77]** | Yes | No | Yes | No | No | No | Yes | No | No |
| **MR Spant [78]** | No | Yes | No | No | No | No | Yes | No | No |
| **Gannet [79]** | No | No | No | No | No | No | Yes | No | No |
| **OXSA [80]** | Yes | Yes | No | No | No | No | No | No | No |
| **Open-source toolbox [81]** | Yes | Yes | No | Yes | Yes | No | Yes | Yes | Yes |
| **SIVIC [82]** | Yes | Yes | No | Yes | No | No | Yes | Yes | No |
| **JMRUI [83]** | Yes | Yes | No | No | No | No | No | No | No |
| **AQSES [84]** | Yes | Yes | No | No | No | No | No | No | No |
| **FID-A [85]** | Yes | No | No | No | No | No | No | Yes | No |
| **VeSPA [86]** | Yes | No | No | No | No | No | No | No | No |
| **Tarquin [87]** | Yes | Yes | No | Yes | Yes | No | No | No | No |
| **MIDAS [88]** | Yes | Yes | No | Yes | Yes | No | Yes | Yes | Yes |
| **jSIPRO [89]** | Yes | Yes | No | Yes | No | No | Yes | No | No |

#### 2.2.1.6 Limitations of MRSI

Although there have been major efforts for improving the clinical utility of $^{1}$H-MRSI with recent developments in data acquisition, processing, and quantitative analysis aspects [70], [71], [72], $^{1}$H-MRSI still has some limitations, including the chemical shift artifact, partial volume effects, ROI analysis, and low spatial resolution.

There have been some studies to reduce or remove the chemical shift artifact. Some of these methods included fat-suppression techniques, sensitivity encoding (SENSE), and post processing approaches [31], [33]. However, these techniques require expertise, which limit their clinical utility. Another approach is estimating the chemical shift amount and relocating all the metabolite maps considering their corresponding shift amounts based on the spatial localization parameters, which would result in an easy post-processing solution.

The analysis of a single voxel MRS is so practical with respect to that of multivoxel MRS. After single voxel is located at a chosen ROI, the MRS results of participants can be analyzed and interpreted for a given ROI. However, multivoxel MRS localization is almost never the same for different individuals, and group analysis requires registration, which is not straightforward.

In the literature, some studies have released their tools for multivoxel MRSI analysis. SIVIC [82] is one of them for the visualization and processing of the DICOM MRS data. It supports different MRS data collected from different MR vendors like Siemens, GE or Philips. On the other hand, chemical shift correction of the multivoxel MRS data isn't supported and the tool doesn't provide automated spectral quality check. Up to now, researchers have used visual approach to exclude bad quality spectra and there is a need for automated approach for objectivity.

Other tools like Java-Based Magnetic Resonance User Interface (jMRUI) [83], LCModel [75], or Osprey [77] can be used for MRS data quantification, but there is a need for a tool to further analyze the MRSI data. None of these tools have provided

automated registration of MRSI data onto common brain atlases like MNI152 brain atlas [90] considering the chemical shift correction. FMRIB Software Library (FSL) is an outstanding tool, which can be used for comprehensive analysis of fMRI, MRI and DTI [91], [92], [93]. Statistical Parametric Mapping (SPM) is a similar tool that enables all types of brain imaging data analysis [94]. FMRIB's Linear Image Registration Tool (FLIRT) could be adapted for MRSI data registration by using a converting matrix produced during registration of reference MRI images to a common brain atlas. To achieve registration with these tools, MRSI data should be transferred from spectral form to metabolite maps overlaid onto reference MRI images.

ROI analysis of MRSI data is another issue that needs addressing. Several regions of the common brain templates should be extracted and multiplied with the metabolite maps for regional statistical analysis of MRSI data. As an example, the brain parcellations defined on MNI152 brain atlas [90] could be used. Schaefer et al. [95] proposed human brain parcellations based on resting state fMRI (rs-fMRI), which could be adapted for MRS regional analysis.

## 2.3 Parkinson's Disease

PD is one of the progressive neurodegenerative disorders that manifests itself with motor symtomps, such as stiffness, bradykinesia, and resting tremor. Almost 80 out of 100 PD patients ultimately develop dementia [96]. A-synuclein accumulation in the form of Lewy bodies (LBs), neuronal loss in the substantia nigra, and deposits of other amyloidogenic proteins, including frequent amyloid-b and tau, are all examples of diagnostic neuro-pathology of PD [97]. The diagnosis of PD and the determination of its stages such as cognitively normal (PD-CN), PD-MCI, or dementia (PDD) are mainly based on clinical assessment and neuropsychological test measures [98]. The neuropsychological tests that are used for the diagnosis of Parkinson's Disease will be described in section 2.3.1.

### 2.3.1 Diagnosis of Parkinson's Disease

The Unified Parkinson Disease Rating Scale (UPDRS) is a commonly used assessment test for the determination of the severity of PD. It consists of four different domain assessments: motor manifestations, mental and mood manifestations, and daily activities like eating, dressing, and turning in bed. Information provided by caregivers or patients is included in parts 1, 2, and 4 of the UPDRS test. The third section of the examination looks at the individuals' motor symptoms. UPDRS is a standardized test to assess PD progression [99]. However, it is unable to evaluate health-related quality of life.

In addition to UPDSR, several neuropsychological tests are employed. One of them is the Addenbrooke's Cognitive Examination Revised (ACE-R) that evaluates cognitive abilities such as verbal fluency, language, orientation, and visuospatial skills [100].

Mini-mental state examination (MMSE) assesses cognitive impairment [101]. MMSE having 30-point questions is a common test used in medical practice to evaluate mild cognitive impairment and dementia. It consists of straightforward problems and questions like the location and time of the test, arithmetic problems like the series of eight, repeating lists of words, basic motor skills, and language comprehension. A high score denotes higher cognitive abilities.

The Stroop test, often known as the Stroop effect, is a standard neuropsychological exam that assesses a person's psychological abilities and attention [102]. This exam is identifying the color of a word. A word and its written ink are congruent in the first stage of the Stroop test. A word and its printed ink are not the same in the second part of the test. Since participants typically read the words without focusing on the written ink of the words, the latter part of this test is more difficult. They correct themselves and say the word's right color when they realize they said the color incorrectly. As a result, it takes a while to finish the Stroop exam.

Benton's Judgment of Line Orientation test (JLO) test provides a flexible way to examine spatial perception in both research and therapeutic settings [103]. Line segments in this test are orientated differently, and they need to be matched with a response card that has longer lines. The total score is determined by counting the right answers, with age and gender adjustments. Patients are classified as normal, mildly impaired, or severely impaired based on the test results.

The symbol digit modalities test (SDMT) was developed to assess the level of patients' neurological damage. The SDMT can be used to look at the impairment of neurocognitive abilities, such as motor, speed, attention, and visual scanning [104]. Participants are given a set of symbols to match with a sample set of numbered symbols, and they have 90 seconds to do so while writing down the numbers that go with each match. The examination is given in both written and oral form.

The Wisconsin Card Sorting Test (WCST) is a neuropsychological assessment of the thinking ability and cognitive flexibility [105]. There are two decks of cards, and each deck has a number of cards with varying colors, sizes and forms. It is believed that the stimulation card from the first deck of cards will match the second deck of cards. Each participant is shown a card from the second deck one at a time. As a consequence, the player is required to match the first deck of cards with the second one in accordance with rules that wasn't mentioned to her/him. By formulating his rules in accordance with the feedback provided following each right response, the participant must match the cards.

## 2.4 Super-Resolution with Deep Learning

Deep learning is the new area of machine learning and it could imitate human brain workings in terms of processing data or creating patterns for decision making. Neural networks can be thought like the human brain neuron nodes and all of them are connected to each other like a web. Deep learning is very effective because of its ability to learn a sequence of non-linear transformations, extract features, and fuse information

from different modalities. In other words, it is able to learn in supervised, semi-supervised and unsupervised manners for data representations with specific algorithms [106], [107], [108]. The main reasons why deep learning has increased in popularity are improved GPU technology, increased training and testing data sets for deep learning, and breakthroughs in processing machine learning research.

Compared to hand-engineered domains such as computer vision and audio analysis, deep learning has outstanding performance. At the same time, deep learning architectures including deep belief networks, recurrent neural networks, and deep neural networks have outperformed the state of the art especially in handwriting [109] or face recognition [110], pattern recognition [111], image classification [112], image super resolution [113], and social network filtering [106] within the last decade.

There have been many different state-of-the-art image super resolution methods, such as fast super-resolution convolutional neural network (FSRCNN) [114], photo-realistic single image super-resolution using a generative adversarial network (SRGAN) [115], second-order attention network (SAN) for single image super resolution [116], multi-scale residual network (MSR) for image super-resolution [117], and enhanced deep residual networks for single image super-resolution (EDSR) [6].

## 2.5 The Aims of This Thesis

The aims of this thesis were threefold. The first aim (Chapter 3) was to develop an open-source 3D MRSI data analysis software, called Oryx-MRSI, with a user-friendly GUI to improve upon aforementioned limitations of MRSI data analysis by reading LCModel outputs as well as raw spectral data and enabling visualization and metabolite map generation considering the chemical shift correction while providing automated spectral quality control based on full width at half maximum (FWHM), SNR, Cramer-Rao lower bounds (CRLB), and fraction of CSF (fCSF). This software provided registration of metabolite maps onto the MNI152 brain atlas [90] for the calculation of metabolite intensities at multiple brain locations, including the functional

parcellations of the human cerebral cortex based on rs-fMRI networks [95] or the MNI structural brain atlas regions. A spreadsheet was also provided to export the mean, median, and standard deviation (SD) values of the metabolites and metabolite ratios with or without fCSF correction at the multiple brain regions. The second goal was to investigate metabolic changes in PD-MCI by using 3D MRSI data of 76 participants (16 healthy controls (HC), 26 PD-CN patients and 34 PD-MCI). This was also an example of the clinical usage of the developed software, Oryx-MRSI. Metabolic values calculated using Oryx-MRSI were assessed to define differences between PD-MCI, PD-CN, and HC at several brain regions. Additionally, calculated metabolic parameters and NPT scores were statistically compared between groups. Lastly, supervised machine learning algorithms were applied to classify HC, PD-CN, and PD- MCI groups based on metabolite levels. The last aim of this thesis was to design a new post-processing super resolution algorithm based on deep learning that would generate high resolution spatial MRSI maps.

# 3. ORYX-MRSI

*This chapter describes Oryx-MRSI, which has been developed as a fully-automated open source software for $^{1}$H-MRSI data analysis.*

## 3.1 Rationale

There are some limitations of $^{1}$H-MRSI preventing its wider use in the clinics, including the spectral quality issues, partial volume effect, chemical shift artifact, and ROI analysis of the metabolite maps (Detailed information of these limitations are given in section 2.2.1.6). In this study, a MATLAB-based open-source data analysis software for three-dimensional $^{1}$H-MRSI, called Oryx-MRSI, which includes modules for visualization of raw $^{1}$H-MRSI data and LCModel outputs, chemical shift correction, tissue fraction calculation, metabolite map production, and registration onto standard MNI152 brain atlas while providing automatic spectral quality control, is presented. Oryx-MRSI enables region of interest analysis at brain parcellations defined on MNI152 brain atlas. The contents of this chapter has been published at the IMA Journal [2].

## 3.2 Methods

Oryx-MRSI was written in MATLAB 2020a (Mathworks Inc., Natick, Massachusetts) and also has been tested using MATLAB versions 2020a and newer in Ubuntu 18.04.5 LTS and macOS 11.4 Big Sur. All sub-functions of Oryx-MRSI can be called as command-line scripts. Oryx-MRSI can be easily used through a user-friendly GUI. The GUI was developed with the MATLAB App Developer and all the inputs that are taken from the user are checked and verified to handle possible user errors. A complete Oryx-MRSI data analysis pipeline includes nine different modules, which are load data, co-registration, segmentation, FWHM and SNR, spectral quality, metabolite maps, registration, ROI analysis, and distributions. Before the analysis starts, the user

is asked to provide some parameters, including the cut-off values of the CRLB, fCSF, FWHM, and SNR for voxel exclusion criteria, a frequency parameter for the reference metabolite, RF bandwidth of the sequence for chemical shift correction, and cut-off value for the probabilistic binary map after registration onto the MNI152 brain atlas. The results of the analysis are automatically saved in the " spectra" folder after the execution of each module. The following subsections describe the Oryx-MRSI modules in detail.

### 3.2.1 Load Data

This module enables the user to visualize 3D $^{1}$H-MRSI data located either in a raw data file or COORD file generated by LCModel. Currently, Oryx-MRSI supports 3D $^{1}$H-MRSI raw data saved in the SPAR/SDAT format acquired on a Philips MR scanner and NIfTI-MRS format. For reading the NIfTI-MRS data, an open-source code available at 'https://github.com/schorschinho/nifti-mrs-matlab'. This github link for Nifti-MRS-Matlab was adapted. Some examples of 3D $^{1}$H-MRSI datasets can be found in the " /Oryx-MRSI/Dataset" folder under the GitHub repository located at 'https://github.com/Computational-Imaging- LAB/Oryx-MRSI'. Oryx-MRSI also allows the user to load and visualize their own dataset stored as an SPAR or a NIfTI-MRS file under the " /Oryx-MRSI/Dataset" folder. The necessary steps of the data preparation before data analysis with Oryx-MRSI are detailed in the documentation available in the GitHub repository.

The default imaging system for the data order of the raw data and LCModel outputs are left, posterior, and superior (LPS). Accordingly, the column numbers increase from right to left, and the row numbers increase from the anterior to posterior directions at a selected slice at the visualization screen. Although several metabolites, including lipids and macromolecules, are quantified by LCModel, Oryx-MRSI currently creates metabolite maps for Cr+PCr, Glx, Cho, mI, Lac, and lipids (Lip13a, Lip13b, Lip13a + Lip13b), in addition to another metabolite, which could be defined on the main screen in addition to the predefined metabolite maps. The software also allows

zooming in on a voxel for a closer view, and visualization of the individual metabolites.

### 3.2.2 Co-registration

Oryx-MRSI supports reading reference structural MR images in NIfTI format. In this module, first, the position and orientation information of the scanner-space coordinates of the field of view (FOV) are parsed from an SPAR file, and each voxel's size, position, and orientation information are calculated considering their slice, row, and column numbers. This module uses 'Gannetmask_Philips' function from Gannet for co-registration [79] after some necessary modifications for 3D data analysis and generates binary masks for FOV, volume of interest (VOI), and individual voxels. Oryx-MRSI asks the user to select one reference metabolite from among H2O, NAA, Cr, Cho, and Lac/Lip or to set a free frequency parameter, and to specify the RF bandwidths of the MR system for the excitation and the first and second echo directions in Hz. The chemical shift correction is applied when the chemical shift correction option is set to 'on,' and the RF band-widths are provided by the user.

For chemical shift correction, the gradient strengths (T/mm) on the excitation, and first and second echo directions (dir) are calculated as follows:

$$GR_{dir} = \frac{-RF_{dirbw}}{gamma_{1H} * 10^{-3} * VOI_{dir}} * chemicalshiftsign(dir) \tag{3.1}$$

where $\text{gamma}_{1\text{H}}$ is equal to the gyromagnetic ratio in Hz/T, VOI represents the volume of interest box sizes in mm in the respective directions, chemical shift sign is either +1 or -1, and positive chemical shift directions are L, P, and S for the LPS imaging system. The chemical shift amounts in mm in the three respective directions are then calculated as,

$$chemshift_{dir} = -\delta_{ppm} * 10^{-6} * \frac{Resonancefreq}{gamma_{1H} * 10^{-3} * GR_{dir}} \tag{3.2}$$

where $\delta_{ppm}$ is the ppm difference between the shifted and reference metabolites, and the resonance frequency is in Hz. Cr+PCr (3.03 ppm), Glx (2.25 ppm), Cho (3.2 ppm),

mI (3.52 ppm), Lac (1.3 ppm), Lip13a (1.3 ppm), Lip13b (1.3 ppm), and Lip13a + Lip13b (1.3 ppm) metabolite maps and if present a user-defined metabolite map are estimated. The user can change the default value for the metabolite ppm. The corresponding FOV for these metabolites are shifted in space by their respective chemical shift amounts. This module ensures that the binary voxel masks are positioned onto the same coordinate system and co-registered to the reference structural image. The resultant binary masks are saved in the NIfTI format under the ' /coreg_binary_mask' folder.

### 3.2.3 Segmentation

The segmentation module uses FMRIB's Software Library (FSL)-Fast tool to segment the T1w-MRI into CSF, WM, and GM regions. If the anatomical reference image for $^{1}$H-MRSI is T1w-MRI, this module calculates the CSF, WM, and GM fractions at each voxel of all different binary masks, which are FOV placements of every metabolite after chemical shift correction. On the other hand, if the anatomical reference image for $^{1}$H-MRSI is T2w-MRI, the T1w-MRI and CSF, WM, and GM probabilistic maps are first registered to T2w-MRI using FSL-Flirt. Then, the CSF, WM, and GM fractions are calculated for all voxels of different metabolite masks. The tissue fraction calculations of the 3D $^{1}$H-MRSI are modified from Osprey [77], which calculates GM, WM, and CSF fractions for a single-voxel MRS data. If the chemical shift correction is set to "off," the tissue fractions are calculated separately for each voxel. On the other hand, each metabolite will have a shifted box placement if the chemical shift correction is set to "on." As a result, the tissue fractions are calculated separately for each metabolite of individual voxels when the chemical shift correction is "on."

### 3.2.4 CRLB, FWHM, SNR

The CRLB FWHM SNR module reads the LCModel TABLE files of multivoxel $^{1}$H-MRSI data to retrieve the CRLB, FWHM, and SNR information for each voxel. This module also provides sagittal, coronal and axial views of the CRLB, FWHM, and SNR maps for all the slices.

### 3.2.5 Spectral Quality Control

This module provides automatic and manual spectral quality control to select high-quality voxels for the analysis based on the FWHM, SNR, CRLB, and fCSF thresholds provided by the user. The GUI asks the user to determine the cut-off values for FWHM, SNR, CRLB, and fCSF to exclude poor-quality spectra. Each metabolite has a CRLB value provided in TABLE files after LCModel data analysis, indicating the quantification reliability, which were used to exclude spectra based on CRLB. The logical operator "or" was used to automatically exclude the poor spectra. Additionally, the user can manually select the voxels to be included in or excluded from the analysis. The user could also select individual voxels to see its FWHM, SNR, CRLB, and fCSF values.

### 3.2.6 Metabolite Map

LCModel TABLE files are parsed to obtain the concentration values of the metabolites. These results are positioned onto a 3D MR volume with the same image space and properties as the reference anatomical MRI. The off-center, size, and angulation along the anterior-posterior (ap), left-right (lr), and cranial-caudal (cc) directions are considered to create several 3D MR spectroscopic maps including both the concentration and CSF-corrected concentration maps, and their Ins or Cr + PCr ratio maps.

CSF correction is necessary to reduce the partial volume effect in multivoxel MRSI data analysis [30]. The corrected metabolite concentrations are calculated as follows:

$$C = C_0(\frac{1}{1 - V_{CSF}}) \tag{3.3}$$

where C represents the corrected metabolite concentration and $C_0$ the initial metabolite concentration obtained from the LCModel TABLE files. VCSF is the volume fraction of the CSF of each voxel calculated at the segmentation module. The outputs of this module are saved under the 'spectra/nifti' directory.

### 3.2.7 Registration

The registration module enables the user to register the reference anatomical MRI onto the MNI152 brain atlas using the FSL-FLIRT tool to obtain a transformation matrix, which is then used to register the spectral image volumes, including the binary mask of the VOI and all the raw and CSF-corrected concentration or ratio maps onto the atlas. Although the original binary mask of the VOI has all the ones inside and zeros outside, the pixel intensities have a range of probabilistic values ranging between 0 and 1 after registration. The user is asked to provide an inclusion cut-off value for probabilistic maps. Thus, only those pixels that exceed this threshold are considered to be within the VOI and considered for further analysis. The outputs of this module are saved under the ' /spectra/nifti/MNI_Regist_Probabilistic' directory.

### 3.2.8 ROI Analyze

This module enables the user to evaluate the metabolic maps at functional parcellations of the human cerebral cortex on rs-fMRI networks or MNI structural

brain atlas regions and calculates the mean, median, and standard deviation of the chosen concentration map in these brain regions. If the number of pixels in an ROI is greater than the exclusion ratio (given on the ROI module page), then that ROI is included in the analysis of the metabolite of interest, otherwise, it is not. The ROI Analyze module exports all the results in a Microsoft Excel sheet and a '.csv' file.

### 3.2.9 Distributions

This module shows a box plot of a selected metabolite's distribution at a selected region for a visual assessment.

### 3.2.10 Data Acquisition of Example Datasets

Examples of 3D $^{1}$H-MRSI datasets for Oryx-MRSI are available in the ' /Oryx-MRSI/Dataset' folder which is under the GitHub repository. One healthy control and one patient with Parkinson's disease were scanned on a 3T clinical MR scanner (Philips Healthcare, Best, The Netherlands) after obtaining written informed consent. The study was conducted with the approval of the Institutional Review Board. The brain MRI protocol included T1w MRI (TR = 8.31 ms, TE = 3.81 ms, flip angle = 8, acquisition matrix = 256 x 256 x 90, FOV = 240 mm x 240 mm, slice thickness = 1 mm, scan time = 143s), T2w MRI (TR = 10243 ms, TE = 80 ms, flip angle = 90, acquisition matrix = 128 x 128 x 90, FOV = 240 mm x 240 mm x 180 mm, slice thickness = 2 mm, scan time = 3.5 min), and a 3D $^{1}$H-MRSI acquired using a PRESS sequence (TR = 1000 ms, TE = 52 ms, 1000 Hz, 1024 points, data acquisition matrix = 14 x 14 x 3, 588 voxels, FOV = 140 mm x 140 mm x 36 mm, voxel size = 10 mm x 10 mm x 12 mm, total scan time = 8 min). A T2w MRI was used as the reference anatomical MR image for $^{1}$H-MRSI. The excitation, echo, and echo2 directions were along AP, RL, and FH, respectively. The phase-encoding direction (RFOV) was along RL. The chemical shift directions were defined during the data acquisition, which were A, L, and F along AP, LR, and foot-head (FH) for the ex-

ample datasets, respectively. The reference metabolite was NAA at 2.02 ppm. The raw $^{1}$H-MRSI data were quantified with LCModel using a simulated basis set named gamma_press_te52_128mhz_627d.basis provided by the LCModel distributor. Later, brain extracted NIfTI files of T1w MRI, T2w MRI, and the raw data files in SPAR and SDAT format, LCModel outputs, and the screenshots of the $^{1}$H-MRSI data acquisition were saved under ' /Oryx-MRSI/Dataset/Patient_Name' directory. The spectral datasets given in the GitHub repository were evaluated in detail qualitatively, and the exclusion criteria for the example dataset were defined as $<8$, $>0.10$, $>30$, and $>0.30$ for the SNR, FWHM, CRLB, and fCSF values, respectively [118], [119], [120].

MRI brain protocols for Braino GE Phantom trials are given as text files in the GitHub repository, separately. The Braino GE Phantom was scanned on the same scanner with four different trials to assess the chemical shift directions (TR/TE = 1000/52 ms, 3D scan mode, transverse orientation). In the first and second trials, the RFOV was set as RL. The chemical shift directions were defined as A, L, and F along AP, LR, and FH, respectively. The only difference between the first and second trials was the plan scan metabolite, which was set as water and NAA, respectively. In the third and fourth trials, the RFOV was set as AP. The chemical shift directions were A, R, and H along AP, R, and FH, respectively. The plan scan metabolites of the third and fourth trials were water and NAA, respectively.

## 3.3 Results

Figure 3.1 shows the main screen of Oryx-MRSI, where the user can provide the required parameters of the cut- off values of CRLB, fCSF, FWHM, SNR for voxel exclusion criteria, RF bandwidth of the sequence for chemical shift correction, and cut-off value for the probabilistic binary map after registration onto the MNI152 brain atlas. An example NIfTI-MRS data, which is available at 'https://github.com/wtclarke/fsl_mrs', was successfully loaded and visualized (Figure 3.2).

The dataset named K_01 in the GitHub repository was used for the example

data analysis. Oryx-MRSI successfully loaded the example dataset and enabled visualization of the 3D $^{1}$H-MRSI dataset after reading either the raw data (Figure 3.3) or the COORD files (Figure 3.4).

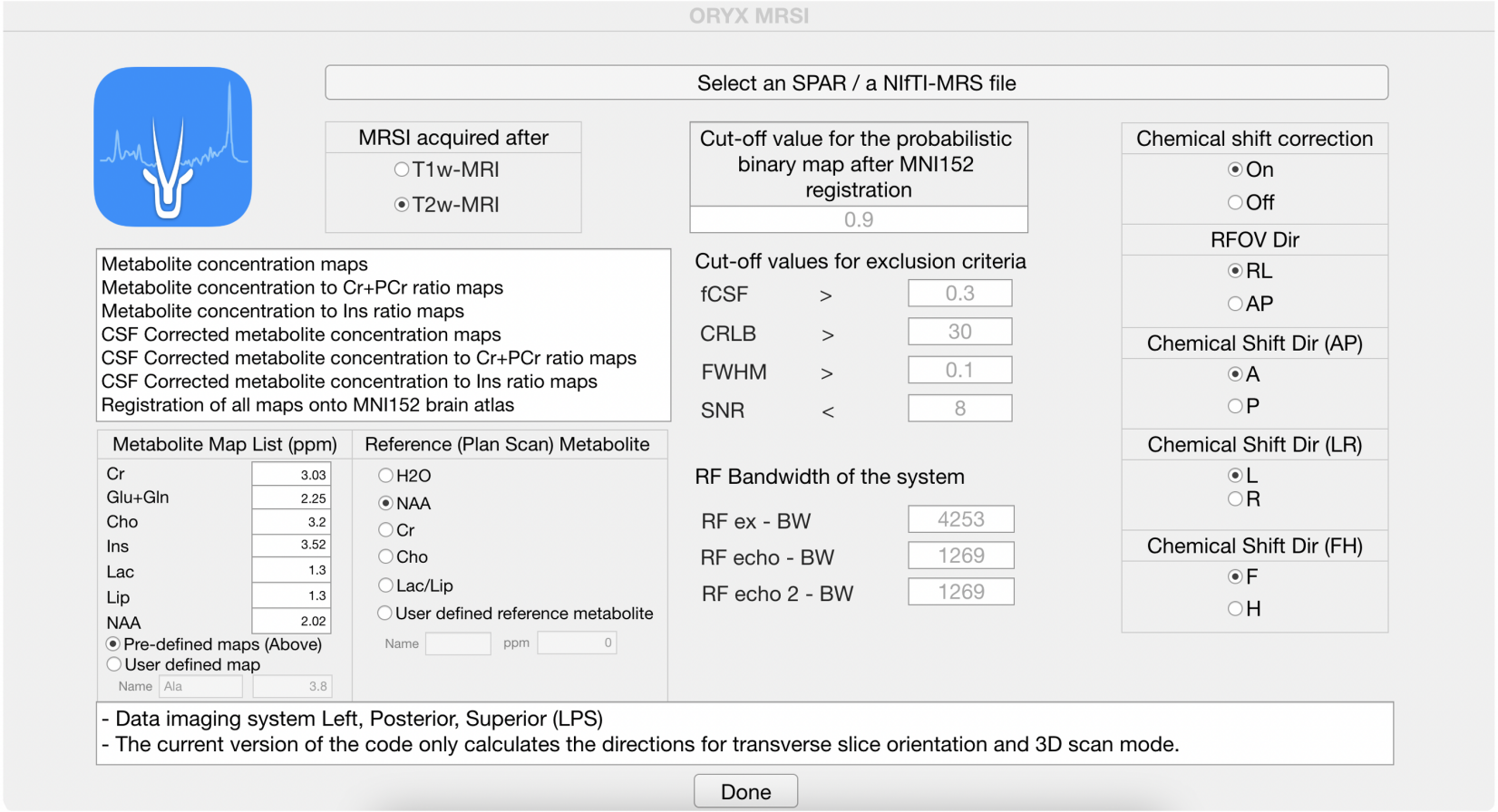


**Figure 3.1** The main screen of Oryx-MRSI where the user could provide the required parameters of cut-off values of CRLB, fCSF, FWHM, and SNR for voxel exclusion criteria, RF bandwidth of the sequence for chemical shift correction, and the cut-off value for the probabilistic binary map after registration onto the MNI152 brain atlas [2].

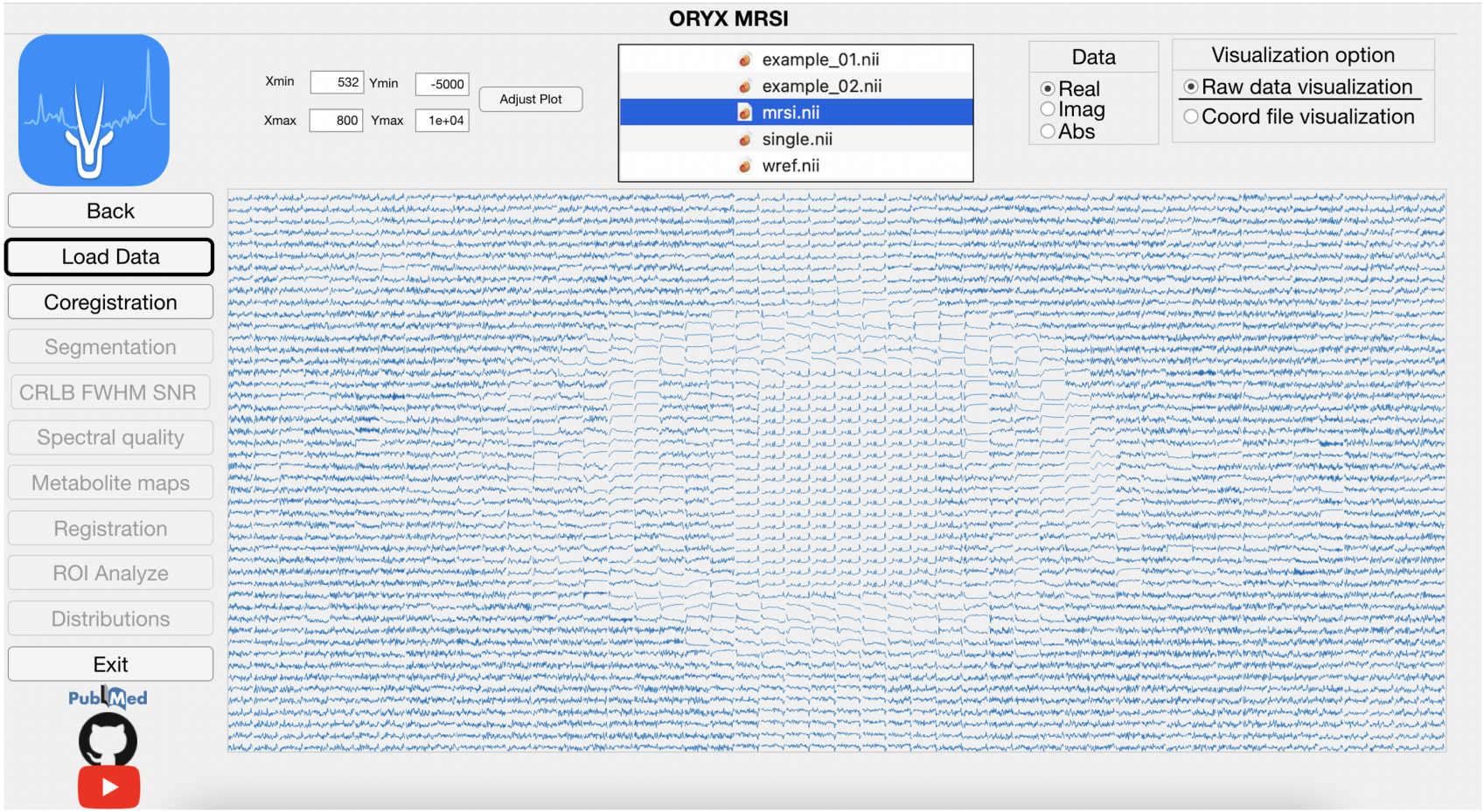


**Figure 3.2** Display of an example NIfTI-MRS data [2].

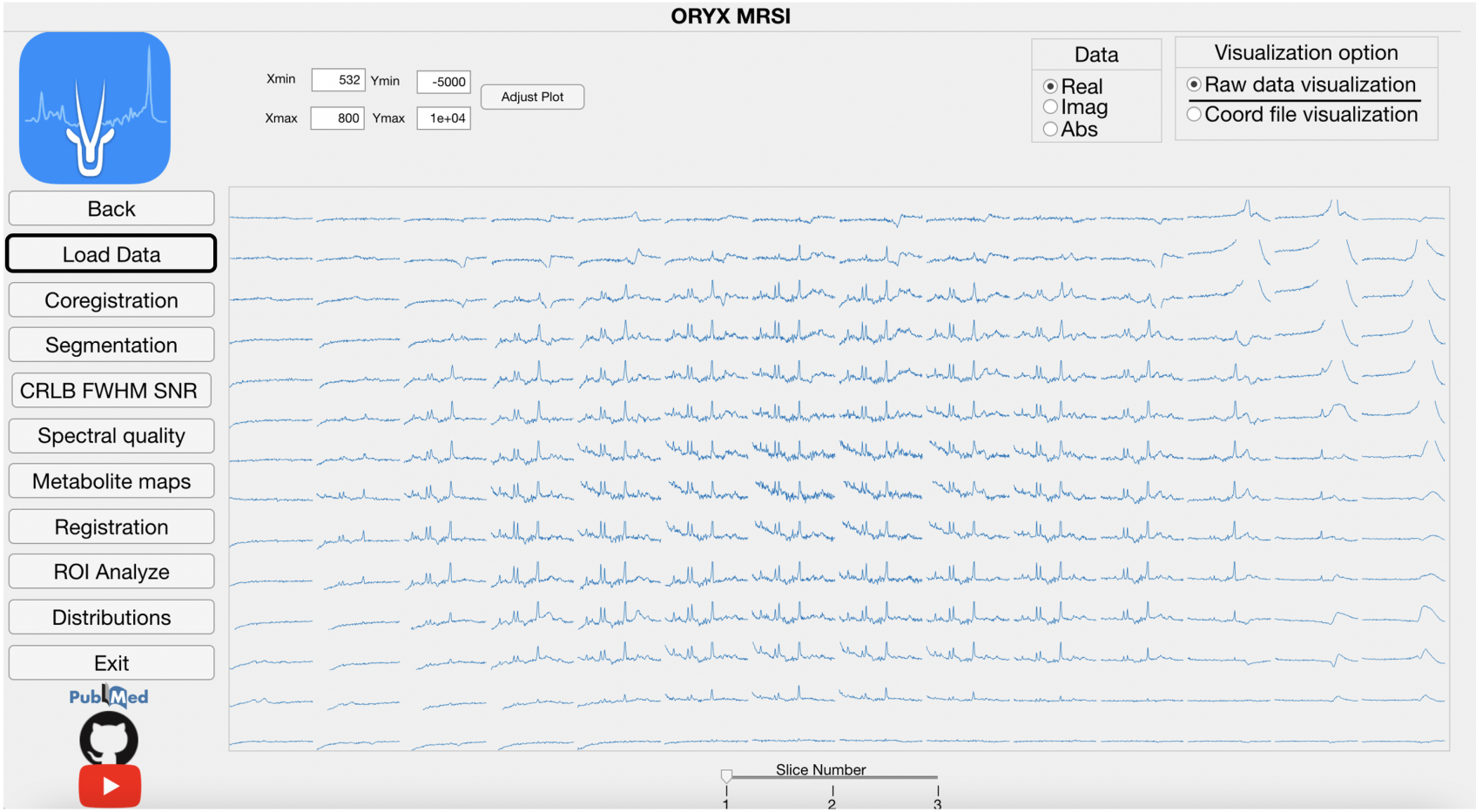


**Figure 3.3** Visualization of the 3D $^{1}$H-MRSI dataset after reading a raw data [2].

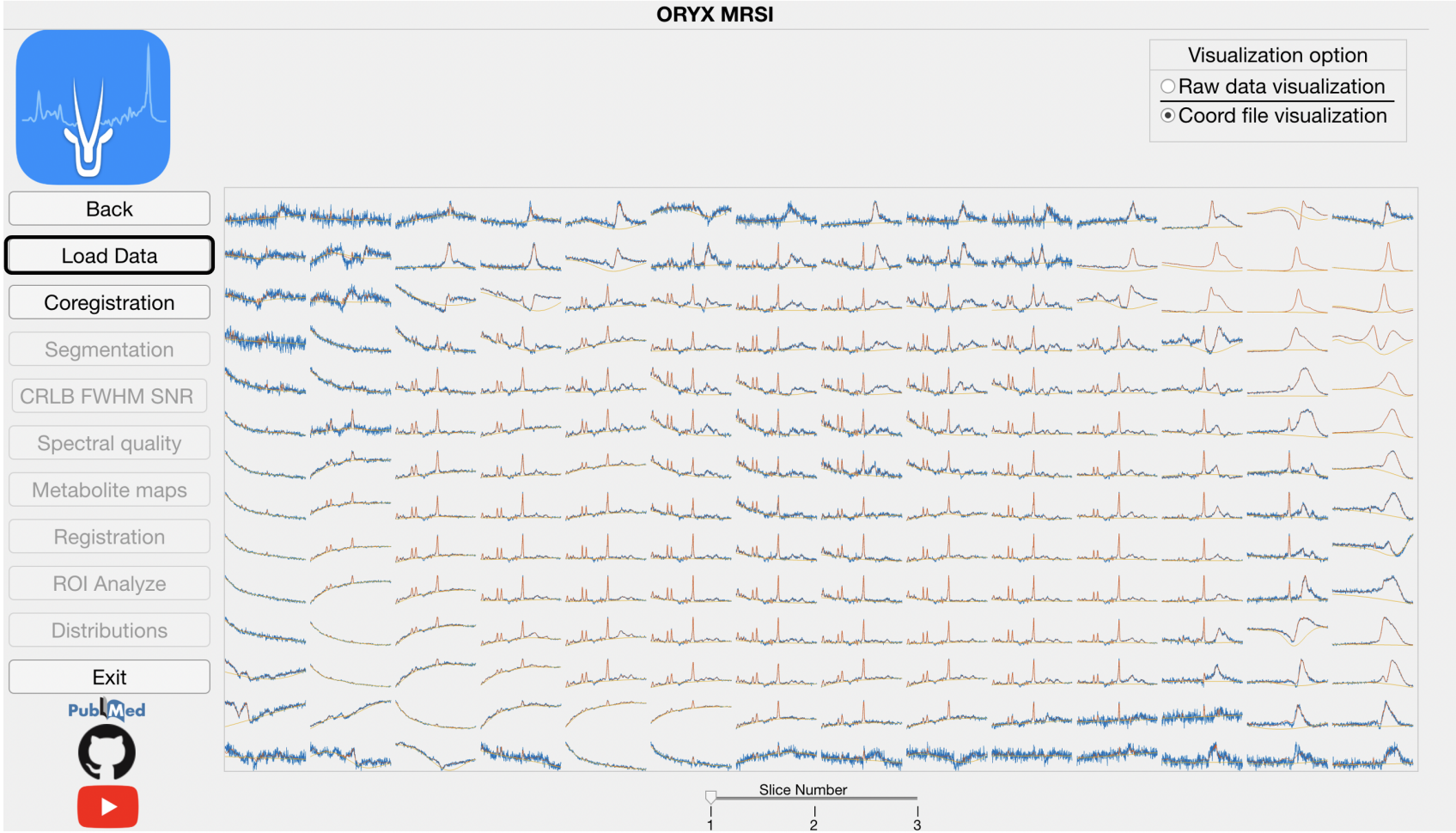


**Figure 3.4** Visualization of the 3D $^{1}$H-MRSI dataset after reading a COORD file (Blue: Raw spectra, Orange: Fitted spectra) [2].

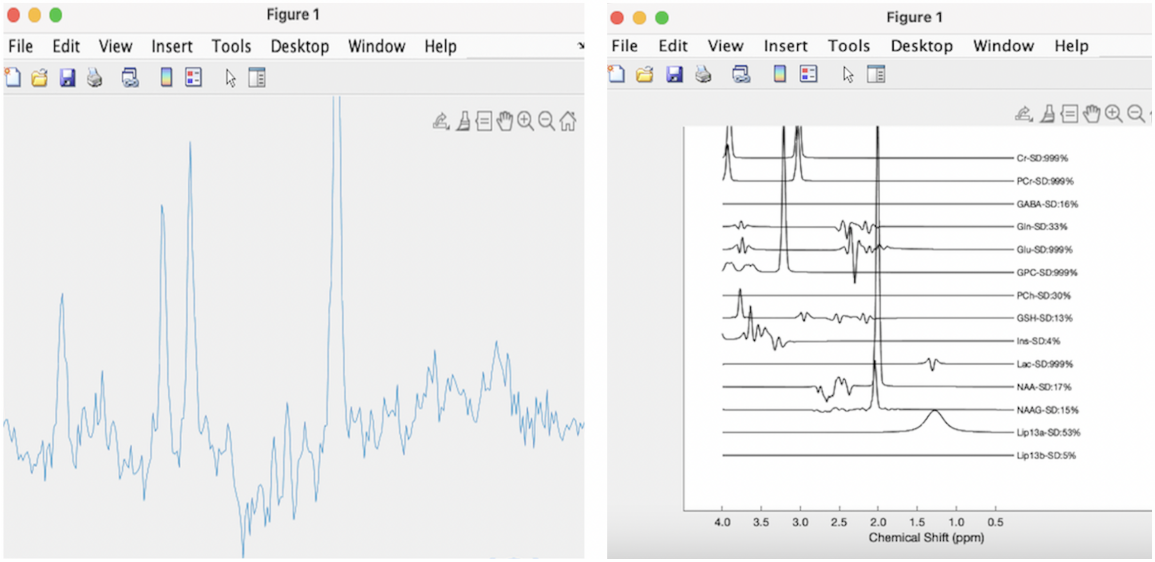


**Figure 3.5** Left: Zooming in on a voxel for a closer view. Right: Visualization of the individual metabolite fits [2].

The software also supported zooming in on a voxel for a closer view (Figure 3.5, left), and visualization of the individual metabolite fits (Figure 3.5, right).

Figures 3.6 and 3.7 show the visualization of the $^{1}$H-MRSI data acquired with the first and second phantom trials, which were conducted with water and NAA as the plan scan metabolites, respectively. All metabolites were shifted towards the left direction when water was set as the reference frequency. However, Cho was shifted towards the right and Lac was shifted towards the left direction when NAA was used as the reference frequency. The chemical shift amount in the AP direction was less than in the other directions due to the higher RF pulse bandwidth.

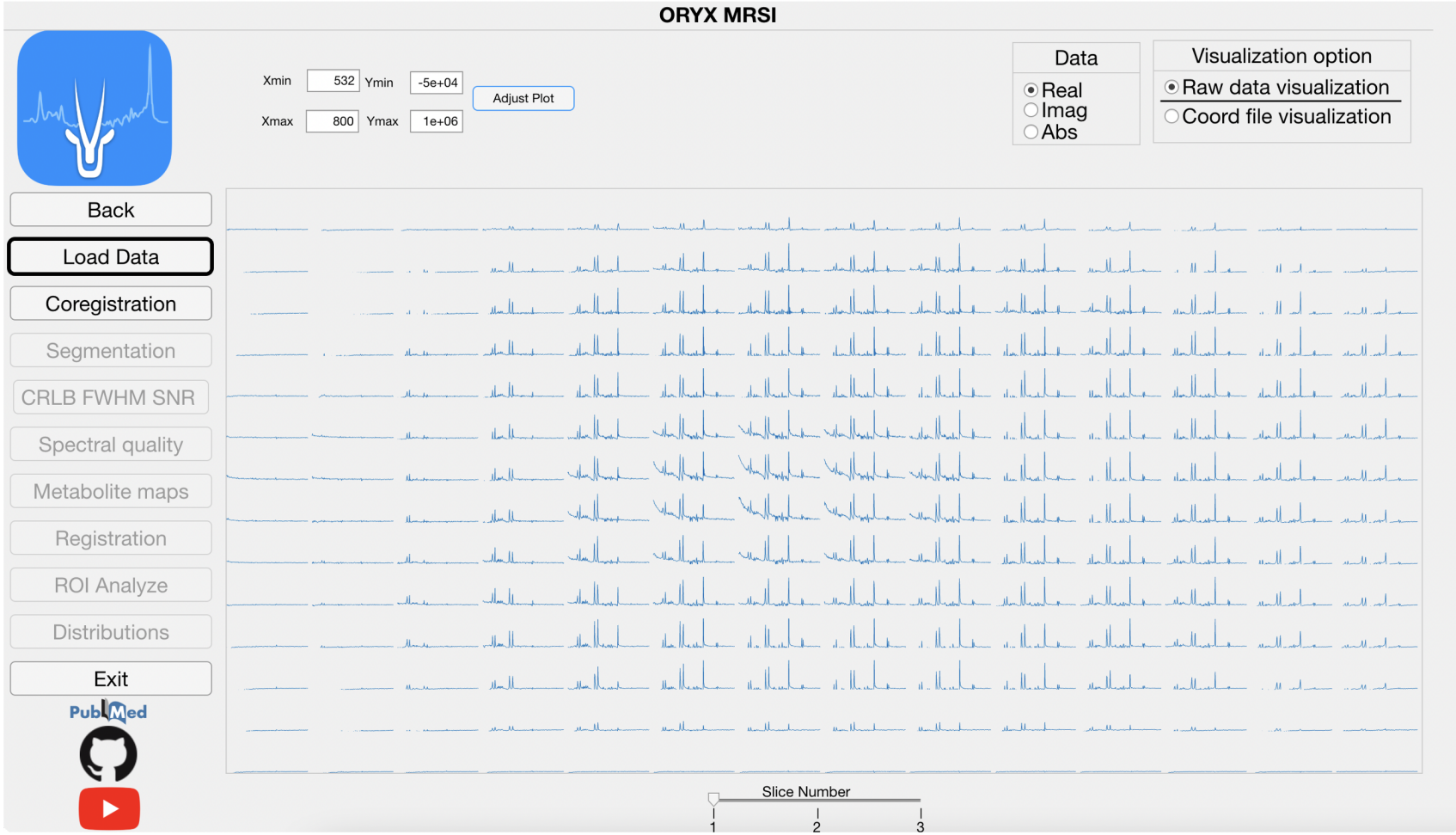


**Figure 3.6** Two slices of the $^{1}$H-MRSI data acquired with the first phantom trial, which were conducted with water as the plan scan metabolites [2].


**Figure 3.7** Two slices of the $^{1}$H-MRSI data acquired with the second phantom trials, which were conducted with NAA (B) as the plan scan metabolites [2].

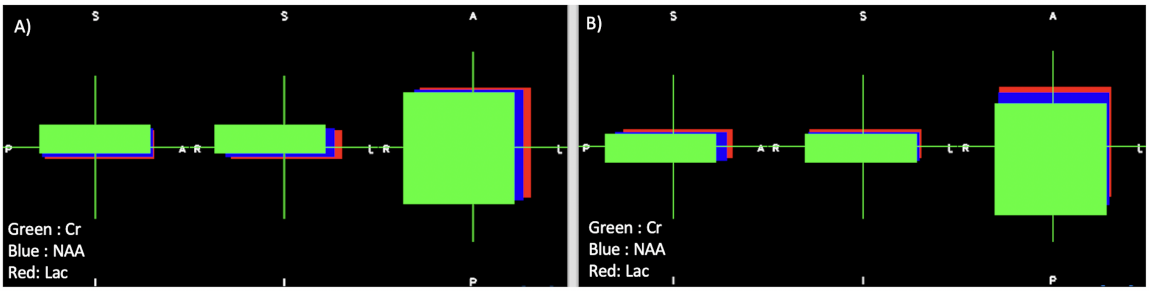


**Figure 3.8** The chemical shift directions of the Cr (green) and Lac (red) boxes when NAA (blue) was set as the reference metabolite on the second phantom trial ((A) RFOV = RL, chemical shift directions = A, L, F), and fourth phantom trial ((B) RFOV = AP, chemical shift directions = A, R, H) [2].

Figure 3.8 shows the chemical shift directions of the Cr (green) and Lac (red) boxes when NAA (blue) was set as the reference metabolite on the second phantom trial(A, RFOV = RL, chemical shift directions = A, L, F), and fourth phantom trial (B, RFOV = AP, chemical shift directions = A, R, H). The Lac box was shifted towards (A, L, F) and (A, L, H) directions, whereas there were shifts towards (P, R, H) and (P, R, F) for Cr in the second and fourth phantom trials, respectively. All the calculated chemical shift directions were consistent with those displayed on the Philips MR scanner console.

Figure 3.9 shows the placements of the different metabolite FOV boxes (green: Cr+PCr, blue: NAA+NAAG, red: Cho, pink: Glx, brown: mI) after chemical shift correction (first row). The second row shows the distributions of metabolite to Cr+PCr ratio maps both estimated by LCModel and after chemical shift correction at the frontal lobe of the 'K_01' dataset given at GitHub. If the chemical shift correction option was off," the metabolite maps were generated based on the LCModel estimations. On the other hand, the maps were spatially shifted by the corresponding chemical shift amount, when the chemical shift correction option was 'on.' Only the voxels at the intersection of the shifted boxes were compared for the metabolite to Cr + PCr ratio maps. The mean ($\pm SD$) values of the NAA+NAAG, Cho, Glx, and Ins to Cr+PCr ratios directly estimated by LCModel at the frontal lobe were 0.32 ± 0.08, 1.91 ± 1.15, 1.45± 0.82, and 0.77 ± 0.34, respectively.

On the other hand, the mean ($\pm SD$) values of the NAA+NAAG, Cho, Glx, and

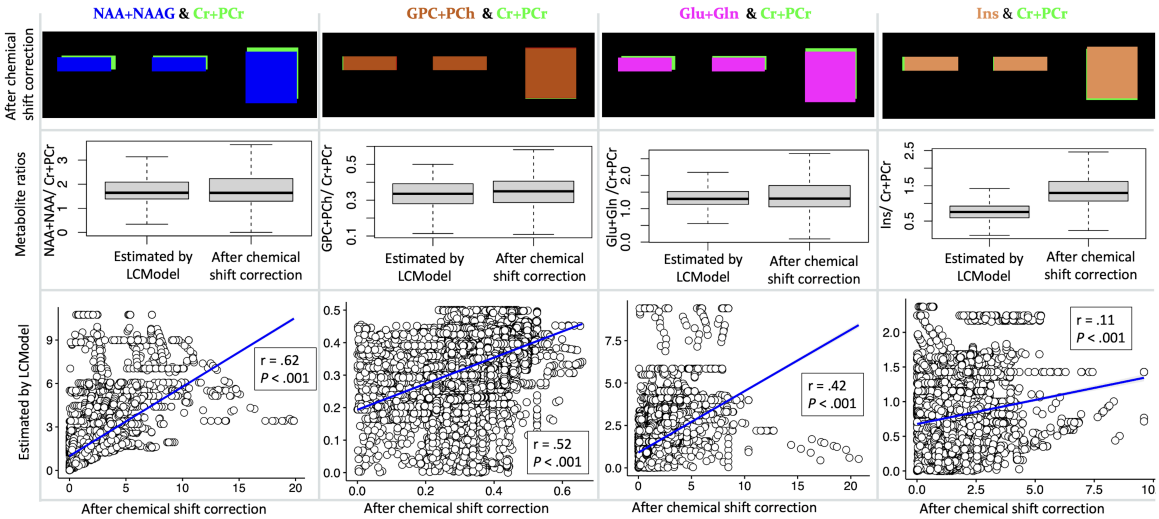


**Figure 3.9** The FOV box placements after chemical shift correction (first row). The distributions (second row), and the correlations (third row) of NAA+NAAG, Cho, Glx, and Ins to Cr+PCr ratios estimated by LCModel and after chemical shift correction [2].

mI to Cr+PCr ratios at the same region after chemical shift correction were 0.33±0.09, 1.93±1.44, 1.52±1.07, and 1.41±0.74, respectively. Additionally, the third row shows the correlations of the metabolite to Cr+PCr ratios estimated by LCModel and after chemical shift correction calculated using a Spearman rank correlation coefficient. There were positive correlations between NAA+NAAG/Cr+PCr ($r = 0.62$, $p < 0.001$), Cho/Cr+PCr($r=0.52$,$p<0.001$),Glx/Cr+PCr ($r = 0.42$, $p<0.001$) and Ins/Cr+PCr ($r = 0.11$, $p < 0.001$) ratios estimated by LCModel directly and their recalculated values after the chemical shift correction.

Figure 3.10 shows example binary FOV masks of Cr+PCr and Lac placed on an anatomical T2-weighted MRI, which indicates the importance of taking chemical shift into account for $^{1}$H-MRSI. Figure 3.11 depicts the FOV and a single voxel (in white, slice = 1, row = 1, and col = 1) out of the 3x14x14 voxels for the NAA+NAAG (blue box), Cr + PCr (green box), and Lac (red box) metabolites in all three views.

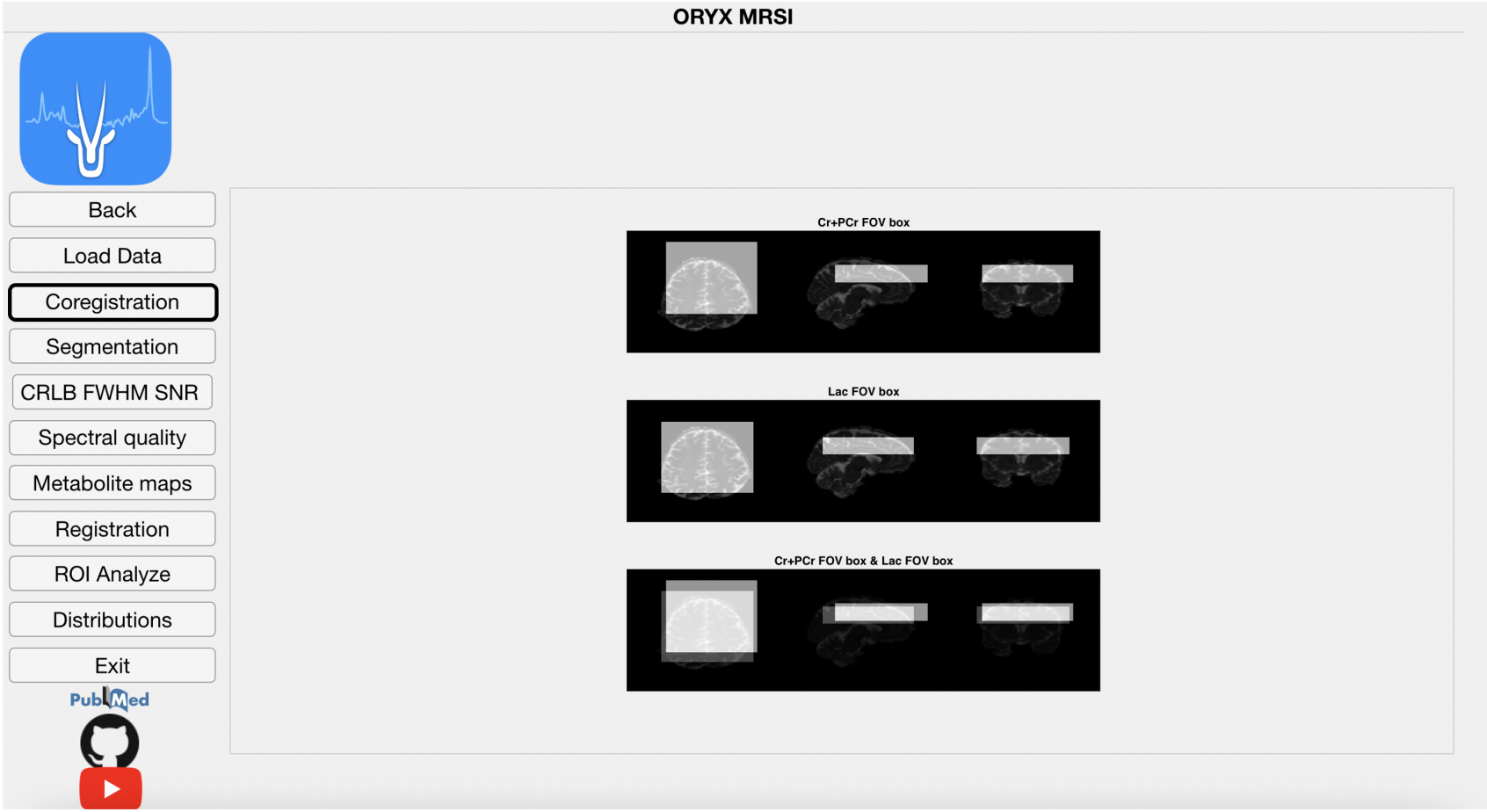


**Figure 3.10** Example binary FOV masks of Cr+PCr and Lac placed on an anatomical T2-weighted MRI [2].

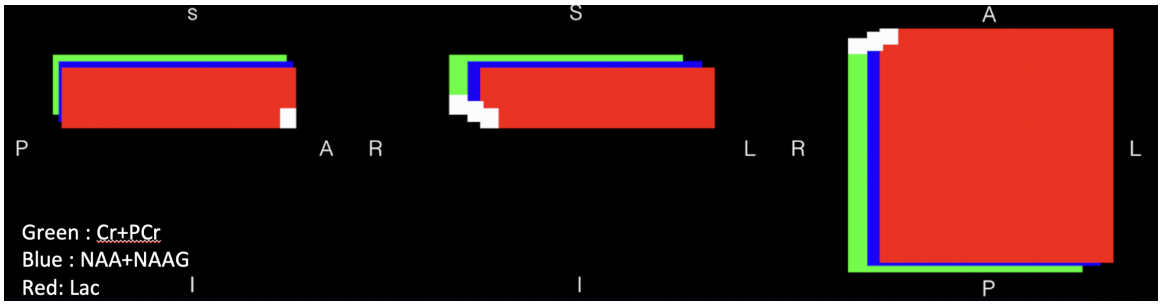


**Figure 3.11** The FOV and a single voxel (in white, slice = 1, row = 1, and col = 1) out of 3 x 14 x 14 voxels for the NAA + NAAG (blue box), Cr + PCr (green box), and Lac (red box) metabolites [2].

Figures show the fCSF, fWM, and fGM maps for the NAA+NAAG box at slice 1 of the example dataset (Figure 3.12) along with the CRLB, FWHM, and SNR maps (Figure 3.13), and the voxels included in the analysis after the quality check (Figure 3.14).

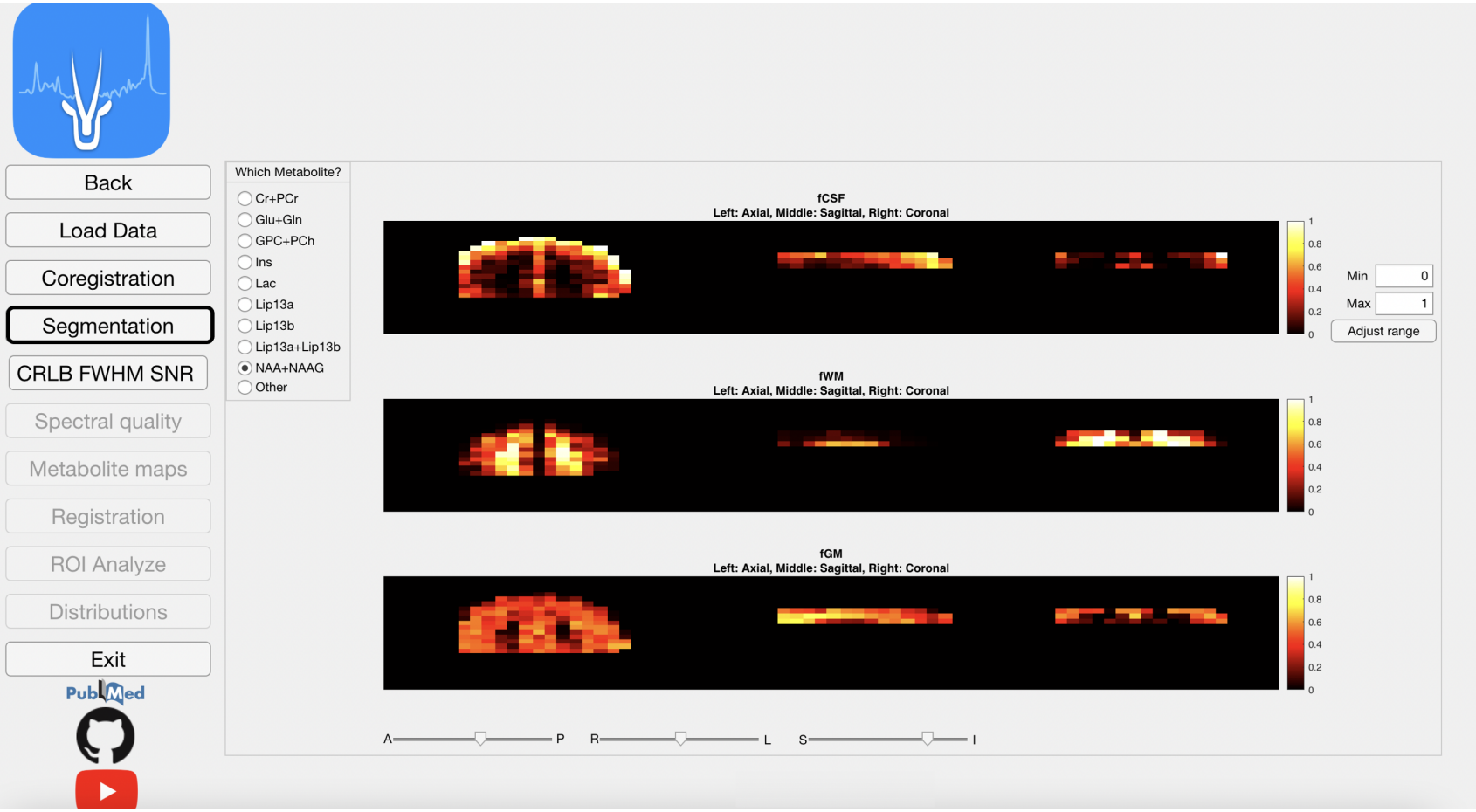


**Figure 3.12** (The fCSF, fWM, and fGM maps of the NAA+NAAG box at slice 1 of the example dataset [2].

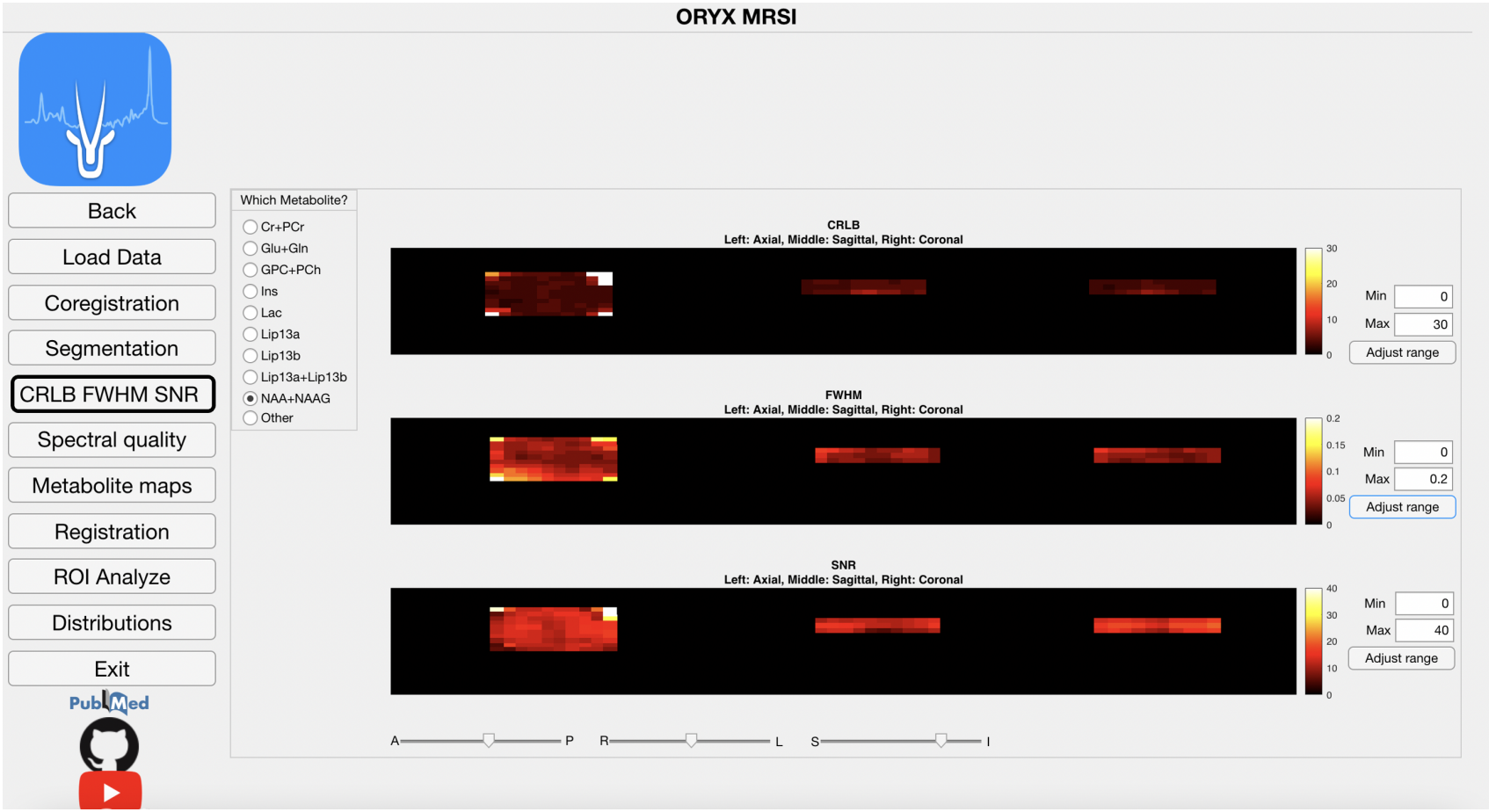


**Figure 3.13** The CRLB, FWHM and SNR maps at slice 1 of the example dataset [2].

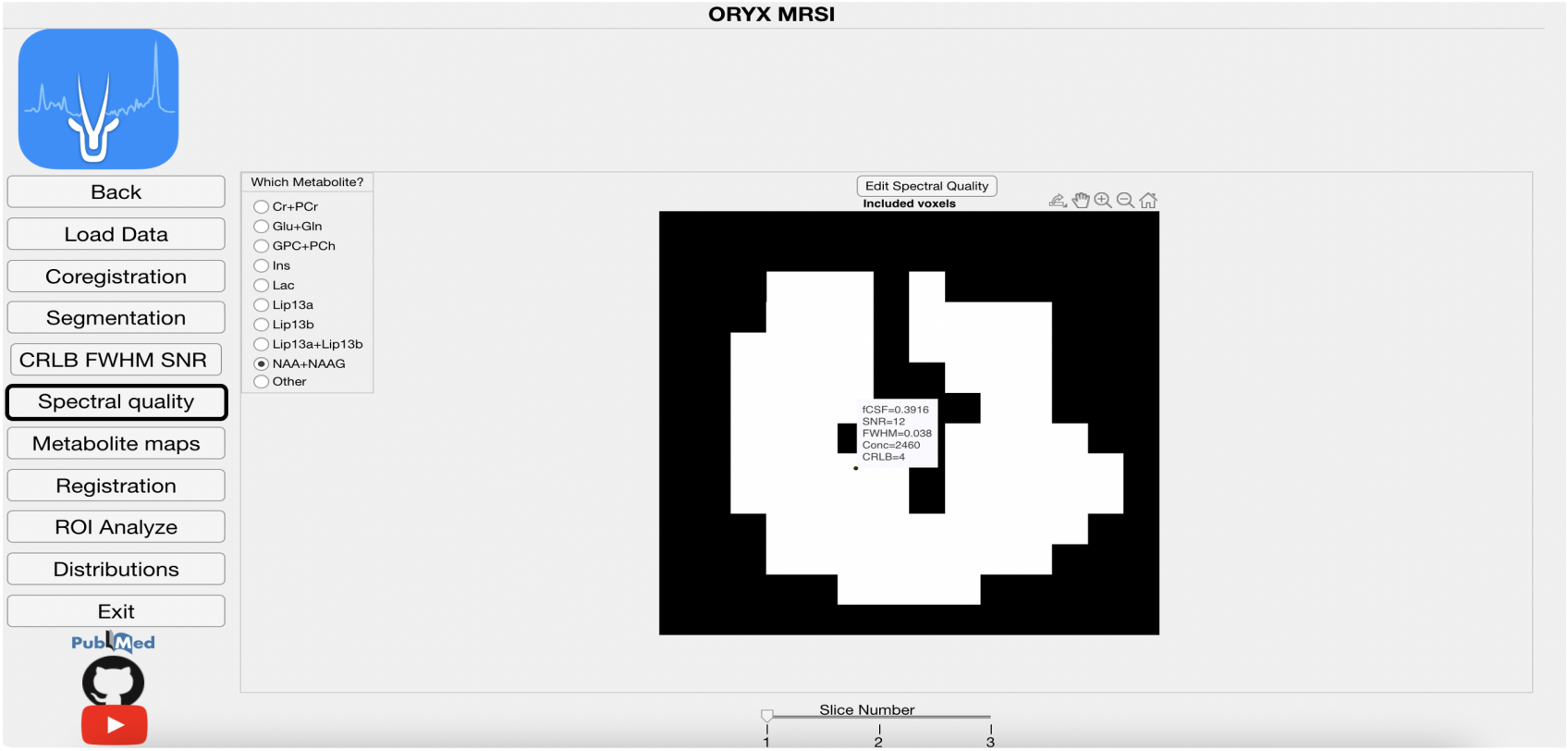


**Figure 3.14** The voxels included in the analysis after the quality check at slice 1 of the example dataset [2].

An NAA+NAAG concentration map was generated using the metabolite map module (Figure 3.15). Additionally, this module allows for the visualization of CSF corrected concentration maps, and metabolite to Ins or Cr+PCr ratio maps. An NAA+NAAG concentration map after registration onto the MNI152 brain atlas is shown in Figure 3.16.

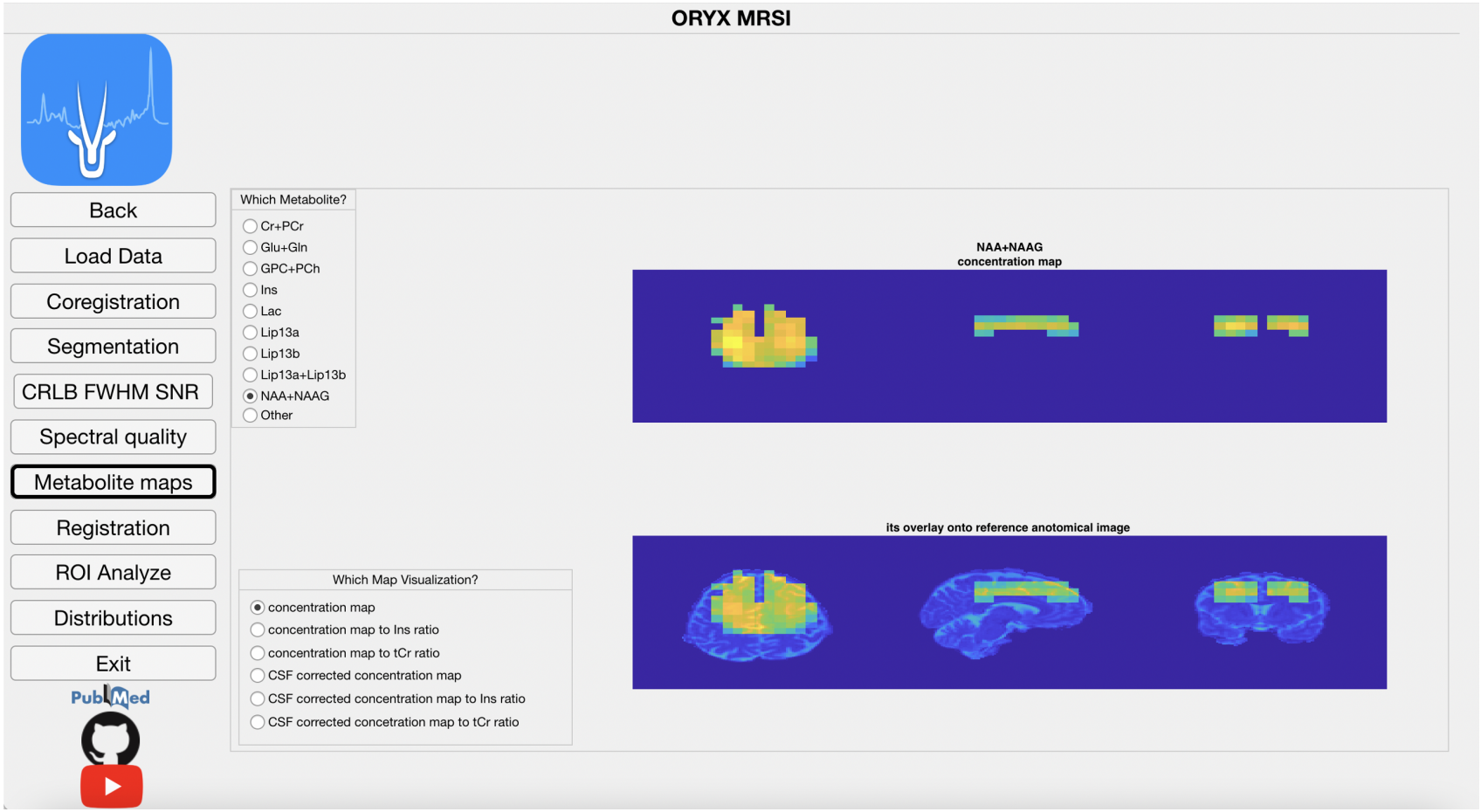


**Figure 3.15** An NAA+NAAG concentration map generated using the metabolite map module [2].

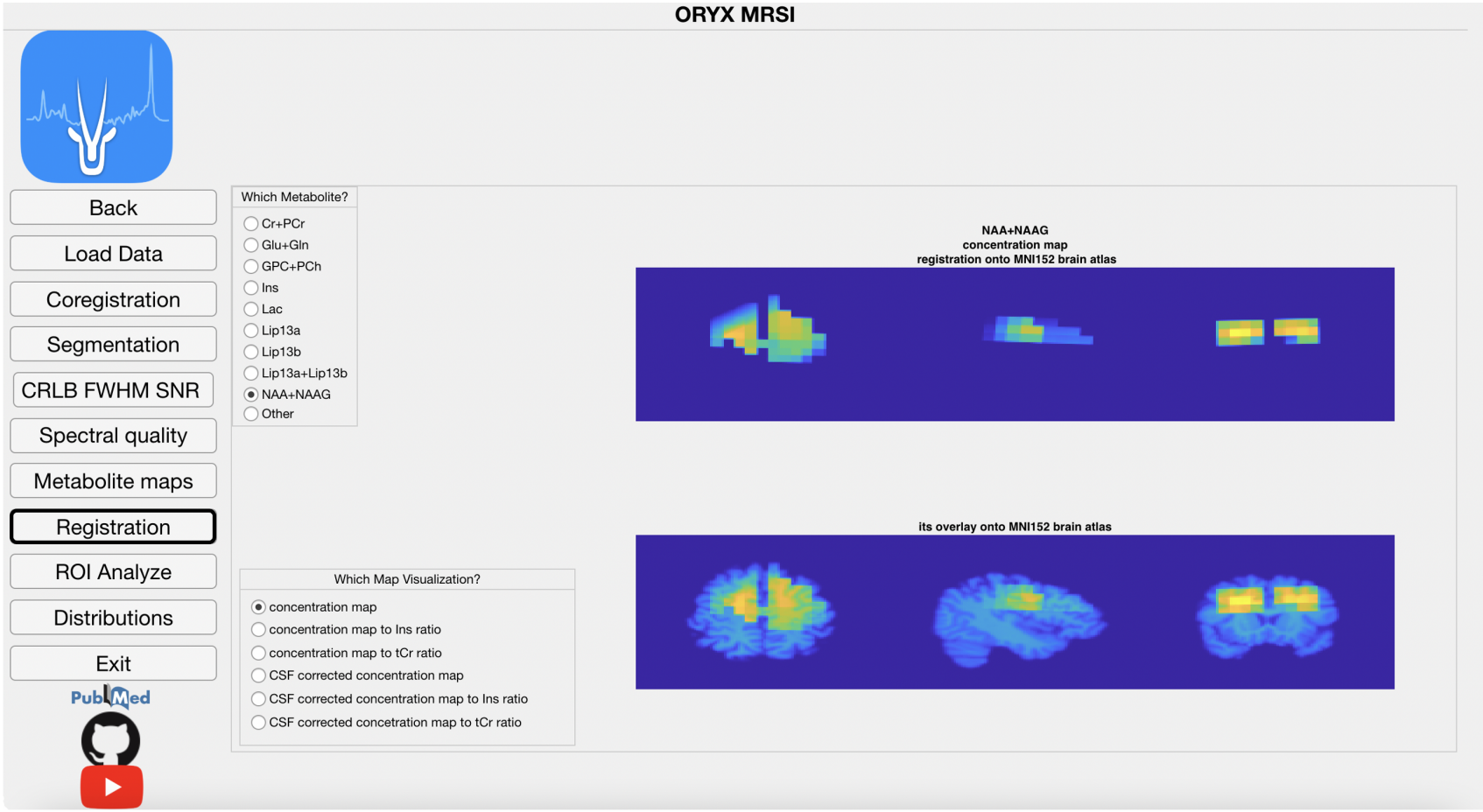


**Figure 3.16** The NAA+NAAG concentration map after registration onto the MNI152 brain atlas [2].

Figure 3.17 shows an example NAA+NAAG concentration map (A), which is overlaid onto MNI brain atlas (B) at the brain connectivity networks (C).

Figure 3.17.D depicts NAA+NAAG concentration map at the left somatomotor $6^{th}$ area and its box plot distribution (Figure 3.18). The module results were validated with Philips MR scanner and LCModel software for load data, Philips MR scanner for co-registration and chemical shift correction, and Osprey software [77] for segmentation.

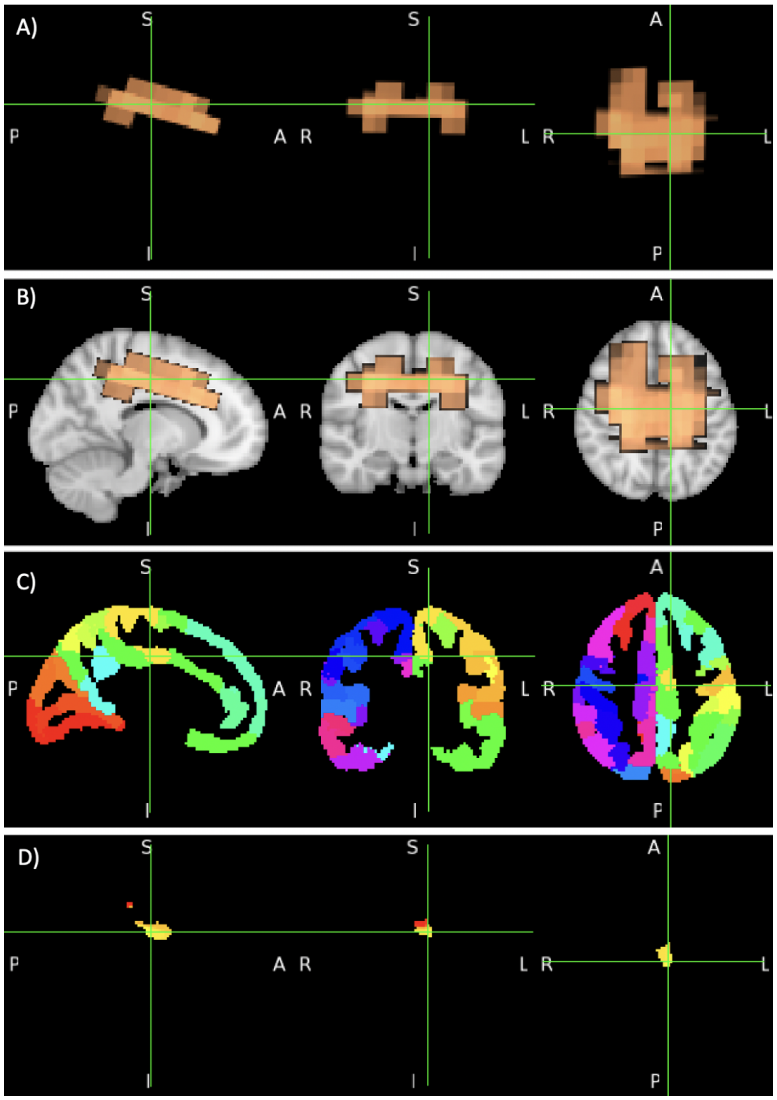


**Figure 3.17** An example NAA+NAAG concentration map (A), which is overlaid onto MNI brain atlas (B) at the brain connectivity networks (C). The NAA+NAAG concentration map located at the left somatomotor $6^{\text{th}}$ area (D) [2].

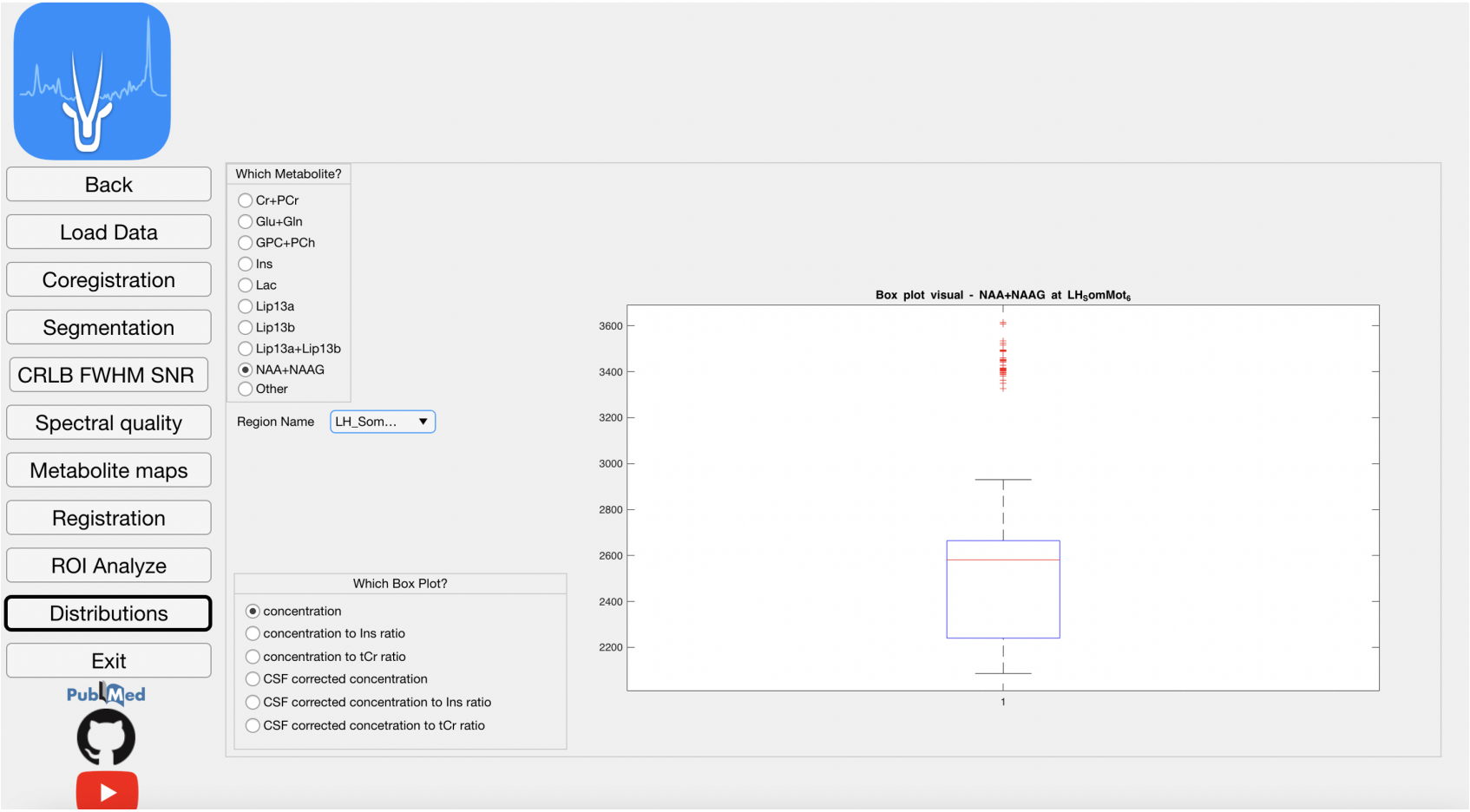


**Figure 3.18** An example box plot distribution of NAA+NAAG concentration map [2].

## 3.4 Discussion

There have been several multivoxel $^{1}$H-MRSI studies that have employed data analysis pipelines including automatic and manual data quality control, chemical shift correction, tissue fraction calculation, metabolite map generation and registration onto common brain atlases, and ROI analysis [81], [121], [122], [123], [124], [88], [125], [126]. However, a standardized data analysis software has not yet been developed that can execute all these steps for the analysis of 3D $^{1}$H-MRSI data. This study presents Oryx-MRSI, which is an open-source MATLAB-based end-to-end pipeline for complementary MRSI data analysis after data quantification. The necessary input files for MRSI data analysis in Oryx-MRSI are raw MRSI data (SPAR - SDAT or NIfTI-MRS format), the anatomical MR images saved in NIfTI format, and LCModel outputs including COORD and TABLE files. Oryx-MRSI supports chemical shift and tissue-fraction corrections and the generation of MNI-registered metabolite maps after considering several data quality criteria. Importantly, all metabolite map outputs are stored in a standard medical image file type, NIfTI, which is a common data storage format for neuroimaging that can easily be visualized using FSLEyes [127], SPM [94], MRICron [128], or NiBabel [129] in Python. Additionally, Oryx-MRSI generates brain-atlas-based statistical analysis results.

Many studies have reported the importance of CSF correction after anatomical image segmentation [30], [130], [131], [132], [133]. While LCModel [75] does not take into account partial volume effect, Osprey [77], FSL-MRS [76], and MRSpant [78] provide corrections for it. Similarly, Oryx-MRSI also supports partial volume fraction calculations and CSF correction. Another important factor in $^{1}$H-MRSI data quantification is the chemical shift effect [72], [31]. As a result, Oryx-MRSI has a chemical shift correction module. However, it is important to note that chemical shift correction formula is dependent on the specifics of the spectroscopy sequence. Additionally, although the PRESS sequence suffers from this artifact, semi-LASER sequences have better localization performance. Our analysis results revealed that although the metabolite to Cr+PCr ratios estimated by LCModel directly and their corresponding values after chemical shift correction were correlated, they had significant differences in their

values, because LCModel does not consider the chemical shift, while Oryx-MRSI re-calculates metabolite concentrations to tCr or mI ratios at every voxel after chemical shift correction.

The production of metabolite maps registered to standardized brain atlases, such as the MNI152 brain atlas, is required to facilitate group-based statistical analysis [134] or to analyze spectroscopic data along with other MR images, such as arterial spin labeling (ASL) MRI. FSL-MRS, Osprey, and MRSpant co-register MRS data onto the reference anatomical MRI to compute the CSF fraction and correct for it, but they currently do not support metabolite map generation, registration onto a common brain atlas, and ROI analysis. On the other hand, Oryx-MRSI has these additional features.

Another requirement for reliable data analysis is automated quality control of the spectra based on the linewidth, SNR, and accuracy of the peak fits [135]. The CRLB is commonly employed to assess the quality of the data quantification. However, Kreis reported that the use of CRLB values to assess the spectral quality might affect the resultant findings [136]; hence, we enabled Oryx-MRSI to assess the effects of different CRLB thresholds on data analysis.

This study had some limitations. It is necessary to note that the chemical shift directions and formulations provided in the Methods section were calculated for a single MR vendor, and it is necessary to validate these formulations for different vendors. Additionally, Oryx-MRSI currently only supports transverse slice orientation and 3D scan mode. Moreover, LCModel data quantification results are currently needed to activate FWHM and SNR, spectral quality, metabolite maps, registration, and ROI analyze sections. Oryx-MRSI could be installed and run only on macOS and Linux, because FSL does not directly run on Windows operating systems but requires a Windows Subsystem for Linux (WSL). Additionally, Oryx-MRSI currently supports ROI based analysis, and a voxel-based statistical analysis module will be developed in the future. Oryx-MRSI will be continuously updated to provide support for different MR vendors, and possible integration with earlier open-source MRS data analysis tools.

## 3.5 Conclusions

Oryx-MRSI is a fully automated open-source software for comprehensive data analysis of 3D $^{1}$H-MRSI that includes specific modules for automated spectral quality control, metabolite map production, co-registration with anatomical MRI, segmentation of anatomical MRI for CSF fraction correction, registration onto MNI152 brain atlas, and ROI analysis. The metabolic map outputs produced by Oryx-MRSI supports concurrent evaluation of MRSI data along with other MR modalities at brain parcellations defined on MNI152 brain atlas and could enable group-based statistical analysis. As a result, Oryx-MRSI might facilitate more common use of $^{1}$H-MRSI in clinical settings.

# 4. IDENTIFICATION OF METABOLIC CORRELATES OF MILD COGNITIVE IMPAIRMENT IN PARKINSON'S DISEASE USING MAGNETIC RESONANCE SPECTROSCOPIC IMAGING AND MACHINE LEARNING

*This chapter presents a detailed study for the analysis of multi-voxel $^{1}$H-MRSI data in PD patients, and identifies metabolic correlates of mild cognitive impairment in PD using machine learning.*

## 4.1 Rationale

Multi-voxel $^{1}$H-MRSI provides a simultaneous assessment of multiple brain regions and a more comprehensive metabolic profiling of the brain tissue. The main aim of this study was to identify possible objective metabolic biomarkers of early cognitive decline in PD using $^{1}$H-MRSI assessed at several regions of the intrinsic connectivity networks (ICNs), which have been suggested for mapping large-scale connectivity networks in the human cerebral cortex using rs-fMRI [137]. This study included spectroscopic mapping at various ICN parcellations [95] of the human brain after considering the chemical shift correction and automated spectral quality control based on FWHM, SNR, CRLB, and CSF fraction. Our secondary aim was to apply supervised machine learning algorithms to classify HC, PD-CN, and PD-MCI patients based on metabolic findings. The contents of this chapter has been published at Magma journal [3].

## 4.2 Materials and Methods

### 4.2.1 Subjects

This prospective study was approved by Istanbul University, Istanbul Faculty of Medicine, Clinical Research Ethics Committee, and written informed consent was obtained from all participants. Eighty-seven subjects (41 PD-MCI, 27 PD-CN, and 19 HC) were recruited from the patients referred to the Movement Disorders outpatient clinic at the Behavioral Neurology and Movement Disorders Unit of the Department of Neurology. HC were most often the partners of the patients or volunteering employees of the department. Each patient was classified as PD-CN or PD-MCI by experienced behavioral neurology and movement disorder specialists. PD diagnosis was according to the UK Brain Bank criteria [138], and PD-MCI diagnosis was according to the MDS Task Force guidelines (abbreviated assessment) [139]. PD-MCI patients were defined as those who received a score of $<83$ from the ACE-R test [140]. Participants with a history of a major psychiatric or neurological disorder and less than five years of education were excluded from the study. The remaining 76 subjects (16 HC, 26 PD-CN, and 34 PD-MCI) were matched according to their age, gender, and education.

### 4.2.2 Neuropsychological Tests and Rating Scales

A screening and neuropsychological test battery, including the Geriatric Depression Scale (GDS) [141], Movement Disorder Society Unified Parkinson's Disease Rating Scale (MDS-UPDRS) [99], MMSE [101], ACE−R [100], Montreal Cognitive Assessment (MOCA) [142], Stroop task [102], JLO [103], SDMT [104], and WCST [105] were applied to all participants to screen for depression and general cognition, to quantify the general PD symptoms, and to assess specifically the cognitive domains of executive functioning, visual-spatial functions, and attention. The Hoehn & Yahr scale was also used for staging the severity of PD.

### 4.2.3 MR Data Acquisition and Post-Processing

A brain MRI protocol that included T1w MRI acquired with 3D Turbo Field Echo (TFE) (TR = 8.4 ms, TE = 3.9 ms, flip angle = 8, acquisition matrix = 256 x 256 x 180, Field of view (FOV) = 250 mm x 250 mm, slice thickness = 1 mm, scan time = 6 minutes), T2w MRI (TR = 10243 ms, TE = 80 ms, flip angle = 90, acquisition matrix = 128 x 128 x 90, FOV = 240 mm x 240 mm, slice thickness = 2 mm, scan time = 3.5 minutes) and $^{1}$H-MRSI was performed on a 3T clinical MR scanner (Philips Healthcare, Best, Netherlands). T2w MRI was used for spectroscopic box placement as the reference image. 3D $^{1}$H-MRSI data were acquired using the PRESS sequence in two consecutive scans by experienced spectroscopists to cover a large portion of the brain while avoiding shimming difficulties, susceptibility artifacts, and lipid contamination (TR = 1000 ms, TE = 52 ms, spectral bandwidth=1000 Hz, 1024 points; RF pulse bandwidths = 4253 Hz and 1269 Hz for the excitation and the two refocusing pulses, respectively; data acquisition matrix (superior box) = 14 x 14 x 3 and 588 voxels, data acquisition matrix (inferior box) = 12 x 12 x 3 and 432 voxels, FOV (superior) = 140 mm x 140 mm x 36 mm, FOV (inferior) = 120 mm x 120 mm x 36 mm, voxel size = 10 x 10 x 12 mm, total scan time = 16 min). The water was suppressed by applying two frequency selective RF pulses followed by spoiler gradients, and second-order shimming was applied before data acquisition. Spatial saturation bands were also placed around the PRESS box to suppress lipid at the scalp area.

Raw $^{1}$H-MRSI data were exported and analyzed offline. All spectral voxels were qualitatively assessed before the data analysis. The LCModel (version 6.3-1L) [75] was used to automatically fit a simulated basis set to each spectrum to obtain the spectral peak intensities and SD including mI, and four composite peak intensities (total choline (tCho=GPC+PCh), total creatine (tCr=Cr+PCr), total NAA (tNAA=NAA+NAAG), and Glx. The basis spectra were provided by the LCModel distributor for our specific PRESS sequence (TE=52 ms) on a Philips 3T MR scanner, and it was simulated in GAMMA using the chemical shifts and coupling constants defined by Govindaraju et al. [45] and ideal (hard) pulses. Figure 4.1 shows the sagittal views of $^{1}$H-MRSI FOVs (red) and PRESS selected boxes (green) (a), the spectra of

a selected region (blue) (b), and a single spectrum example along with some of the LCModel quantification results (pink) (c) for a 66−years−old male PD−MCI patient.

Oryx−MRSI written in MATLAB (The Mathworks Inc., Natick, MA) was used to process the MRSI data [2], and Figure 4.2 shows the code workflow. First, the brain extraction tool (BET) [143] of FSL [92] was called within Oryx-MRSI for skull stripping of the T1w MRI and the reference T2w MRI (Figure 4.2.a). Then, T1w MR images were segmented to generate CSF, GM, and WM images using FSL (Figure 4.2.b). Afterwards, T1w MRI data were co-registered onto the reference T2w MRI, and a transformation matrix was generated (Figure 4.2.c shown with *), which was then used to co-register CSF, GM, and WM images onto the reference images (Figure 4.2.c shown with **). The orientation and position information of the spectral FOV were retrieved from the MRSI data header. The location information of each spectroscopic voxel was then calculated automatically, considering the number of slices, rows, and columns (Figure 4.2.d). Then, the FOV box was positioned into a 3D grid in accordance with the location and size of the reference T2w MRI (by considering the off-center region of interest (ROI), size, and angulation along the ap, lr, and cc directions) to get binary location masks of metabolites at the same resolution with T2w-MRI (Figure 4.2.e). PRESS MRSI suffers from the chemical shift artifact. Therefore, the chemical shift misregistration amount was calculated for each metabolite of interest, considering that the center of the localization pulses was set to NAA frequency, and the binary location masks of metabolites were shifted in space by their corresponding chemical shift amounts [31] using Oryx−MRSI (please refer to the original manuscript for further details). As an example, the blue box represents the NAA box, the green represents the Cr box, and the red represents the lipid box after chemical shift correction in Figure 4.2.f. Afterwards, the volume fractions within each voxel of the binary localization masks were calculated (Figure 4.2.g). The LCModel TABLE files were parsed using a text reader to obtain the spectral peak intensities, CRLB, SNR, and FWHM (Figure 4.2.h). Afterwards, a MATLAB structure was created to store all metabolic information, including the spectral peak intensities, CRLB, SNR, FWHM, location information, which were later used for metabolic map generation (Figure 4.2.i).

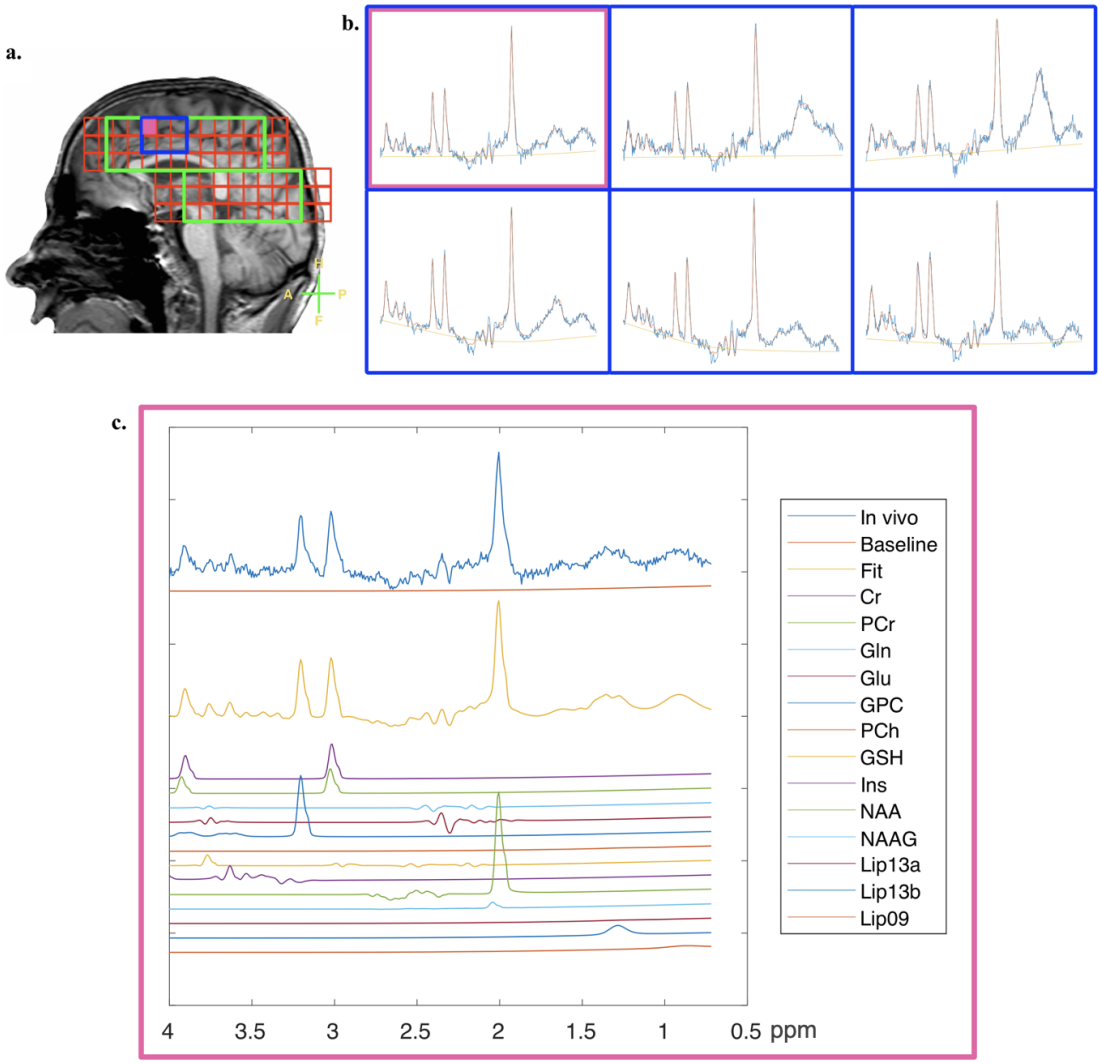


**Figure 4.1** The sagittal views of the $^{1}$H-MRSI FOVs (red) and PRESS selected boxes (green) (a), the spectra of a selected region (blue) (b), and a single spectrum example along with some of the LCModel quantification results (pink) (c) for a 66-years-old male PD-MCI patient [3].

Several inclusion criteria considering FWHM, SNR, CRLB, and CSF fraction thresholds were applied to produce a final inclusion matrix in the spectral PRESS box area for the automatic spectral quality check. First, only the spectra with FWHM $<$ 0.1 ppm [118] and SNR $>$8 were included in the analysis [119]. Next, any metabolite of a given spectrum with a CRLB of more than 30 was excluded [120]. Additionally, any voxel with a CSF fraction of more than 0.3 was excluded from the analysis [118].

The binary mask in Figure 4.2.j represents an example of the inclusion matrix for the tNAA concentrations at a given slice. One MRSI voxel represents a 10 x 10 x 12 mm area on the T2w MRI, which encompasses multiple voxels. Metabolic images, like a tNAA concentration image, were generated, and each voxel value of MRSI data was placed in a corresponding area in the 3D volumes in accordance with the T2w-MRI (Figure 4.2.k - left). All resultant metabolite images were 3D volumes and saved in NIFTI format with a size of 128 x 128 x 90 to match the T2w MRI. Additionally, corrected metabolic concentration images were generated by taking into account the partial volume effect (PVE) as, Ccorrected=$C_0$*(1/(1-VCSF)), where VCSF is the CSF volume fraction within the voxel of interest (Figure 4.2.k - right). Moreover, metabolite to total creatine or myoinositol ratio images were generated by applying pixel by pixel division in the 3D metabolite volumes. Figure 4.2.l shows the division of an example tNAA image (up left) with a tCr image (upper right) and the resultant tNAA/tCr ratio image (bottom) at their intersection area. Subsequently, the reference T2w MR image (Figure 4.2.m, up left) was registered into the MNI152 brain atlas (Figure 4.2.m, upper right) using FMRIB's Linear Image Registration Tool (FLIRT) [144] to obtain a transformation matrix, which was subsequently applied to register the overlaid metabolic images into the MNI152 brain atlas (Figure 4.2.m, down). This data analysis pipeline was repeated for the second $^1$H-MRSI scan. Then, a simple matrix addition was applied to the metabolite images belonging to the first and second MRSI scans to create combined metabolic images (Figure 4.2.n, up left). Finally, the metabolic intensities were evaluated at the intersection of the PRESS box with 400 brain parcellations defined on seven rs-fMRI networks [95] (Figure 4.2.n, upper right). An example region of interest is shown in Figure 4.2.n (down). Only the regions included in the PRESS box of at least nine participants of each subject group and 40

participants of all groups were included in the statistical analysis.

As a result, metabolic ratios, including tCho/tCr, tNAA/tCr, mI/tCr, Glx/tCr, and tNAA/mI, were evaluated at 69 different brain parcellations. Moreover, FSLeyes was used to match the rs-fMRI brain parcellations to the Harvard-Oxford cortical atlas to evaluate metabolite intensities at structural regions.

### 4.2.4 Statistical Analysis

The neuropsychological test scores, disease duration, levodopa drug dosage, Hoehn & Yahr, and MDS-UPDRS test scores were compared between PD-CN and PD-MCI groups using the Mann-Whitney U test. Age, education, and metabolite values were compared between the HC, PD-CN, and PD-MCI groups using a Kruskal-Wallis test followed by post-hoc Dunn's test for pairwise multiple comparisons. The gender distribution was compared between the three groups using a chi-square test. Additionally, a Spearman rank correlation coefficient test was used to assess the association between the MR spectroscopic values and neuropsychological test scores in all patients with PD. Bonferroni multiple comparison correction was applied, and p-values of $< 0.\ 00007$ (0.05/[69 regions * 5 metabolite ratios * 2 (original and corrected)]) were considered as statistically significant for the tests comparing the metabolic indices between subject groups in different brain parcellations [95]. On the other hand, the false-positive error was corrected by the total number of neuropsychological tests, and p-values of $< 0.007$ (0.05/7) were considered statistically significant when comparing the neuropsychological test scores between the subject groups. A p-value of $< 0.05$ was considered statistically significant for Dunnâs post-hoc test.

Finally, machine learning algorithms, including k-nearest neighbor (KNN), bagged trees, and fine Gaussian support vector machine (SVM), were employed in MATLAB Classification Learner for the classification of HC versus PD-CN or PD-MCI and PD-CN versus PD-MCI using tNAA/tCr, tNAA/mI, tCho/tCr, tCho/mI, Glx/tCr, Glx/mI, and mI/tCr at the brain parcellations. The class imbalance issue was addressed

using the Synthetic Minority Over-sampling Technique (SMOTE) approach. The accuracy, sensitivity, and specificity of the classification algorithms were evaluated using a five-fold cross-validation.

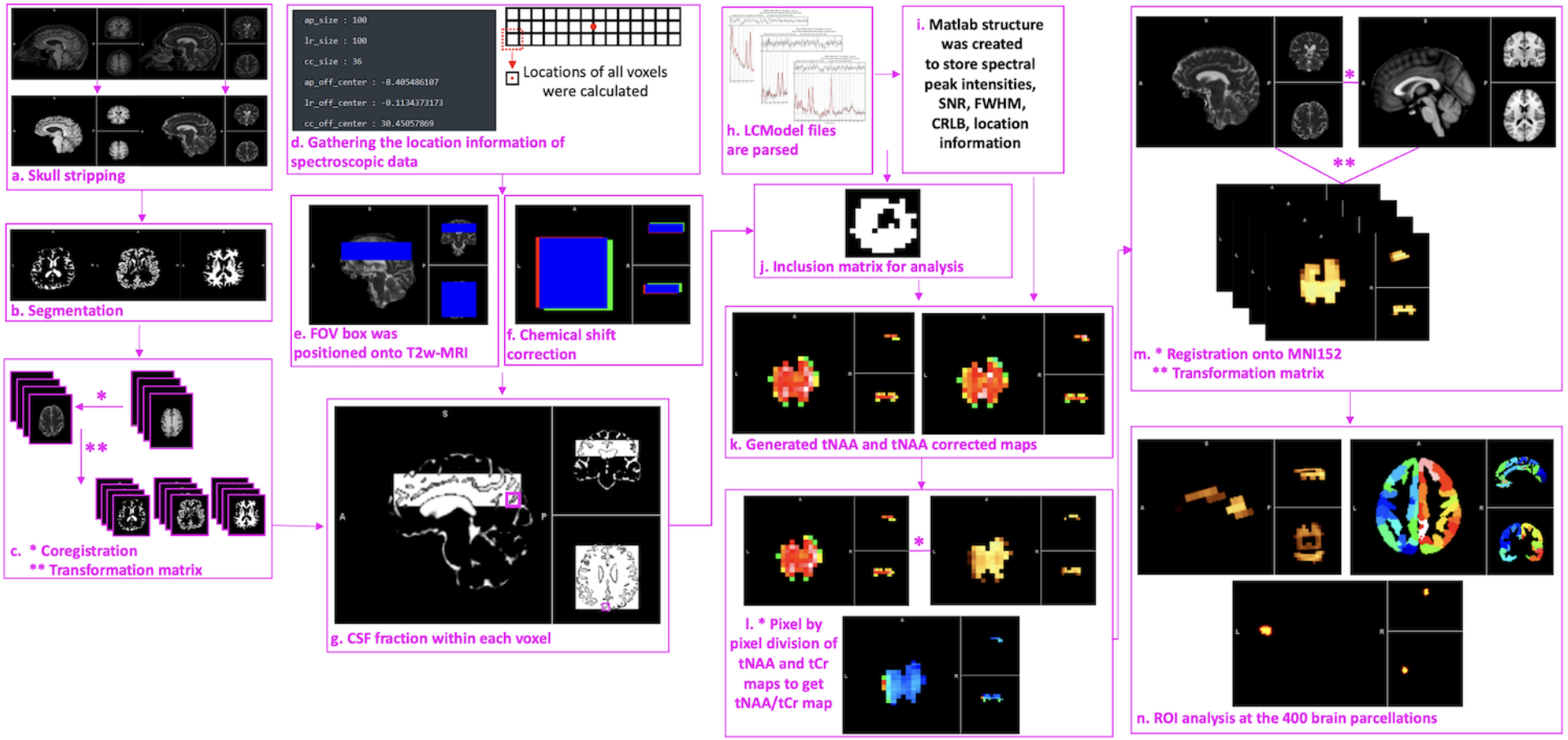


**Figure 4.2** A step by step visualization of the workflow for the 3D MRSI data analysis [3].

## 4.3 Results

Table 4.1 shows the demographic details of the participants in this study. The ratios of male to female patients were 11:5, 16:10, and 24:10 in the HC, PD-CN, and PD-MCI groups, respectively. Although the PD-MCI and HC groups had fewer females than males, the gender distribution was not statistically significantly different between the three groups ($p = 0.75$). The mean age of subjects was around 60 years, and it was not significantly different between the three groups ($p = 0.16$). Although the mean years of education were slightly lower in the PD-MCI group ($8.35 \pm 3.63$ years), this difference was not statistically significant between the subject groups ($p = 0.08$). Additionally, PD-CN and PD-MCI patients had similar Hoehn Yahr scores ($p = 0.40$), disease duration ($p = 0.21$), and levodopa dosages ($p = 0.21$). On the other hand, PD-MCI patients had lower total MDS-UPDRS ($p = 0.05$) and MDS-UPDRS-III ($p = 0.04$) scores than PD-CN patients.

There were statistically significant differences between the ACE-R ($p < 0.0001$), ACE-R visual ($p = 0.0001$), MMSE ($p < 0.0001$), MOCA ($p = 0.0003$), and SDMT ($p = 0.0002$) test scores of the three subject groups (Table 4.2). While the neuropsychological test scores were similar between HC and PD-CN groups in pairwise comparisons, PD-MCI patients had lower ACE-R ($p < 0.0001$ for both HC and PD-CN), ACE-R visual ($p = 0.002$ for HC, and $p = 0.0009$ for PD-CN), MMSE ($p = 0.0013$ for HC, and $p = 0.01$ for PD-CN), MOCA ($p = 0.001$ for HC, and $p = 0.002$ for PD-CN), and SDMT ($p = 0.0015$ for HC, and $p = 0.002$ for PD-CN) than both HC and PD-CN patients. There were no statistically significant differences between the WCST percentage of perseverative response scores, STROOP interference time, and JLO scores of the three subject groups. No statistically significant differences were observed between the GM, WM, and CSF fractions of the subject groups in this study.

PD-CN patients had higher tGlu/tCr ratio ($p = 0.003$) and corrected tGlu/tCr ratio ($p = 0.003$) than HC at a part of ventral attention / salience networks (VAN/SN), corresponding to the left dorsal anterior cingulate cortex (dACC) (Figure 4.3, red region) (Table 4.3). Additionally, PD-CN patients had a higher mI/tCr ratio ($p =$

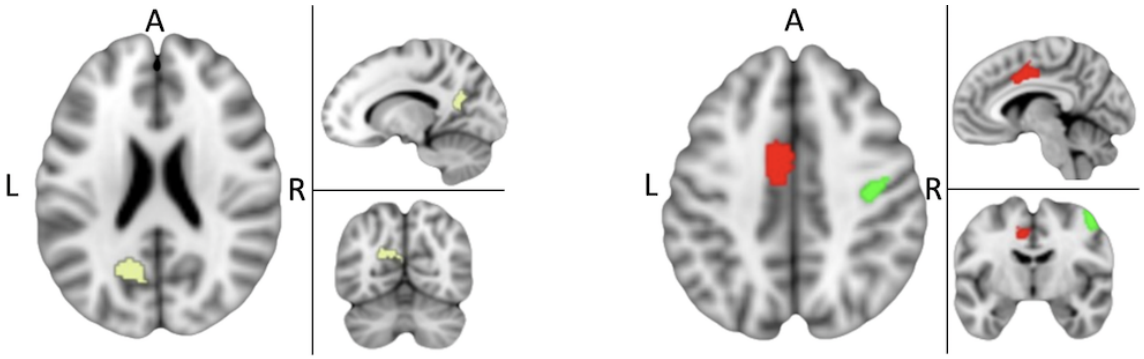


**Figure 4.3** The superior brain regions with metabolic differences between the three subject groups. Red: the left dACC, corresponding to VAN/SN, green: the right precentral gyrus, corresponding to SMN, gold: left precuneus PCC, corresponding to DMN [3].

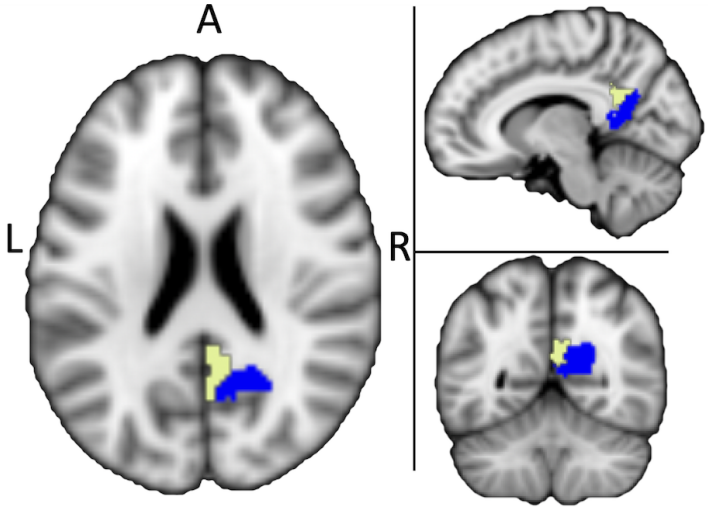


**Figure 4.4** Additional inferior brain regions with metabolic differences between the three subject groups. Blue: the right retrosplenial cortex, corresponding to DMN, gold: the right precuneus PCC, corresponding to DMN [3].

0.01) and corrected mI/tCr ratio (p = 0.02) than HC at a part of default mode network (DMN), corresponding to the left precuneus, occupying a part of the posterior cingulate cortex (PCC) (Figure 4.3, gold region). PD-MCI patients had lower tNAA/tCr ratio (p = 0.002) and corrected tNAA/tCr ratio (p = 0.01) in the right precentral gyrus, corresponding to sensorimotor network (SMN) (Figure 4.3, green region) than PD-CN. Finally, there were tNAA/mI ratio and corrected tNAA/mI ratio differences between the three subject groups in the right retrosplenial cortex, corresponding to the DMN (Figure 4.4, blue region). Post-hoc comparisons indicated that PD-MCI patients had lower tNAA/mI (p = 0.04) than PD-CN in this area. Moreover, there was a positive correlation between tNAA/tCr and JLO in the right precuneus, involving the PCC, a part of DMN (Figure 4.4, gold region) (r = 0.49, p = 0.0004).

**Table 4.1**
The demographic details of the participants in this study.

| | **HC** | **PD-CN** | **PD-MCI** | **p** |
|---|---|---|---|---|
| Sex (M:F) | 11:05 | 16:10 | 24:10 | 0.75 |
| Age | 59.38±6.71 | 60.85±9.42 | 63.00±9.34 | 0.16 |
| Education Years | 10.19±3.83 | 10.42±4.01 | 8.35±3.63 | 0.08 |
| Hoehn & Yahr | N/A | 1.78±0.51 | 1.90±0.53 | 0.40 |
| Disease duration, years | N/A | 5.6±2.97 | 6.80±3.62 | 0.21 |
| Levodopa dosage, mg/day | N/A | 692.27±354.53 | 818.00±393.18 | 0.21 |
| MDS-UPDRS-III | N/A | 24.38±10.60 | 30.76±12.96 | 0.09 |
| MDS-UPDRS-Total | N/A | 45.11±17.18 | 52.50±21.57 | 0.13 |

**Table 4.2**
The comparison of the neuropsychological test scores of the three subject groups.

| **Test** | **Subjects** | **Mean±SD** | **p** | **PD-CN, p** | **PD-MCI, p** |
|---|---|---|---|---|---|
| WCST % of PR | HC | 18.52 ± 7.64 | 0.04 | 0.99 | 0.16 |
| | PD-CN | 18.51 ± 9.02 | | | 0.06 |
| | PD-MCI | 24.39 ± 9.84 | | | |
| ACE-R | HC | 92.69 ± 4.32 | <0.0001** | 0.55 | <0.0001* |
| | PD-CN | 89.81 ± 3.82 | | | <0.0001* |
| | PD-MCI | 76.82 ± 5.74 | | | |
| ACE-R (Visual) | HC | 15.62 ± 0.50 | 0.0001** | 0.99 | 0.002* |
| | PD-CN | 15.48 ± 0.82 | | | 0.0009* |
| | PD-MCI | 14.17 ± 1.46 | | | |
| MMSE | HC | 29.88 ± 0.50 | <0.0001** | 0.13 | 0.0013* |
| | PD-CN | 29.31 ± 0.84 | | | 0.01* |
| | PD-MCI | 28.15 ± 1.58 | | | |
| MOCA | HC | 25.79 Â±2.42 | 0.0003** | 0.93 | 0.001* |
| | PD-CN | 25.10 ± 2.38 | | | 0.002 |
| | PD-MCI | 22.39 ± 2.48 | | | |
| STROOP IT | HC | 46.50 ± 17.17 | 0.02 | 0.65 | 0.03 |
| | PD-CN | 53.77 ± 18.97 | | | 0.22 |
| | PD-MCI | 74.15 ± 42.81 | | | |
| JLO | HC | 24.81 ± 2.76 | 0.08 | 0.89 | 0.11 |
| | PD-CN | 23.69 ± 3.87 | | | 0.28 |
| | PD-MCI | 21.53 ± 5.23 | | | |
| SDMT | HC | 35.69 ± 14.48 | 0.0002** | 0.91 | 0.0015* |
| | PD-CN | 31.00 ± 9.15 | | | 0.002* |
| | PD-MCI | 21.50 ± 9.61 | | | |

**p <0.007: statistically significant for the Kruskal-Wallis test; and *p<0.05: Dunn's post-hoc test. PR: perseverative responses, IT: interference time.

**Table 4.3**
The differences of the original and corrected spectroscopic concentrations and the ratio values between the three subject groups.

| Metabolite | Metric | Network - PL | Core Regions | Subjects | Mean ± SD | p | PD-CN, p | PD-MCI, p |
|---|---|---|---|---|---|---|---|---|
| tGlutCr | Ratio | VAN SN - 108 | Left dACC | HC | 1.12 ± 0.31 | 0.004 | 0.003* | 0.14 |
| | | | | PD-CN | 1.25 ± 0.16 | | | 0.39 |
| | | | | PD-MCI | 1.39 ± 0.39 | | | |
| | Corrected Ratio | | | HC | 1.12 ± 0.30 | 0.005 | 0.003* | 0.14 |
| | | | | PD-CN | 1.26 ± 0.17 | | | 0.41 |
| | | | | PD-MCI | 1.39 ± 0.38 | | | |
| mItCr | Ratio | DMN - 191 | Left precuneus & PCC | HC | 0.95 ± 0.13 | 0.009 | 0.01* | 0.63 |
| | | | | PD-CN | 1.01 ± 0.21 | | | 0.11 |
| | | | | PD-MCI | 1.12 ± 0.24 | | | |
| | Corrected Ratio | | | HC | 0.96 ± 0.13 | 0.02 | 0.02* | 0.75 |
| | | | | PD-CN | 1.02 ± 0.20 | | | 0.12 |
| | | | | PD-MCI | 1.12 ± 0.25 | | | |
| tNAAtCr | Ratio | SMN - 252 | Right precentral gyrus | HC | 1.32 ± 0.25 | 0.004 | 0.41 | 0.38 |
| | | | | PD-CN | 1.44 ± 0.24 | | | 0.002* |
| | | | | PD-MCI | 1.16 ± 0.15 | | | |
| | Corrected Ratio | | | HC | 1.31 ± 0.22 | 0.02 | 0.56 | 0.49 |
| | | | | PD-CN | 1.40 ± 0.25 | | | 0.01* |
| | | | | PD-MCI | 1.16 ± 0.17 | | | |
| tNAAmI | Ratio | DMN - 392 | Right retrosplenial cortex | HC | 1.52 ± 0.36 | 0.02 | 0.06 | 0.99 |
| | | | | PD-CN | 1.47 ± 0.31 | | | 0.04* |
| | | | | PD-MCI | 1.22 ± 0.23 | | | |
| | Corrected Ratio | | | HC | 1.51 ± 0.36 | 0.04 | 0.1 | 0.99 |
| | | | | PD-CN | 1.47 ± 0.30 | | | 0.08 |
| | | | | PD-MCI | 1.23 ± 0.25 | | | |

**Table 4.4**
The classification accuracy/sensitivity/specificity of HC vs. PD-CN, HC vs. PD-MCI, and PD-CN vs. PD-MCI using spectroscopic features.

| Subjects | Model | Accuracy | Sensitivity | Specificity |
|---|---|---|---|---|
| HC vs PD-CN | Bagged Trees | 86.5 | 73.1 | 84.6 |
| HC vs PD-MCI | Bagged Trees | 86.4 | 72.7 | 81.8 |
| PD-CN vs PD-MCI | Fine Gaussian SVM | 77.3 | 63.6 | 69.7 |

The classification algorithms resulted in an overall accuracy of 86.5 % (sensitivity = 73.1 % and specificity = 84.6 %) for classifying HC and PD-CN groups based on metabolic intensities using bagged trees (Table 4.4). On the other hand, HC and PD-MCI groups were successfully classified using bagged trees with an accuracy of 86.4 % (sensitivity = 72.7 % and specificity = 81.8 %). Finally, the classification accuracy of PD-CN versus PD-MCI was 77.3 % (sensitivity= 63.6 % and specificity = 69.7 %) using a fine gaussian SVM.

## 4.4 Discussion

This study investigated differences in metabolite levels between HC, PD-CN, and PD-MCI at various functional connectivity network parcellations and explored the associations between the metabolic markers and neuropsychological test scores. Our 3D $^{1}$H-MRSI data acquisition region covered a large portion of the cerebrum without the need for precise manual region selection. We generated 3D metabolite images after taking into account CSF partial volume effects and several quality control checks and registered them into the MNI152 brain atlas to enable consistent ROI analysis in multiple subjects. Moreover, this atlas-based registration and analysis approach enabled us to evaluate various metabolites at several brain parcellations defined on the MNI152 atlas. This study suggested that multi-voxel $^{1}$H-MRSI could be employed to reveal changes in brain metabolism in PD-MCI, especially in the regions that are parts of DMN, VAN/SN, and SMN. We can summarize our findings mainly as 'posterior metabolic changes' in PD patients, compared to HC subjects. In studies using ASL-MRI, a 'posterior cortical hypoperfusion' pattern was established as indicative of cognitive impairment in PD [145], [146], [98]. Therefore, 'posterior cortical' changes at post-Rolandic structures in cognitive impairment might be a multimodal imaging finding.

Previous studies have identified several possible metabolic biomarkers of cognitive decline in PD at a few brain areas [13], [14], [15], [16], [17], [147]. Guan et al. [147] reported significantly lower NAA/Cr ratios in the cortical areas, such as prefrontal cor-

tex, cuneus, hippocampus, as well as subcortical structures, such as substantia nigra, globus pallidus, and dorsal thalamus in PD patients than in HCs using single-voxel $^{1}$H-MRS. Another study reported lower NAA/Cr ratios in the occipital lobe and higher Cho/Cr ratios at the PCC in PD-MCI patients than in HC [13]. Similarly, Summerfield et al. [16] reported reduced NAA levels in the occipital lobes of PDD patients. Moreover, Camicioli et al. [14] reported lower NAA/Cr ratios in the PCC of non-demented PD patients than in HC. On the other hand, although lower NAA/Cr and higher Cho/Cr ratios were observed in the PCC of PDD patients than that of HCs in another study, these differences were not statistically significant after correcting for age, sex, and MDS-UPDRS III scores [148]. Another study assessed metabolic differences in PDD, PD-MCI, and PD-CN and reported a significant reduction in NAA levels in the right dorsolateral prefrontal cortex in PD-MCI and in the left hippocampus in PDD [17].

Several MRI studies have reported possible imaging biomarkers of cognitive impairment in ICNs, including VAN, DMN, VN, and SMN. Although Yeo et al. [137] reported that VAN region was likely an aggregate of multiple networks variably referred to as the SN [149] and cingulo-opercular networks (CON) [150], dissimilar functions had been assigned to these networks. VAN responds to sudden salient stimuli [151], whereas SN selects the stimuli that deserve attention [152]. On the other hand, CON takes a role in error-processing and inhibitory control [153]. A study reported that PD patients with impulse control deficits had decreased perfusion and reduced brain activity at regions including the prefrontal-striatal loops and ACC, which was interpreted as a response inhibition impairment, a function that is implicated for CON [154]. Our findings indicated a higher tGlu/tCr ratio in the left dACC of the VAN/SN/CON, which might result in glutamate toxicity possibly leading to deficiencies in proper response to stimuli and inhibitory control. DMN, comprising the precuneus, PCC, medial frontal cortex, and bilateral temporoparietal junction, involves internal modes of cognition and is linked to attention, working memory, and memory recall [155]. The failure of DMN to deactivate at the appropriate moments is linked to poor attention performance [156]. Proper deactivation of DMN could be associated with better task performance, which might manifest itself as higher tNAA [157], which is a marker

of neuronal viability, and lower mI [158], an indicator of less gliosis or inflammation. Additionally, another study reported higher mI as a classic hallmark of Alzheimer's disease MCI (AD-MCI), focusing mainly on the pathophysiology [159]. Similarly, our findings indicated that PD-CN patients had higher mI/tCr than HC, while PD-MCI patients had decreased tNAA/mI at a part of the DMN. The alterations in mI/tCr and tNAA/mI levels might suggest neuronal loss and gliosis, resulting in a parallel decline in DMN connectivity. On the other hand, SMN is a large-scale brain network that comprises primary somatosensory (postcentral gyrus), primary motor (precentral gyrus) cortices, and supplementary motor area (SMA). When executing and coordinating motor activities, such as finger tapping, the SMN is engaged, suggesting that the network prepares the brain for motor activity. rs-fMRI studies reported lower functional connectivity at the SMN of PD-MCI patients [160], [161]. We have previously reported that PD-MCI had decreased perfusion in the left precentral gyrus at the SMN than HC using ASL-MRI [98]. Our results are consistent with the previous findings and revealed lower tNAA/tCr in PD-MCI than PD-CN at a part of the SMN corresponding to the right precentral gyrus, which might suggest neuronal loss at this area. In addition, our results revealed a positive correlation between tNAA/tCr and JLO in the right precuneus and PCC of DMN, which might indicate a relationship between metabolic abnormalities and visuospatial deficits detectable by JLO in PD-MCI.

There is no single machine learning algorithm that would work best for every classification problem [162]. As a result, the performances of numerous machine learning algorithms were evaluated in this work. PD-MCI and PD-CN were successfully differentiated from HC based on the spectroscopic differences within the DMN, SMN, and VAN/SN/CON regions using machine learning algorithms. On the other hand, the classification of PD-MCI and PD-CN had a lower accuracy, possibly due to their more similar metabolic signatures altered by Parkinson's disease.

The current study had some limitations. The $^{1}$H-MRSI data acquisition volume of interest was manually selected for each subject, which necessitated post-processing registration. Also, the full brain coverage was not possible due to the limitations of the clinical MRSI data acquisition sequence used in this study. As a result, the brain

regions outside of the spectral FOV coverage could not be assessed and the reported metabolic results are restricted to the available brain parcellations within the spectral FOV. Moreover, registration of $^{1}$H-MRSI data of our subject population, with a mean age of 60 years, into the MNI152, a normalized brain atlas based on healthy and young subjects, might have resulted in slight regional shifts between subjects. So, future studies will use age-matched brain atlases for more accurate registration [163]. Additionally, an automated single MRS voxel placement based on the MNI brain atlas during data acquisition has been recently proposed [164], which might be adapted to 3D $^{1}$H-MRSI to improve the prescription consistency between the subjects. Bonferroni multiple comparison correction was applied in this study considering original and corrected metabolite ratios and brain regions. Therefore, p-values of $< 0.\ 00007$ were considered as statistically significant, which was quite strict. Although our approach was rather rigorous to prevent false positives, it might have reduced the power of the tests to detect some true statistically significant differences. Moreover, we employed PRESS to acquire the $^{1}$H-MRSI data, which is known to suffer from the chemical shift artifact more than the semi-LASER sequence that minimizes chemical shift displacement errors. On the other hand, this work included the calculation and correction of the chemical shift error using the Oryx-MRSI software tool. Additionally, we did not have unsuppressed water or metabolite relaxation times available for all our datasets for absolute metabolite quantification. Our study had a limited number of subjects and future studies with larger sample sizes and longer follow-up durations are required to validate the biomarkers of PD-MCI. Additionally, a future study including PD-dementia patients might help to clarify the metabolite changes along the cognitive impairment stages. An integrated analysis of $^{1}$H-MRSI data with other multimodality MR images after registration into a common brain template would increase our understanding of the mechanisms of cognitive impairment in PD.

In conclusion, this study has shown that multivoxel $^{1}$H-MRSI provides objective metabolic findings of mild cognitive impairment in PD. Specifically, PD-MCI patients had lower tNAA/tCr and tNAA/mI levels at the posterior cortical regions, affecting mainly the functions of DMN and SMN.

# 5. SUPER-RESOLUTION FOR MRSI

## 5.1 Rationale

$^{1}$H-MRSI in addition to standard anotomical MR images, like T1w MRI, T2w MRI, and FLAIR MRI, helps in better defining disease characteristics by providing metabolic information of the tissue. $^{1}$H-MRSI detects a number of metabolites present in the tissue in relatively much lower concentrations than water. As a result, higher voxel sizes are employed for $^{1}$H-MRSI to increase SNR. $^{1}$H-MRS images typically have a spatial resolution that is 10 times lower than anatomical MR images. It is possible to increase the spatial resolution of $^{1}$H-MRSI, but it would require a long scan time unless data under-sampling strategies are employed [165]. An alternative approach that would result in higher spatial resolution $^{1}$H-MRSI without a cost of scan time is advanced post-processing methods. In this study, we propose to increase the spatial resolution of $^{1}$H-MRSI using Super-Resolution Convolution Neural Network (SRCNN). For this purpose, we present an SRCNN pipeline for post-processing $^{1}$H-MRSI images using the anatomical information present in T1w, T2w and FLAIR MRI. Additionally, one of the recent super resolution for single image methods, enhanced deep super-resolution network (EDSR), has been applied to create super resolved anatomical and metabolic images. Some of the contents of this chapter have been published at the Communications in Computer and Information Science book series [4].

## 5.2 Materials and Methods

### 5.2.1 MR Data Acquisition and Preprocessing for SRCNN

Three healthy subjects (age=$51.33 \pm 5.03$ years; 1F/2M), who provided written informed consent before the data acquisition, were included in this study. The imaging experiments were performed on a 3T clinical MR scanner (Philips Medical Systems,

Best, Holland) with a 32-channel head coil. For each subject, MRI data acquisition frames were aligned parallel to the anterior commissure - posterior commissure line. For anatomical scans, a T1w MRI (TR/TE=8.3/3.8 ms, FOV=250 x 250 x 180 mm, voxel size=1 x 1 x 1 mm), T2w MRI (TR/TE=10243/80 ms, 90 flip angle, FOV= 240 x 240 x 180 mm, voxel size=2 x 2 x 2 mm), and FLAIR MRI (TR/TE=4800/1650 ms, FOV= 250 x 250 x 180 mm, voxel size=1 x 1 x 3 mm) were obtained. Afterwards, three dimensional $^{1}$H-MRSI data was acquired by using PRESS sequence (TR/TE=1000/52 ms, FOV=140 x 140 x 36 mm, voxel size= 10 x 10 x 12 mm, 14 x 14 x 3 voxels, scan time=8 min). T2w MRI was used as the reference image for defining $^{1}$H-MRSI ROI, which covered a 110 x 110 x 36 mm region.

Raw $^{1}$H-MRSI data were exported out and the spectra were quantified by using the LCModel program [75]. Metabolite concentrations including tNAA were quantified for each voxel. Oryx-MRSI was used to combine the metabolite concentrations of each voxel into a single tNAA map for each slice. T1w and FLAIR MRI were rigidly registered to reference T2w MRI using FSL-FLIRT to align all anatomical scans (Figure 5.1). Additionally, a fused MRI was formed by placing T1w, T2w, and FLAIR MRI into three distinct channels of an RGB image using the https://sourceforge.net/projects/bric1936/MCMxxxVI-RGBExplorer tool.

The spatial resolution of tNAA maps were upscaled by a factor of five along the in-plane dimensions using nearest neighbor interpolation to match the T2w MR image resolution. T1w, T2w, FLAIR, and Fused MR image regions that corresponded to the region of interest of tNAA maps were extracted (Figure 5.2). Each spectral slice was 12 mm thick, and it contained six 2 mm thick anatomical MR images. Our $^{1}$H-MRSI data was composed of three slices. As a result, we obtained 18 images for each anatomical MR imaging modality for each subject, resulting in a total of 54 slices for all of the three subjects.

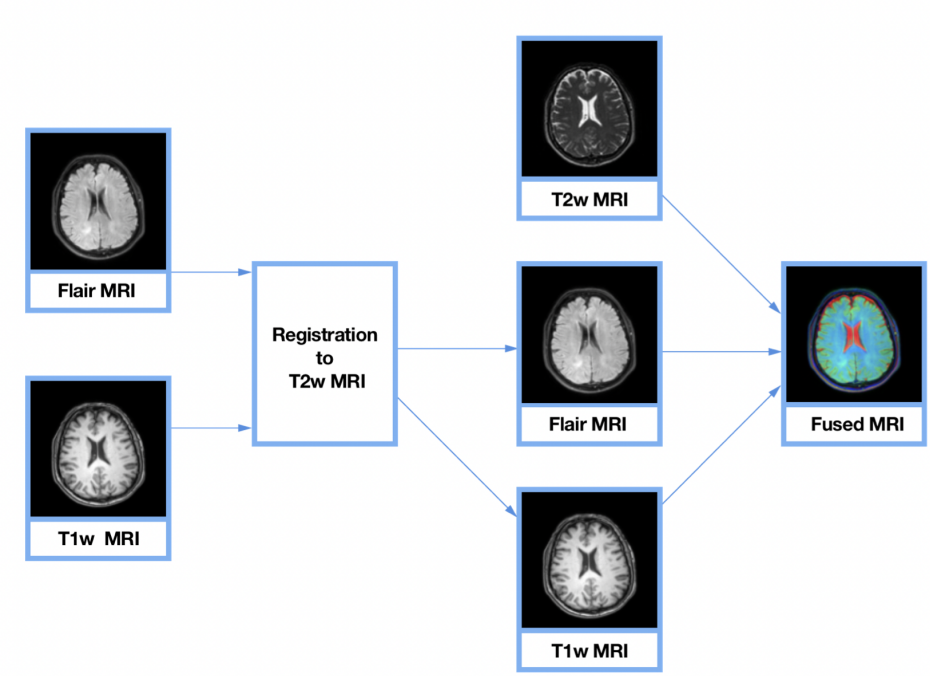


**Figure 5.1** A schematic of MR image registration and fusion of T1w, T2w, and FLAIR MRI [4].

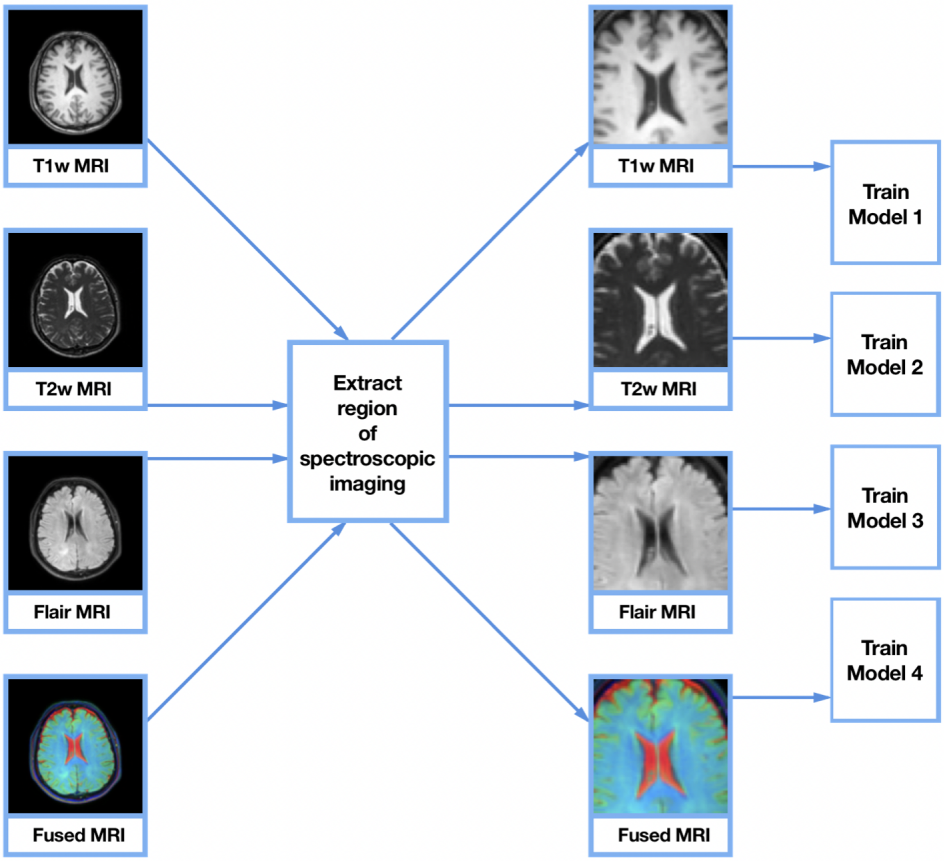


**Figure 5.2** A schematic pipeline of ROI extraction and training of anatomical MRI [4].

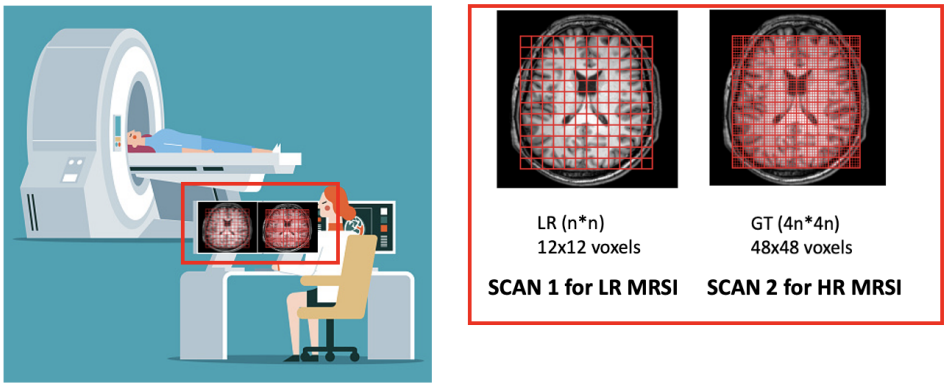


**Figure 5.3** High and low resolution data acquisition of MRSI.

### 5.2.2 MR Data Acquisition and Preprocessing for EDSR

MR spectroscopic imaging data were acquired from 10 volunteers and GE Braino phantom at 3T and 7T clinical MR scanners for the super-resolution of MRSI study. During the covid pandemic and due to the busy schedule of the hospitals, the data acquisition was started on March 21, 2021, and the last data acquisition was completed on March 5, 2022. Some MRSI scans were not usable due to the poor data quality, high noise and low metabolite concentration definition, and as a result, only four MRSI datasets could be analyzed. An example high and low MRSI data acquisition matrix is shown in Figure 5.3.

### 5.2.3 CNN Implementation

Caffe [166] was installed as a deep learning framework for SRCNN to train super-resolution models. SRCNN structure shown in Figure 5.4 included three convolutional layers, which performed patch extraction and representation, non-linear mapping and reconstruction [5]. At the first layer, the image was convolved with a set of filters followed by an application of Rectified Linear Unit (ReLU, max(0, x)) on filter responses [167]. For the first layer, a kernel size of 3 x 9 x 9 was used for each convolution, and 64 feature maps were produced as the output. The second layer mapped the 64-dimensional features of each patch onto a 32-dimensional feature space of the

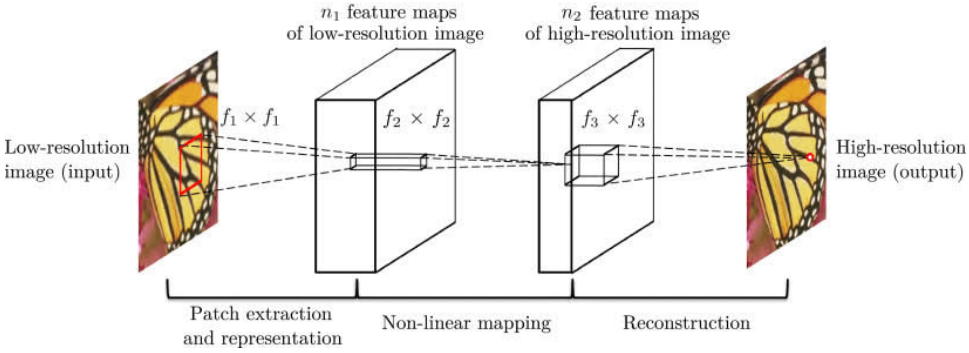


**Figure 5.4** SRCNN network structure [5].

high resolution image. The final layer served the purpose of combining the overlapping high-resolution patches to produce the final high resolution image. The kernel sizes of the second and the third layers were 1 x 1 and 5 x 5, respectively. The weight filler type was set as Gaussian, base learning rate was set as 0.0001, and the learning policy was fixed. A Euclidean loss function was employed. As per the training/testing strategy from [168], the extracted regions of the structural MR images and Fused MRI were downsampled and fed into the SRCNN to train four separate models (Figure 5.2). Thirty-nine MR images were used for training the SRCNN framework, and fifteen MR images were used for testing purposes for each model. Afterwards, tNAA maps were used as the testing dataset, and the four distinct models trained on different structural MR images or Fused MRI were employed in SRCNN to upscale the spatial resolution of tNAA maps by a factor of three. SRCNN was run three times with 10,000, 100,000, or 1,000,000 iterations for each model to determine the number of necessary iterations for reconstructing a high quality super resolution tNAA map. The results of the SRCNN were compared with bicubic interpolation.

### 5.2.4 EDSR Implementation

EDSR [6] structure used in this study is shown in Figure 5.5. It consists of SRResNet and modified residual blocks and uses scaling layers to ensure consistency. Unlike SRResNet, it eliminates useless modules to make the network architecture simpler. Additionally, batch normalization was skipped, which helped to save almost 40 % memory usage. In this study, EDSR technique [6] was adopted us-

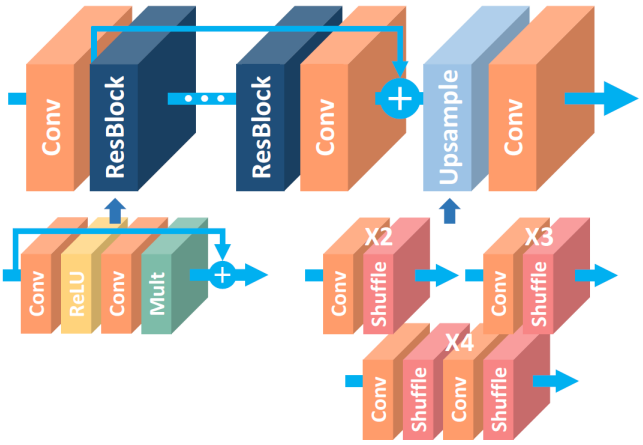


**Figure 5.5** EDSR network structure [6].

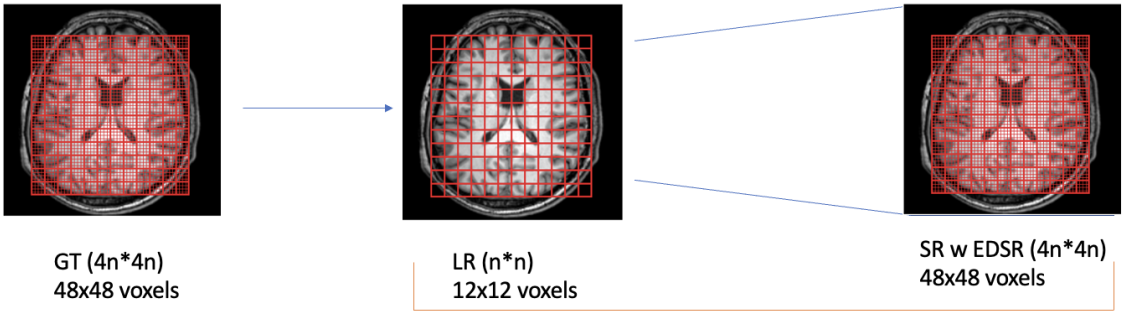


**Figure 5.6** The pipeline for the low and high resolution MRSI data to get super resolved MRSI.

ing Keras API. EDSR Pre-trained model was downloaded for transfer learning (Link: https://github.com/krasserm/super-resolution). Then, the weights of the first few layers of the network were freezed, and for hyper parameter fine-tuning, different optimizers, loss functions, and learning rates were used to apply it for super resolved MRI. The final optimized parameters for learning rate, optimizer, loss function, and metric were set as 0.1, Adam, SSIM, and mean absolute error. The pipeline for the low and high resolution MRSI data to get super resolved MRSI data is shown in Figure 5.6.

### 5.2.5 Image Quality Evaluation Metrics

Peak signal to noise ratio (PSNR), and root mean square error (RMSE) were used as evaluation metrics of accuracy on all experiments in our study. The tNAA

**Table 5.1**
The mean PSNR and RMSE of anatomical MRI and Fused MRI datasets.

| | | **T1w MRI** | | **T2w MRI** | | **FLAIR MRI** | | **Fused MRI** | |
|---|---|---|---|---|---|---|---|---|---|
| **Method** | **# Iteration** | **PSNR** | **RMSE** | **PSNR** | **RMSE** | **PSNR** | **RMSE** | **PSNR** | **RMSE** |
| Bicubic SR | - | 25.11 | 14.14 | 25.11 | 14.14 | 27.23 | 11.09 | 31.56 | 6.73 |
| SRCNN | 10000 | 25.21 | 13.98 | 24.81 | 14.64 | 27.52 | 10.71 | 30.67 | 7.46 |
| SRCNN | 100000 | 25.86 | 12.98 | 25.92 | 12.89 | 28.13 | 9.99 | 32.11 | 6.32 |
| SRCNN | 1000000 | 25.85 | 13 | 26.1 | 12.63 | 27.77 | 10.42 | 32.36 | 6.2 |

map that was upsampled by nearest neighbor interpolation was used as the reference image for comparison purposes.

## 5.3 Results of SRCNN

SRCNN was first applied to increase the spatial resolution of anatomical and fused MRI by using the corresponding MRI for both training and test datasets. Figure 5.7 displays our SRCNN results for increasing the spatial resolution of anatomical MRI. SRCNN resulted in less blurry and more detailed MRI than bicubic interpolation for all anatomical and Fused MRI. Gyri and sulci were better resolved in high resolution images obtained by SRCNN for all anatomical MRI. SRCNN resulted in a higher mean PSNR than bicubic interpolation for all anatomical and fused MRI after 10,000 iterations (Table 5.1). When T2w or Fused MRI were used as SRCNN training datasets, 10,000 iterations was not sufficient to outperform bicubic interpolation in terms of RMSE. Highest mean PSNR and lowest RMSE values were obtained when SRCNN was trained with 100,000 iterations for T1w and FLAIR MRI, and 1,000,000 iterations for T2w and Fused MRI.

Four distinct training models obtained by using SRCNN algorithm on different anatomical or Fused MRI were applied to increase the spatial resolution of tNAA maps. Table 5.2 displays the PSNR and RMSE values when bicubic interpolation or SRCNN with varying number of iterations were employed for super-resolution $^{1}$H-MRSI. T1w MRI model did not result in a higher PSNR or lower RMSE than bicubic interpolation

**Table 5.2**
The mean PSNR and RMSE results of SRCNN for super-resolution MRSI based on different anatomical MRI training models.

| | | T1w MRI | | T2w MRI | | FLAIR MRI | | Fused MRI | |
|---|---|---|---|---|---|---|---|---|---|
| **Method** | **# Iteration** | **PSNR** | **RMSE** | **PSNR** | **RMSE** | **PSNR** | **RMSE** | **PSNR** | **RMSE** |
| Bicubic SR | - | 27.01 | 11.37 | 27.01 | 11.37 | 27.01 | 11.37 | 27.01 | 11.37 |
| SRCNN | 10000 | 26 | 12.77 | 23.47 | 17.09 | 27.05 | 11.32 | 24.01 | 16.06 |
| SRCNN | 100000 | 26.69 | 11.79 | 27.88 | 10.28 | 27.58 | 10.64 | 27.77 | 10.41 |
| SRCNN | 1000000 | 25.94 | 12.86 | 26.08 | 12.65 | 26.29 | 12.35 | 28.17 | 9.95 |

for any of the iteration levels. Fused MRI model with 1,000,000 iterations resulted in the highest PSNR and lowest RMSE. Figure 5.8 shows our SRCNN results for increasing tNAA map spatial resolution.

## 5.4 Results of EDSR

Firstly, pre-trained model was applied to the MR images without further training (Figure 5.9). The PSNR value was calculated as 24.085. Secondly, transfer learning was applied by freezing top layers of the EDSR model. Figure 5.10 shows the ground truth (Gold) image, low resolution image (LR MRI), and super resolved image (SR MRI) obtained with the pretrained model, and SR MRI obtained with transfer learning. The PSNR value of transfer learning was calculated as 24.177, which was higher than SR MRI obtained with only pretrained model.

Thirdly, transfer learning was applied again with fine tuning (Figure 5.11). Learning rate was set to 0.01 and loss function was changed from mean absolute error (MAE) to mean square error (MSE). The PSNR result of SR MRI obtained with transfer learning and fine tuning (24.197) was higher than that of SR MRI with pretrained model (24.085), and SR MRI with only transfer learning by freezing the top layers (24.177).

Figure 5.12 shows the NAA metabolite maps produced from the acquired low and high resolution MRSI data. Low resolution images were upscaled by using bicubic

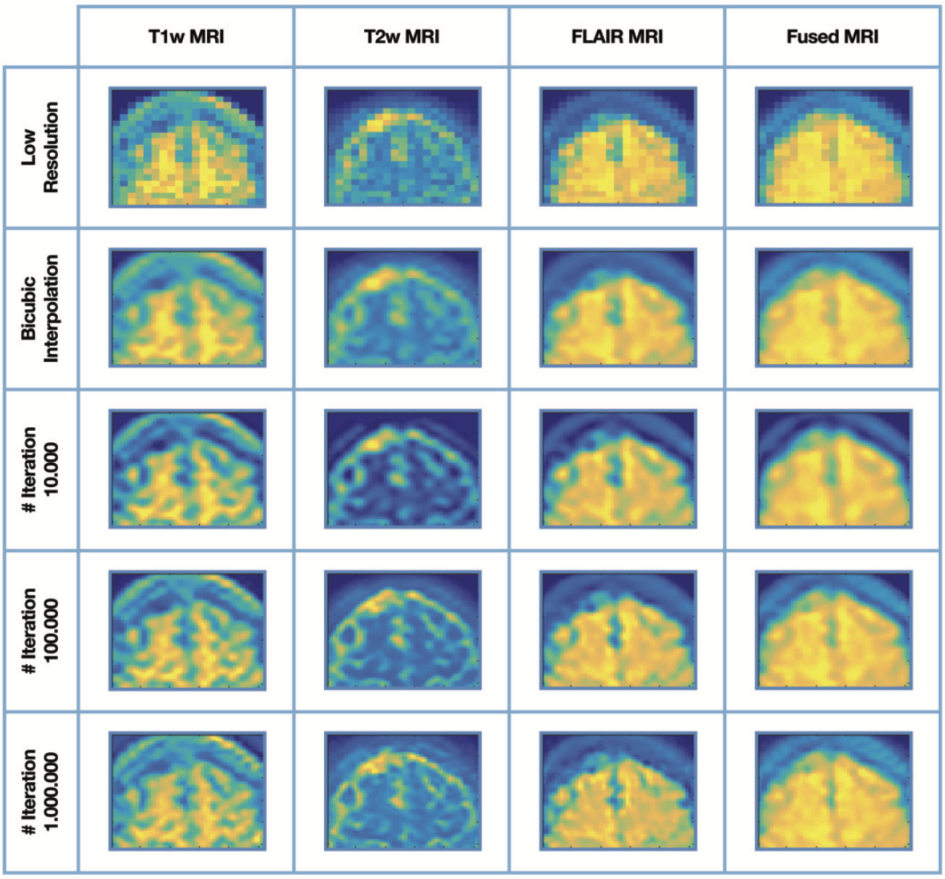


**Figure 5.7** Example SRCNN results for increasing the spatial resolution of anatomical MRI using 10,000, 100,000, and 1,000,000 iterations [4].

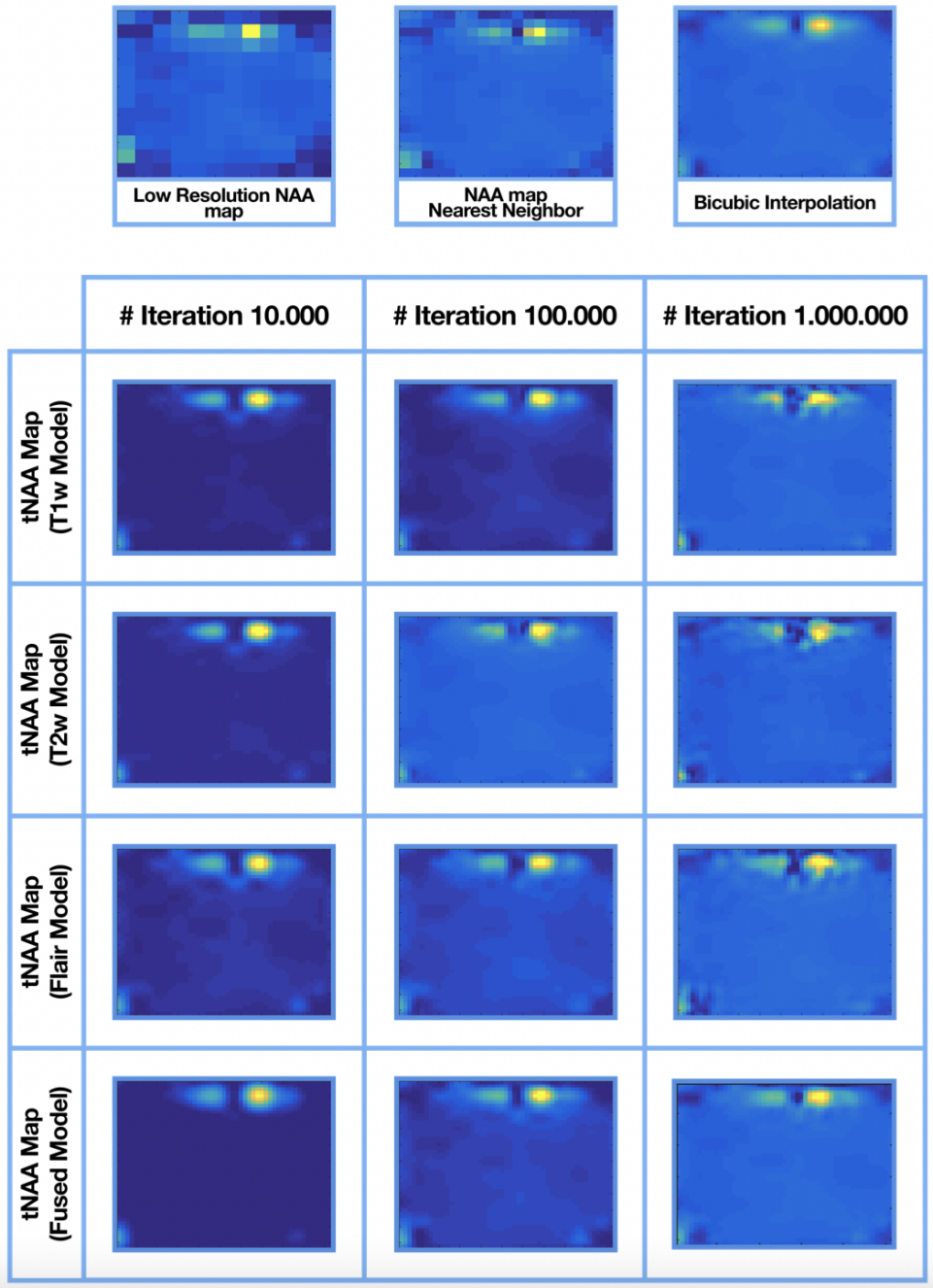


**Figure 5.8** SRCNN results of an example tNAA map upscaled by using T1w, T2w, FLAIR, and Fused MRI filter models with 10,000, 100,000, and 1,000,000 iterations [4].

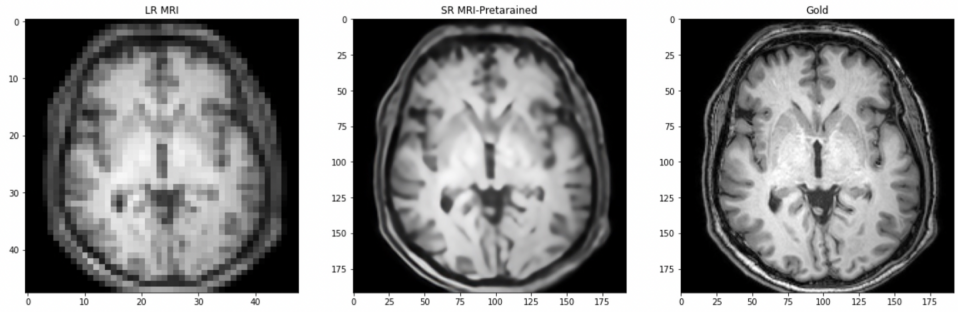


**Figure 5.9** Example result of EDSR algorithm using pretrained model for MRI images.

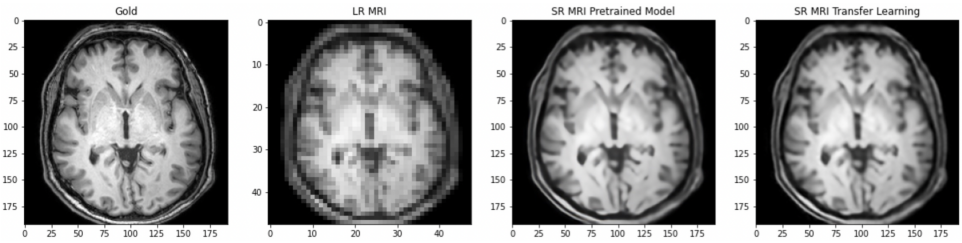


**Figure 5.10** Example result of EDSR algorithm using transfer learning based on only freezing the top layers of the model for MRI images.

interpolation. Super resolved NAA image was generated using EDSR model. SSIM and PSNR values of the NAA, Cho, and Cr images generated by bicubic interpolation and EDSR are given at Table 5.3. Figure 5.13 shows some of the spectra acquired with HR MRSI and that of SR MRSI generated via EDSR.

## 5.5 Discussion

In this study, we have presented a novel application of SRCNN deep learning method for increasing the spatial resolution of $^{1}$H-MRSI based on the anatomical image

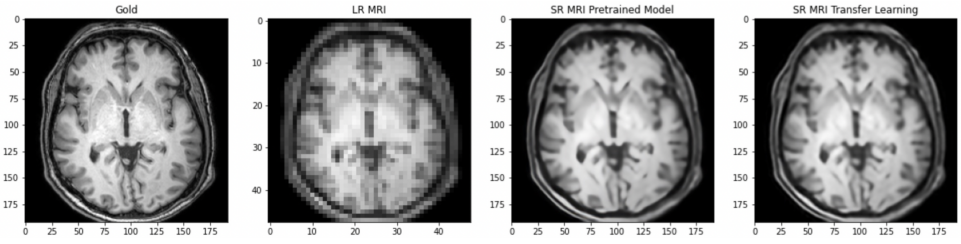


**Figure 5.11** Example result of EDSR algorithm using transfer learning based on both freezing the top layers of the model and training with fine-tuning for MRI images.

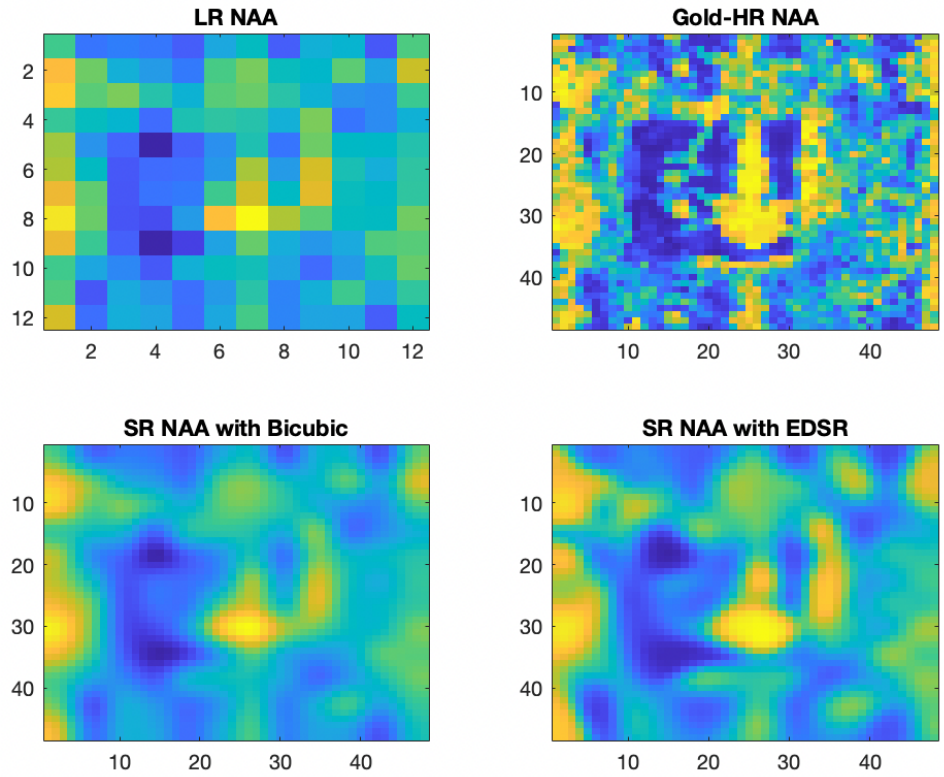


**Figure 5.12** Example result of EDSR algorithm using transfer learning based on both freezing the top layers of the model and training with fine-tuning for NAA images.

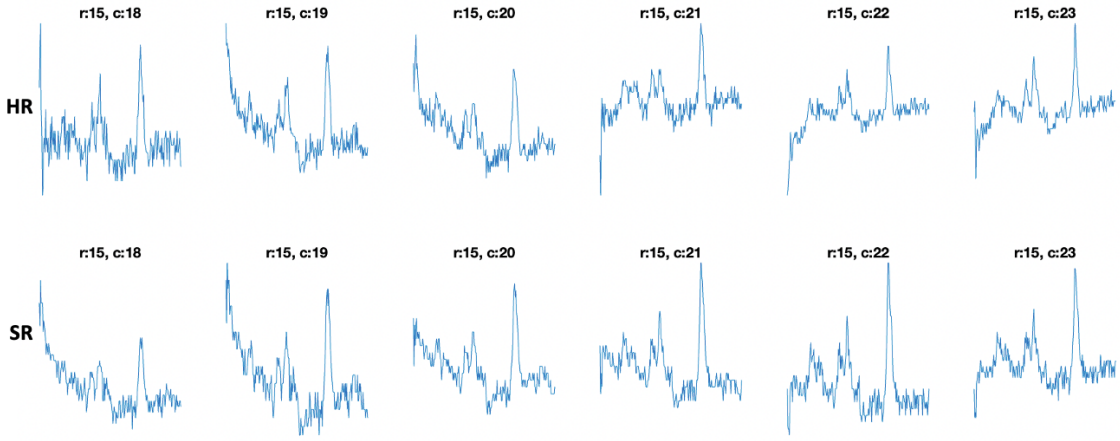


**Figure 5.13** Example spectra visualization of HR and SR MRSI at the selected voxels.

**Table 5.3**
Metric results of super resolved NAA, Cho, and Cr images generated via bicubic interpolation and EDSR network.

| Metric | Method | NAA | Cho | Cr |
|---|---|---|---|---|
| SSIM | Bicubic | 0.293 | 0.290 | 0.291 |
| | SR w/EDSR | 0.372 | 0.367 | 0.364 |
| PSNR | Bicubic | 13.697 | 13.754 | 13.757 |
| | SR w/EDSR | 14.016 | 14.057 | 14.032 |

definition of T1w, T2w, FLAIR, and Fused MRI. One of the main limitations of this study is the use of a single MR spectral frequency point that corresponds to a tNAA map as an example spectral image instead of all the MR spectral points. Our results could be similarly applied to increase the spatial resolution of other metabolite maps that could be obtained by $^{1}$H-MRSI, or a better approach would be the application of the SRCNN models for increasing the spatial resolution of the whole MR spectral array. The proposed approach may contribute to the clinical utility of $^{1}$H-MRSI, e.g. better radiotherapy treatment planning based on higher resolution $^{1}$H-MRSI.

Additional EDSR technique was also adopted as a novel method for getting super resolved MR images. Transfer learning was successfully done with different parameter setups considering only transfer learning with pretrained model, freezing the top layers of the model, and with fine-tuning. Training with fine-tuning resulted in higher PSNR value compared to the other setups. The pre-trained model acquired from anatomical MR images was also applied to NAA, Cho, and Cr images after hyperparameter tuning. This super resolution study had some limitations. The training was only done with anatomical MR images and the application of this method to MR spectroscopic images couldn't be fully accomplished due to the lack of enough many high and low resolved MR spectroscopic imaging data. However, this pipeline will be further optimized and applied once we acquire more low and high resolution MRSI data for training.

# 6. SUMMARY

This thesis has focused on developing software tools for improved $^{1}$H-MRSI. The goals of this dissertation were to develop an open-source user-friendly 3D MRSI data analysis program, called Oryx-MRSI, to use the Oryx-MRSI software for the multivoxel $^{1}$H-MRSI data analysis of PD-MCI patients to define metabolic correlates of MCI, and to improve the resolution of MRSI data using deep learning based super resolution algorithms.

This thesis firstly focused on the open-source software development practices to create a sustainable product and get user feedback with an overarching goal of reaching many users. Oryx-MRSI asks for some parameters before the data analysis, including RF bandwidth of the system for chemical shift correction, cut-off values for voxel exclusion criteria based on FWHM, SNR and CRLB, and cut-off value for the probabilistic binary map after the registration onto MNI152 brain atlas. Oryx-MRSI has nine different modules. *Load data* is the first one and this module reads the raw 1H-MRSI data, and a skull stripped T1-weighted or T2-weighted MRI, and allows for a visualization of the spectra. *Co-registration* module enables chemical shift correction for users. If chemical shift correction is 'on', then the chemical shift misregistration amount is calculated for each metabolite according to the RF pulse bandwidths for each direction provided on the Main Page. Then, shifted metabolite maps are generated considering the MR image space data order and the respective location. *Segmentation* module calculates the WM, GM and CSF fractions in each voxel for every metabolite, which vary due to chemical shift misregistration. *CRLB, FWHM, SNR* module reads LCModel .table files to get CRLB, FWHM, and SNR values of each voxel to create and visualize multivoxel CRLB, FWHM, SNR maps. *Spectral quality* module displays voxels included in the $^{1}$H-MRSI data analysis for each metabolite after the FWHM, SNR, CRLB, and fCSF exclusion criteria defined on the Main Page are applied. *Metabolite maps* reads the LCModel .table files and they are parsed using a text reader and each metabolite result is positioned into a 3D grid in accordance with the MR im-

age space data to create several maps, which are the concentration, CSF corrected concentration, and concentration or CSF corrected concentration to mI and tCr ratio maps. *Registration* module registers the reference anatomical MRI onto MNI152 brain atlas to obtain a transformation matrix. Then, this transformation matrix is used to register the PRESS box and all the concentration or ratio maps that were previously co-registered to the anatomical MRI onto the MNI152 brain atlas. *ROI Analysis* is a new feature not provided by former MRSI data analysis tools. The metabolic maps can be evaluated at brain parcellations defined on MNI anatomical atlas and rs-fMRI networks to define a mean, median and SD value of the concentration map of interest at these brain regions. *Distributions* module displays a box plot showing the distribution of a chosen metabolite at a selected location for a better visual evaluation. This software contributes to the open-source community and makes MRSI data analysis easier. Additionally, sharing the software on GitHub allows for reaching more users for feedback while keeping the software sustainable.

This thesis also consisted of the first clinical application of Oryx-MRSI in which we investigated the metabolic biomarkers of MCI in PD in comparison to PD-CN and HC. Supervised machine learning algorithms were applied to classify HC, PD-CN, and PD-MCI groups based on metabolite levels, and the HC and PD-MCI patients were successfully classified with over 80% accuracy using bagged trees. As a result of this study, $^{1}$H-MRSI revealed metabolic changes in the default mode, ventral attention/salience, and sensorimotor networks of PD-MCI patients, which could be summarized mainly as 'posterior cortical metabolic changes' related with cognitive dysfunction. The main contribution of this study was defining early metabolic changes of the cognitive dysfunction in Parkinson's disease using Oryx-MRSI, which might aid clinicians with the diagnosis of MCI.

This thesis also focused on deep learning based techniques to improve the spatial resolution of $^{1}$H-MRSI. The application of SRCNN for increasing the spatial resolution of 1H-MRSI was presented first. Our results indicated that SRCNN would contribute to reconstructing higher resolution $^{1}$H-MRSI. Additionally, more recent EDSR algorithm was applied to increase the resolution of MRI and MRSI images via transfer learning.

The preliminary results completed with only 4 MRSI data showed higher PSNR and SSIM values for super resolved NAA, Cho, and Cr images generated via EDSR compared to the images upscaled by using bicubic interpolation. The spectral visualization revealed that the spectral pattern was preserved after the EDSR application.

This research had some limitations. The chemical shift directions and formulations for Oryx-MRSI must be validated for use with different MR vendors, because they were computed for a single MR vendor. Additionally, Oryx-MRSI currently only supports transverse slice orientation and 3D scan mode. Since FSL cannot run natively on Windows operating systems, only macOS and Linux are supported for running Oryx-MRSI. In the second study, the $^{1}$H-MRSI data was acquired using PRESS sequence, which is known to be more susceptible to the chemical shift artifact than the semi-LASER sequence. Additionally, registration of $^{1}$H-MRSI data was done using the MNI152 brain atlas, which is based on healthy and young subjects. However, our subject population had a mean age of 60 years, and registration into the MNI152 atlas might have resulted in slight regional shifts between subjects. In the last section of this thesis, training based on both SRCNN and EDSR techniques were only completed with anatomical MR images and the application of this method to the whole MR spectroscopic data couldn't be fully accomplished due to the limited number of available high and low resolved MR spectroscopic imaging data.

As a future work for Oryx-MRSI, a voxel-based statistical analysis module will be developed in addition to the ROI analysis. Oryx-MRSI will be continuously updated to provide support for different MR vendors, and possible integration with earlier open-source MRS data analysis tools. Additionally, a future study including PD dementia patients might help to elucidate the metabolite changes along the cognitive decline continuum. Moreover, an integrated analysis of $^{1}$H-MRSI data with other multimodality MR images after registration into an age matched brain template would possibly result in a better definition of the metabolic markers of cognitive impairment in PD. Lastly, further work could increase the number of input channels (e.g. adding other structural MR sequences or diffusion parametric maps to the 3-channel [T1W, T2W, FLAIR] input array that was evaluated here) to investigate the optimal input configuration

for increasing the spatial resolution of $^{1}$H-MRSI. Additional studies will be conducted to investigate the use of other deep learning methods, like SRGAN and MSR, to increase the spatial resolution of $^{1}$H-MRSI and these pipelines will be applied on a high number of real low and high resolution MRSI data. The results of this dissertation can be utilized for improved and unified $^{1}$H-MRSI data analysis along with other MRI modalities, and might also help with higher spatial resolution metabolic imaging to better define the metabolic changes that occur in the brain with diseases such as the Parkinson's disease.

# APPENDIX A. Publications

## Publications

First author

1. **Cengiz S,** Arslan DB, Kicik A, Erdogdu E, Yildirim M, Hatay GH, Tufekcioglu Z, Ulug AZ, Bilgic B, Hangasi H, Demiralp T, Gurvit H, Ozturk-Isik E. Identification of metabolic correlates of mild cognitive impairment in Parkinson's disease using magnetic resonance spectroscopic imaging and machine learning. Magn Reson Mater Phy (2022). https://doi.org/10.1007/s10334-022-01030-6

2. **Cengiz S,** Yildirim M, Bas A, Ozturk-Isik E (2022) ORYX-MRSI: A fully-automated open-source software for proton magnetic resonance spectroscopic imaging data analysis. Int J Imaging Syst Technol. doi: 10.1002/ima.22748

3. **Cengiz S,** ValdesHernandez MC, Ozturk-Isik E, (2017) Super Resolution Convolutional Neural Networks for Increasing Spatial Resolution of $^{1}$H Magnetic Resonance Spectroscopic Imaging. In: Valdes Hernandez M., Gonzalez-Castro V. (eds) Medical Image Understanding and Analysis. MIUA 2017. Communications in Computer and Information Science, vol 723. Springer. (Book chapter) doi: 10.1007/978-3-319-60964-5_56

Not first author

1. Azamat S, Betul Arslan D, Erdogdu E, Kicik A, **Cengiz S,** Eryurek K, Tufekcioglu Z, Bilgic B, Hanagasi H, Demiralp T, Gurvit H, Ozturk-Isik E (2021) Detection of visual and frontoparietal network perfusion deficits in Parkinsonâs disease dementia. Eur J Radiol 144:109985.

2. Arslan DB, Gurvit H, Genc O, Kicik A, Eryurek K, **Cengiz S,** Erdogdu E, Yildirim Z, Tufekcioglu Z, Ulug AM, Bilgic B, Hanagasi H, Tuzun E, Demiralp

T, Ozturk-Isik E (2020) The cerebral blood flow deficits in Parkinsonâs disease with mild cognitive impairment using arterial spin labeling MRI. J Neural Transm 127:1285â1294.

3. Ozturk-Isik E, **Cengiz S,** Ozcan A, Yakicier MC, Ersen A, Pamir M, Ozduman K, Dincer A (2019). Identification of IDH and TERTp mutation status using $^{1}$HâMRS in 112 hemispheric diffuse gliomas. Journal of Magnetic Resonance Imaging. 10.1002/jmri.26964.

**International Conference Proceedings and Abstracts**

First author

1. **Cengiz S,** Yildirim M, Bas A, Ozturk-Isik E. ORYX-MRSI: A data analysis software for multi-slice $^{1}$H-MRSI. International Society for Magnetic Resonance in Medicine. Virtual Meeting, May 15-20, 2021. (digital poster)

2. **Cengiz S,** Yildirim Z, Arslan DB, Kicik A, Erdogdu E, Yildirim M, Tufekcioglu Z, Bilgic B, Hanagasi H, Ulug AM, Gurvit IH, Demiralp T, Ozturk-Isik E. MRSI Based Biomarkers of Parkinson's Disease with Mild Cognitive Impairment at Resting State fMRI Based Brain Parcellations. Alzheimerâs Association International Conference. Los Angeles, USA, July 14-18, 2019. (poster)

3. **Cengiz S,** Arslan DB, Kicik A, Erdogdu E, Yildirim M, Tufekcioglu Z, Bilgic B, Hanagasi H, Ulug AM, Gurvit H, Demiralp T, Ozturk−Isik E, Magnetic resonance spectroscopic imaging based biomarkers of Parkinson's disease with mild cognitive impairment registered to MNI152 brain atlas after chemical shift correction. International Society for Magnetic Resonance in Medicine. Paris, France, June 16−21, 2018. (Oral Power Pitch Presentation).

4. **Cengiz S,** Super Resolution Convolutional Neural Networks for Increasing Spatial Resolution of $^{1}$H Magnetic Resonance Spectroscopic Imaging. Medical Image Understanding and Analysis (MIUA) 2017. Edinburgh, UK, July 11-13, 2017. (Oral Presentation).

5. **Cengiz S,** Arslan DB, Kicik A, Erdogdu E, Buker S, Tufekcioglu Z, Ulug AM, Bilgic B, Hanagasi H, Gurvit H, Demiralp T, Ozturk-Isik E, Correlation of MRSI based biomarkers and neuropsychological test scores in Parkinson's disease at 3T. Organization for Human Brain Mapping. Vancouver, Canada, June 25-29, 2017. (Poster).

6. **Cengiz S,** Arslan DB, Kicik A, Erdogdu E, Buker S, Tufekcioglu Z, Ulug AM, Bilgic B, Hanagasi H, Gurvit H, Demiralp T, Ozturk-Isik E, Correlation of cerebral perfusion and metabolic biomarkers in Parkinson's disease with mild cognitive impairment using ASL-MRI and 1H-MRSI at 3T. Organization for Human Brain Mapping. Vancouver, Canada, June 25-29, 2017. (Poster).

7. **Cengiz S,** Kicik A, Erdogdu E, Arslan DB, Buker S, Tufekcioglu Z, Ulug AM, Bilgic B, Hanagasi H, Gurvit H, Demiralp T, Ozturk-Isik E, Comparison of MR spectroscopic imaging findings between different MAPT and COMT genotypes of cognitively normal or mild cognitively impaired Parkinson's disease patients at 3T. International Society for Magnetic Resonance in Medicine. Honolulu, HI, USA, 22-27 April 2017. (Traditional Poster).

8. **Cengiz S,** Arslan DB, Erdogdu E, Kicik A, Hatay GH, Tufekcioglu Z, Bilgic B, Hanagasi H, Ulug AM, Gurvit H, Demiralp T, Ozturk-Isik E, Proton MR spectroscopic imaging of Parkinson's disease with mild cognitive impairment or normal cognition registered to MNI152 brain atlas. European Society of Magnetic Resonance in Medicine and Biology Annual Conference. Vienna, Austria, 29-1 October, 2016. (Oral Presentation).

<u>Not first author</u>

1. Arslan DB, Gurvit H, Genc O, Kicik A, Eryurek K, **Cengiz S,** Erdogdu E, Yildirim Z, Tufekcioglu Z, Ulug AM, Bilgic B, Hanagasi H, Demiralp T, Ozturk-Isik E. The perfusion deficits in general cognitive, executive, and visual dysfunction in Parkinson's disease measured by arterial spin labeling MRI. International

Society for Magnetic Resonance in Medicine. Virtual Meeting, 15-20 May, 2021. (digital poster)

2. Azamat S, **Cengiz S,** Arslan DB, Kicik A, Erdogdu E, Bilgic B, Hanagasi H, Gurvit H, Demiralp T, Ozturk-Isik E. Determination of Cognitive Impairment in Parkinson's Disease Using Proton Magnetic Resonance Spectroscopic Imaging Based Biomarkers, European Society of Magnetic Resonance in Medicine and Biology Annual Conference. Virtual Meeting, September 30-October 2, 2020.

3. Arslan DB, Gurvit H, Genc O, Kicik A, Eryurek K, **Cengiz S,** Erdogdu E, Yildirim Z, Tufekcioglu Z, Ulug AM, Bilgic B, Hanagasi H, Demiralp T, Ozturk-Isik E. The Cerebral Blood Flow Changes in Parkinson's Disease with Mild Cognitive Impairment Using Arterial Spin Labeling MRI. International Society for Magnetic Resonance in Medicine. Virtual Meeting, August 8-14, 2020. (e-poster)

4. Arslan DB, Gurvit H, Genc O, Kicik A, Eryurek K, **Cengiz S,** Erdogdu E, Yildirim Z, Tufekcioglu Z, Ulug AM, Bilgic B, Hanagasi H, Demiralp T, Ozturk-Isik E. Perfusion-Based Biomarkers of Mild Cognitive Impairment in Parkinson's disease with different MAPT haplotypes using Arterial Spin Labeling MRI. International Society for Magnetic Resonance in Medicine. Virtual Meeting, August 8-14, 2020. (e-poster)

5. Arslan DB, Yildirim Z, **Cengiz S,** Kicik A, Erdogdu E, Tufekcioglu Z, Bilgic B, Hangasi H, Ulug AM, Demiralp T, Gurvit IH, Ozturk-Isik E. Cerebral Blood Flow Changes in Different Mapt Genotypes of Parkinsonâs Disease at Cerebral Cortex Parcellations Obtained from Resting State fMRI. Alzheimer's Association International Conference. Los Angeles, USA, July 14-18, 2019. (poster)

6. Arslan DB, **Cengiz S,** Eryurek K, Genc O, Kicik A, Erdogdu E, Tufekcioglu Z, Bilgic B, Hanagasi H, Ulug AM, Gurvit H, Demiralp T, Ozturk-Isik E. Longitudinal Changes in Cerebral Blood Flow Calculated by Arterial Spin Labeling MRI in Parkinson's Disease. International Society for Magnetic Resonance in Medicine. Montreal, Canada, May 11-16, 2019. (digital poster)

7. Arslan DB, **Cengiz S,** Kicik A, Erdogdu E, Yildirim Z, Tufekcioglu Z, Bilgic

B, Hanagasi H, Ulug AM, Demiralp T, Gurvit H, Ozturk-Isik E. The Cerebral Blood Flow Changes of Executive Dysfunction in Parkinson's Disease Measured by Arterial Spin Labeling MRI at Cerebral Cortex Parcellations Obtained from Resting State fMRI. International Society for Magnetic Resonance in Medicine. Montreal, Canada, May 11-16, 2019. (digital poster)

8. Erdogdu E, Kicik A, Arslan DB, **Cengiz S,** Buker S, Tufekcioglu Z, Ozturk-Isik E, Bilgic B, Hanagasi H, Ulug AM, Basar-Eroglu C, Gurvit H, Demiralp T. DTI measures to track cognitive decline in Parkinson's disease with MCI and Dementia. Rome, Italy, June 9-13, 2019. (poster)

9. Ay U, Erdogdu E, Kicik A, Bayram A, Arslan D, Tufekcioglu Z, **Cengiz S,** Ozturk-Isik E, Bilgic B, Hanagasi H, Ulug AM, Gurvit H, Demiralp T. Structural Changes in Neurocognitive Networks Related with Cognitive Decline in Parkinson's Disease. Organization for Human Brain Mapping. Rome, Italy, June 9-13, 2019. (poster)

10. Arslan DB, Kicik A, **Cengiz S,** Erdogdu E, Buker S, Tufekcioglu Z, Ulug AM, Bilgic B, Hanagasi H, Gurvit H, Demiralp T, Ozturk-Isik E, Cerebral Perfusion Correlates of MAPT and COMT Genotypes for Mild Cognitive Impairment in Parkinson's Disease at 3T. International Society for Magnetic Resonance in Medicine. Honolulu, HI, USA, 22-27 April 2017. (Traditional Poster).

11. Ozturk-Isik E, **Cengiz S,** Arslan DB, Kicik A, Erdogdu E, Tufekcioglu Z, Bilgic B, Hanagasi H, Ulug AM, Demiralp T, Gurvit H. Machine Learning for Classification of Mild Cognitive Impairment in Parkinson's Disease Based on Multiparametric MRI at 3T. European Society of Magnetic Resonance in Medicine and Biology Annual Conference. Barcelona, Spain, 19-21 October 2017. (e-poster)

12. Ulug AM, Ozturk-Isik E, Kicik A, Erdogdu E, **Cengiz S,** Arslan DB, Bayram A, Ulasoglu-Yildiz C, Kurt E, Tufekcioglu Z, Bilgic B, Hanagasi H, Demiralp T, Gurvit H. Diffusion discriminant for mild cognitive impairment in Parkinson's disease. International Society of Magnetic Resonance in Medicine Annual Conference, Honolulu, HI, USA, 22-27 April 2017. (Traditional poster).

13. Arslan DB, **Cengiz S,** Kicik A, Erdogdu E, Buker S, Tufekcioglu Z, Ulug AM, Bilgic B, Hanagasi H, Gurvit H, Demiralp T, Ozturk-Isik E, Association of Arterial Spin Labeling MRI with Neurophysiological Test Scores in Parkinson's Disease. Organization for Human Brain Mapping. Vancouver, Canada, June 25-29, 2017. (Poster).

14. Erdogdu E, Kicik A, Buker S, Tufekcioglu Z, Arslan DB, **Cengiz S,** Ozturk-Isik E, Bilgic B, Hanagasi H, Ulug AM, Basar-Eroglu C, Demiralp T, Gurvit H, Functional connectivity changes at different stages of cognitive decline in Parkinson's disease. Organization for Human Brain Mapping. Vancouver, Canada, June 25-29, 2017. (Poster).

15. Arslan DB, **Cengiz S,** Kicik A, Erdogdu E, Hatay GH, Tufekcioglu Z, Bilgic B, Ulug AM, Hanagasi H, Gurvit H, Demiralp T, Ozturk-Isik E, Comparison of cerebral blood volume and arterial blood volume between Parkinson's disease patients with mild cognitive impairment and normal cognition using arterial spin labeling MR at 3T. European Society of Magnetic Resonance in Medicine and Biology Annual Conference. Vienna, Austria, October 29- 1 2016. (Oral Presentation).

**National Conference Proceedings and Abstracts**

First author

1. **Cengiz S,** Yildirim Z, Arslan DB, Kicik A, Erdogdu E, Yildirim M, Tufekcioglu Z, Bilgic B, Hanagasi H, Ulug AM, Gurvit H, Demiralp T, Ozturk-Isik E. Parkinson Hastalığı Hafif Kognitif Bozukluğunun Korteks Parselasyonlarinda MR Spektroskopik Görüntüleme Temelli Biyoişaretleyicileri. Ulusal Nöroloji Kongresi. Antalya, Turkey, November 16-20, 2019. (oral Presentation)

2. **Cengiz S,** Advances in magnetic resonance spectroscopic image processing. Workshop on Recent Advances in Magnetic Resonance Imaging at Bogazici University. Istanbul, Turkey, June 20th, 2017 (Oral Presentation).

3. **Cengiz S,** Arslan DB, Erdogdu E, Kicik A, Hatay GH, Tufekcioglu Z, Bilgic B, Hanagasi H, Ulug AM, Gurvit H, Demiralp T, Ozturk-Isik E. Hafif Kognitif Bozukluğu Olan ve Kognitif Normal Parkinson Hastalarının Üç Boyutlu $^{1}$H Manyetik Rezonans Spektroskopik Görüntüleme Verilerinin Karşılaştırılması. Türk Manyetik Rezonans Derneği. 2016. Ankara, Turkey, May 26-28, 2016. (oral presentation)

Not first author

1. Arslan DB, Yildirim Z, **Cengiz S,** Kicik A, Erdogdu E, Tufekcioglu Z, Bilgic B, Hanagasi H, Ulug AM, Demiralp T, Gurvit H, Ozturk-Isik E. Parkinson Hastalığında MAPT Genotiplerinde Korteks Parselasyonlarında Serebral Kan Akımı Değişiklikleri. Ulusal Nöroloji Kongresi. Antalya, Turkey, November 16-20, 2019. (oral Presentation)

2. Tufekcioglu Z, Cebi M, Tuncer S, Arslan DB, Ipek TD, Aslan O, **Cengiz S,** Kicik A, Erdogdu E, Yildirim Z, Bilgic B, Hanagasi H, Ulug AM, Demiralp T, Gurvit H ve Ozturk-Isik E. Parkin Gen Mutasyonu Taşıyan Bireylerde Serebral Kan Akımının Değerlendirilmesi ve Kognitif Normal Parkinson Hastaları ile Karşılaştırılması. Ulusal Nöroloji Kongresi. Antalya, Turkey, November 16-20, 2019. (oral Presentation)

3. Tuncer S, Arslan DB, Ipek TD, Aslan O, **Cengiz S,** Kicik A, Erdogdu E, Yildirim Z, Tufekcioglu Z, Bilgic B, Hanagasi H, Ulug AM, Demiralp T, Gurvit H, Ozturk-Isik E. Parkinson Hastalarında Kognitif Bozulmanın Arteriyel Spin Etiketleme Manyetik Rezonans Görüntüleme Temelli Biyoişaretleyicilerinin Değerlendirilmesi. Ulusal Nöroloji Kongresi. Antalya, Turkey, November 16-20, 2019. (oral Presentation)

4. Erdogdu E, Kicik A, Buker S, Tufekcioglu Z, Arslan DB, **Cengiz S,** Ozturk-Isik E, Bilgic B, Hanagasi H, Ulug AM, Basar-Eroglu C, Gurvit H, Demiralp T. Parkinson Hastalığı Demansının Beyin işlevsel Bağlantısallık Özellikleri. Ulusal Nöroloji Kongresi. Antalya, Turkey, November 16-20, 2019. (poster)

5. Arslan DB, **Cengiz S,** Erdogdu E, Kicik A, Tufekcioglu Z, Bilgic B, Hanagasi H, Ulug AM, Gurvit H, Demiralp T, Ozturk-Isik E. ASL-MR ile Parkinson hastalığı hafif kognitif bozukluğunda serebral perfüzyon değerlendirmesi. Ulusal Sinirbilim Kongresi, Istanbul, Turkey, May 20-23, 2018. (Oral Presentation)

6. Genc O, Arslan DB, **Cengiz S,** Hatay GH, Kicik A, Erdogdu E, Kaplan OC, Tufekcioglu Z, Bilgic B, Hanagasi H, Gurvit H, Demiralp T, Ulug AM, Ozturk-Isik E. Parkinson hastalığı hafif kognitif bozukluğunun MRG temelli makine öğrenme ile sınıflandırılması. Ulusal Sinirbilim Kongresi. Istanbul, Turkey, May 20-23, 2018. (Oral Presentation)

7. Kicik A, Erdogdu E, Arslan DB, **Cengiz S,** Bilgic B, Tufekcioglu Z, Hanagasi H, Ulug AM, Tuzun E, Demiralp T, Ozturk-Isik E, Gurvit H. Parkinson hastalığında kognitif bozulmayla ilişkili yapısal ve fonksiyonel farklılıklar. Ulusal Sinirbilim Kongresi. Istanbul, Turkey, May 20-23, 2018. (Oral Presentation)

8. Kaplan OC, Arslan DB, **Cengiz S,** Kicik A, Erdogdu E, Hatay GH, Tufekcioglu Z, Bilgic B, Hanagasi H, Gurvit H, Demiralp T, Ulug AM, Ozturk-Isik E. Parkinson Hastalığı Hafif Kognitif Bozukluğunun DifÃ¼zyon Ağırlıklı Manyetik Rezonans Görüntüleme Temelli Biyoişaretleyicilerinin Belirlenmesi. Biyomut. Istanbul, Turkey, November 24-26, 2017. (Poster)

9. Kicik A, Erdogdu E, Tufekcioglu Z, Arslan DB, **Cengiz S,** Buker S, Bilgic B, Hanagasi H, Ulug AM, Basar-Eroglu C, Tuzun E, Demiralp T, Ozturk-Isik E, Gurvit H. Parkinson hastalığında kognitif bozulma ve beynin fonksiyonel bağlantısallık ağları. Ulusal Sinirbilim Kongresi. Sakarya, Turkey. May 7-10, 2017.

10. Arslan DB, **Cengiz S,** Erdogdu E, Kicik A, Hatay GH, Tufekcioglu Z, Bilgic B, Hanagasi H, Ulug AM, Gurvit H, Demiralp T, Ozturk-Isik E. Atardamar Fırıl Etiketleme Manyetik Rezonans Görüntüleme Tekniği Kullanılarak Kognitif Normal ve Hafif Kognitif Bozukluğu olan Parkinson Hastalarının Serebral Kan Akım Değerlerinin Karşılaştırılması. Türk Manyetik Rezonans Derneği. 2016. Ankara, Turkey, May 26-28, 2016. (oral presentation)

11. Kicik A, Erdogdu E, Buker S, Tufekcioglu Z, Arslan DB, **Cengiz S,** Ozturk-Isik

E, Bilgic B, Hanagasi H, Ulug AM, Gurvit H. Parkinson hastalığında hafif kognitif bozuklukla ilişkili dinlenim durumu fonksiyonel bağlantısallık ağları. 14.Ulusal Sinir Bilim Kongresi 2016. Ankara, Turkey, May 26-29, 2016.

# REFERENCES


1. Mukherji, S., "Clinical Applications of Magnetic Resonance Spectroscopy," *Wiley*, 1998.

2. Cengiz, S., M. Yildirim, A. Bas, and E. Ozturk-Isik, "ORYX-MRSI: A fully-automated open-source software for proton magnetic resonance spectroscopic imaging data analysis," *International Journal of Imaging Systems and Technology*, Vol. 32, pp. 1068–1083, jul 2022.

3. Cengiz, S., *et al.*, "Identification of metabolic correlates of mild cognitive impairment in Parkinson's disease using magnetic resonance spectroscopic imaging and machine learning," *Magnetic Resonance Materials in Physics, Biology and Medicine*, 2022.

4. Cengiz, S., M. d. C. Valdes-Hernandez, and E. Ozturk-Isik, "Super resolution convolutional neural networks for increasing spatial resolution of 1h magnetic resonance spectroscopic imaging," in *Medical Image Understanding and Analysis* (Valdés Hernández, M., and V. González-Castro, eds.), (Cham), pp. 641–650, Springer International Publishing, 2017.

5. Dong, C., C. C. Loy, K. He, and X. Tang, "Image Super-Resolution Using Deep Convolutional Networks," *IEEE Transactions on Pattern Analysis and Machine Intelligence*, Vol. 38, no. 2, pp. 295–307, 2016.

6. Lim, B., *et al.*, "Enhanced deep residual networks for single image super-resolution," *IEEE Computer Society Conference on Computer Vision and Pattern Recognition Workshops*, Vol. 2017-July, pp. 1132–1140, 7 2017.

7. Hajjo, R., D. A. Sabbah, S. K. Bardaweel, and A. Tropsha, "Identification of tumor-specific mri biomarkers using machine learning (ml)," *Diagnostics*, Vol. 11, 2021.

8. Luks, T. L., *et al.*, "T2 FLAIR Hyperintensity Volume Is Associated With Cognitive Function and Quality of Life in Clinically Stable Patients With Lower Grade Gliomas," *Frontiers in Neurology*, Vol. 12, p. 2554, 2022.

9. Grade, M., *et al.*, "A neuroradiologist's guide to arterial spin labeling MRI in clinical practice," *Neuroradiology*, Vol. 57, no. 12, pp. 1181–1202, 2015.

10. Salama, G., *et al.*, "Diffusion weighted/tensor imaging, functional mri and perfusion weighted imaging in glioblastoma-foundations and future," *Frontiers in Neurology*, Vol. 8, 2018.

11. Swanberg, K. M., K. Landheer, D. Pitt, and C. Juchem, "Quantifying the metabolic signature of multiple sclerosis by in vivo proton magnetic resonance spectroscopy: Current challenges and future outlook in the translation from proton signal to diagnostic biomarker," *Frontiers in Neurology*, Vol. 10, p. 1173, 11 2019.

12. Horska, A., P. B. Barker, and D. Phil, "Imaging of brain tumors: Mr spectroscopy and metabolic imaging," *Neuroimaging Clin N Am*, Vol. 20(3), pp. 293–310, 2010.

13. Nie, K., *et al.*, "Marked N-acetylaspartate and choline metabolite changes in Parkinson's disease patients with mild cognitive impairment," *Parkinsonism Relat Disord*, Vol. 19, no. 3, pp. 329–334, 2013.

14. Camicioli, R. M., *et al.*, "Posterior cingulate metabolic changes occur in Parkinson's disease patients without dementia," *Neuroscience Letters,*, Vol. 354, no. 3, pp. 177–180, 2004.

15. Hu, M. T., *et al.*, "Evidence for cortical dysfunction in clinically non-demented patients with Parkinson's disease: a proton MR spectroscopy study," *J Neurol Neurosurg Psychiatry*, Vol. 67, no. 1, pp. 20–26, 1999.

16. Summerfield, C., *et al.*, "Dementia in Parkinson disease: a proton magnetic resonance spectroscopy study," *Arch Neurol*, Vol. 59, no. 9, pp. 1415–1420, 2002.

17. Pagonabarraga, J., *et al.*, "Spectroscopic changes associated with mild cognitive impairment and dementia in Parkinson's disease," *Dement Geriatr Cogn Disord*, Vol. 34, no. 5-6, pp. 312–318, 2012.

18. Waragai, M., M. Moriya, and T. Nojo, "Decreased N-Acetyl Aspartate/Myo-Inositol Ratio in the Posterior Cingulate Cortex Shown by Magnetic Resonance Spectroscopy May Be One of the Risk Markers of Preclinical Alzheimer's Disease: A 7-Year Follow-Up Study," *J Alzheimers Dis*, Vol. 60, no. 4, pp. 1411–1427, 2017.

19. Siger, M., *et al.*, "Regional myo-inositol concentration in mild cognitive impairment Using 1H magnetic resonance spectroscopic imaging," *Alzheimer Dis Assoc Disord*, Vol. 23, no. 1, pp. 57–62, 2009.

20. Gao, F., and P. B. Barker, "Various MRS application tools for Alzheimer disease and mild cognitive impairment," *AJNR Am J Neuroradiol*, Vol. 35, no. 6 Suppl, pp. S4–11, 2014.

21. Federico, F., *et al.*, "Proton magnetic resonance spectroscopy in Parkinson's disease and progressive supranuclear palsy," *Neurosurgery, and Psychiatry*, Vol. 62, pp. 239–242, 1997.

22. Ramadan, S., A. Lin, and P. Stanwell, "Glutamate and Glutamine: A Review of In Vivo MRS in the Human Brain," *NMR Biomed.*, Vol. 26(12), pp. 1630–46, 2013.

23. Dorsey, E. R., *et al.*, "Projected number of people with Parkinson disease in the most populous nations, 2005 through 2030," *Neurology*, Vol. 68, no. 5, pp. 384–386, 2007.

24. Angel, R. W., W. Alston, and J. R. Higgins, "Control of movement in Parkinson's disease," *Brain*, Vol. 93, no. 1, pp. 1–14, 1970.

25. Schapira, A. H. V., K. R. Chaudhuri, and P. Jenner, "Non-motor features of Parkinson disease," *Nat Rev Neurosci*, Vol. 18, no. 8, p. 509, 2017.

26. Litvan, I., *et al.*, "MDS Task Force on mild cognitive impairment in Parkinson's disease: critical review of PD-MCI," *Mov Disord*, Vol. 26, no. 10, pp. 1814–1824, 2011.

27. Aarsland, D., and M. W. Kurz, "The epidemiology of dementia associated with Parkinson's disease," *Brain Pathol*, Vol. 20, no. 3, pp. 633–639, 2010.

28. Janvin, C. C., J. P. Larsen, D. Aarsland, and K. Hugdahl, "Subtypes of mild cognitive impairment in Parkinson's disease: progression to dementia," *Mov Disord*, Vol. 21, no. 9, pp. 1343–1349, 2006.

29. Chang, L., S. M. Munsaka, S. Kraft-Terry, and T. Ernst, "Magnetic Resonance Spectroscopy to Assess NeuroInflammation and Neuropathic Pain," *Journal of neuroimmune pharmacology : the official journal of the Society on NeuroImmune Pharmacology*, no. 3, p. 576, 2013.

30. Quadrelli, S., C. Mountford, and S. Ramadan, "Hitchhiker's Guide to Voxel Segmentation for Partial Volume Correction of In Vivo Magnetic Resonance Spectroscopy," *Magnetic Resonance Insights*, Vol. 9, p. MRI.S32903, jan 2016.

31. Ozturk-Isik, E., *et al.*, "Unaliasing lipid contamination for MR spectroscopic imaging of gliomas at 3T using sensitivity encoding (SENSE)," *Magn Reson Med*, Vol. 55, no. 5, pp. 1164–1169, 2006.

32. Hajek, M., and M. Dezortova, "Introduction to clinical in vivo MR spectroscopy," *European Journal of Radiology*, Vol. 67, pp. 185–193, aug 2008.

33. Lange, T., *et al.*, "Pitfalls in Lactate Measurements at 3T," *AJNR Am J Neuroradiol*, Vol. 27(4), pp. 895–901, 2006.

34. Di Costanzo, A., *et al.*, "Proton MR spectroscopy of the brain at 3 T: an update," *European Radiology*, Vol. 17, pp. 1651–1662, jul 2007.

35. Dong, C., C. C. Loy, K. He, and X. Tang, "Learning a deep convolutional network for image super-resolution," *Lecture Notes in Computer Science (including subseries Lecture Notes in Artificial Intelligence and Lecture Notes in Bioinformatics)*, Vol. 8692 LNCS, no. PART 4, pp. 184–199, 2014.

36. Luo, Y., L. Zhou, S. Wang, and Z. Wang, "Video Satellite Imagery Super Resolution via Convolutional Neural Networks," *IEEE Geoscience and Remote Sensing Letters*, Vol. 14, pp. 2398–2402, dec 2017.

37. Pham, C. H., A. Ducournau, R. Fablet, and F. Rousseau, "Brain MRI super-resolution using deep 3D convolutional networks," *Proceedings - International Symposium on Biomedical Imaging*, pp. 197–200, 2017.

38. Lam, F., and Z. P. Liang, "A subspace approach to high-resolution spectroscopic imaging," *Magnetic Resonance in Medicine*, Vol. 71, pp. 1349–1357, apr 2014.

39. Mok, T. C., and A. C. Chung, "Conditional Deformable Image Registration with Convolutional Neural Network," *Lecture Notes in Computer Science*, Vol. 12904 LNCS, pp. 35–45, 2021.

40. Iqbal, Z., *et al.*, "Super-Resolution 1H Magnetic Resonance Spectroscopic Imaging Utilizing Deep Learning," *Frontiers in Oncology*, Vol. 9, p. 1010, oct 2019.

41. Dong, S., *et al.*, "High-Resolution Magnetic Resonance Spectroscopic Imaging using a Multi-Encoder Attention U-Net with Structural and Adversarial Loss," *Annual International Conference of the IEEE Engineering in Medicine and Biology Society. IEEE Engineering in Medicine and Biology Society. Annual International Conference*, Vol. 2021, pp. 2891–2895, 2021.

42. Wang, Z., J. Chen, and S. C. Hoi, "Deep Learning for Image Super-resolution: A Survey," *IEEE Transactions on Pattern Analysis and Machine Intelligence*, Vol. 43, pp. 3365–3387, feb 2019.

43. De Graaf, R. A., *Basic Principles*, ch. 1, pp. 1–42. John Wiley  Sons, Ltd, 2019.

44. Ross, B., and S. Bluml, "Magnetic Resonance Spectroscopy of the Human Brain," *The Anatomical Record*, Vol. 265, no. 2, pp. 54–84, 2001.

45. Govindaraju, V., K. Young, and A. A. Maudsley, "Proton NMR chemical shifts and coupling constants for brain metabolites," *NMR Biomed*, Vol. 13, no. 3, pp. 129–153, 2000.

46. Pfeuffer, J., I. Tkáč, S. W. Provencher, and R. Gruetter, "Toward an in vivo neurochemical profile: quantification of 18 metabolites in short-echo-time (1)H NMR spectra of the rat brain," *Journal of Magnetic Resonance*, Vol. 141, no. 1, pp. 104–120, 1999.

47. Öz, G., *et al.*, "Proton MRS of the unilateral substantia nigra in the human brain at 4 tesla: detection of high GABA concentrations," *Magnetic Resonance in Medicine*, Vol. 55, no. 2, pp. 296–301, 2006.

48. Brambilla, P., *et al.*, "GABAergic dysfunction in mood disorders," *Molecular Psychiatry*, Vol. 8, no. 8, pp. 721–737, 2003.

49. Sanacora, G., *et al.*, "Reduced cortical gamma-aminobutyric acid levels in depressed patients determined by proton magnetic resonance spectroscopy," *Archives of general psychiatry*, Vol. 56, pp. 1043–1047, nov 1999.

50. Sanacora, G., *et al.*, "Subtype-specific alterations of gamma-aminobutyric acid and glutamate in patients with major depression," *Arch Gen Psychiatry*, Vol. 61, pp. 705–713, jul 2004.

51. Petroff, O. A., F. Hyder, D. L. Rothman, and R. H. Mattson, "Homocarnosine and seizure control in juvenile myoclonic epilepsy and complex partial seizures," *Neurology*, Vol. 56, pp. 709–715, mar 2001.

52. Goddard, A. W., *et al.*, "Reductions in occipital cortex GABA levels in panic disorder detected with 1h-magnetic resonance spectroscopy," *Archives of general psychiatry*, Vol. 58, no. 6, pp. 556–561, 2001.

53. Tan, J., *et al.*, "Lack of effect of oral choline supplement on the concentrations of choline metabolites in human brain," *Magnetic Resonance in Medicine*, Vol. 39, pp. 1005–1010, jun 1998.

54. Wang, Y., and S. J. Li, "Differentiation of metabolic concentrations between gray matter and white matter of human brain by in vivo 1H magnetic resonance spectroscopy," *Magnetic Resonance in Medicine*, Vol. 39, no. 1, pp. 28–33, 1998.

55. Pouwels, P. J., and J. Frahm, "Regional metabolite concentrations in human brain as determined by quantitative localized proton MRS," *Magnetic Resonance in Medicine*, Vol. 39, pp. 53–60, jan 1998.

56. Keltner, J. R., *et al.*, "A localized double-quantum filter for the in vivo detection of brain glucose," *Magnetic Resonance in Medicine*, Vol. 39, no. 4, pp. 651–656, 1998.

57. De Graaf, R. A., Y. Luo, M. Terpstra, and M. Garwood, "Spectral Editing with Adiabatic Pulses," *JJournal of Magnetic Resonance, Series B*, Vol. 109, pp. 184–193, nov 1995.

58. Ross, B. D., "Biochemical considerations in 1h spectroscopy. glutamate and glutamine; myo-inositol and related metabolites," *NMR in Biomedicine*, Vol. 4, no. 2, pp. 59–63, 1991.

59. Bruhn, H., *et al.*, "Noninvasive differentiation of tumors with use of localized H-1 MR spectroscopy in vivo: initial experience in patients with cerebral tumors," *Radiology*, Vol. 172, no. 2, pp. 541–548, 1989.

60. Majós, C., *et al.*, "Brain Tumor Classification by Proton MR Spectroscopy: Comparison of Diagnostic Accuracy at Short and Long TE," *AJNR: American Journal of Neuroradiology*, Vol. 25, p. 1696, nov 2004.

61. Gideon, P., *et al.*, "Early time course of N-acetylaspartate, creatine and phosphocreatine, and compounds containing choline in the brain after acute stroke. A proton magnetic resonance spectroscopy study," *Stroke*, Vol. 23, no. 11, pp. 1566–1572, 1992.

62. Bruhn, H., *et al.*, "Cerebral metabolism in man after acute stroke: new observations using localized proton NMR spectroscopy," *Magnetic Resonance in Medicine*, Vol. 9, no. 1, pp. 126–131, 1989.

63. Arnold, D. L., P. M. Matthews, G. Francis, and J. Antel, "Proton magnetic resonance spectroscopy of human brain in vivo in the evaluation of multiple sclerosis: assessment of the load of disease," *Magnetic Resonance in Medicine*, Vol. 14, no. 1, pp. 154–159, 1990.

64. Larsson, H. B., *et al.*, "Localized in vivo proton spectroscopy in the brain of patients with multiple sclerosis," *Magnetic Resonance in Medicine*, Vol. 22, no. 1, pp. 23–31, 1991.

65. Michaelis, T., *et al.*, "Identification of Scyllo-inositol in proton NMR spectra of human brain in vivo," *NMR in Biomedicine*, Vol. 6, no. 1, pp. 105–109, 1993.

66. Viola, A., *et al.*, "High cerebral scyllo-inositol: a new marker of brain metabolism disturbances induced by chronic alcoholism," *Magma (New York, N.Y.)*, Vol. 17, pp. 47–61, sep 2004.

67. Hardy, D. L., and T. J. Norwood, "Spectral editing technique for the in vitro and in vivo detection of taurine," *Journal of Magnetic Resonance (San Diego, Calif. : 1997)*, Vol. 133, no. 1, pp. 70–78, 1998.

68. Kantarci, K., *et al.*, "Regional Metabolic Patterns in Mild Cognitive Impairment and Alzheimer's Disease A 1H MRS Study," *Neurology*, Vol. 55, p. 210, jul 2000.

69. Nelson, S. J., "Assessment of therapeutic response and treatment planning for brain tumors using metabolic and physiological MRI," *NMR in Biomedicine*, Vol. 24, pp. 734–749, jul 2011.

70. Near, J., *et al.*, "Preprocessing, analysis and quantification in single-voxel magnetic resonance spectroscopy: experts' consensus recommendations," *NMR in Biomedicine*, Vol. 34, may 2021.

71. Öz, G., *et al.*, "Advanced single voxel 1 H magnetic resonance spectroscopy techniques in humans: Experts' consensus recommendations," *NMR in Biomedicine*, Vol. 34, may 2020.

72. Wilson, M., and others., "Methodological consensus on clinical proton MRS of the brain: Review and recommendations," *Magnetic Resonance in Medicine*, Vol. 82, pp. 527–550, aug 2019.

73. Ji, B., *et al.*, "Spectral Wavelet-feature Analysis and Classification Assisted Denoising for enhancing magnetic resonance spectroscopy," *NMR in Biomedicine*, Vol. 34, jun 2021.

74. Lei, Y., *et al.*, "Deep learning-based denoising for magnetic resonance spectroscopy signals," *SPIE-Intl Soc Optical Eng*, p. 3, 2021.

75. Provencher, S. W., "Estimation of metabolite concentrations from localized in vivo proton NMR spectra," *Magn Reson Med*, Vol. 30, no. 6, pp. 672–679, 1993.

76. Clarke, W. T., C. J. Stagg, and S. Jbabdi, "FSL-MRS: An end-to-end spectroscopy analysis package," *Magnetic Resonance in Medicine*, Vol. 85, pp. 2950–2964, jun 2021.

77. Oeltzschner, G., *et al.*, "Osprey: Open-source processing, reconstruction estimation of magnetic resonance spectroscopy data," *J Neurosci Methods*, Vol. 343, p. 108827, 2020.

78. Wilson, M., "Spant: An R package for magnetic resonance spectroscopy analysis," *Journal of Open Source Software*, Vol. 6, p. 3646, nov 2021.

79. Edden, R. A., *et al.*, "Gannet: A batch-processing tool for the quantitative analysis of gamma-aminobutyric acid-edited MR spectroscopy spectra," *J Magn Reson Imaging*, Vol. 40, no. 6, pp. 1445–1452, 2014.

80. Purvis, L. A., *et al.*, "OXSA: An open-source magnetic resonance spectroscopy analysis toolbox in MATLAB," *PLOS ONE*, Vol. 12, p. e0185356, sep 2017.

81. Pereira, D. R., L. Ganaha, S. Appenzeller, and L. Rittner, "Open-source toolbox for analysis and spectra quality control of magnetic resonance spectroscopic imaging," *SPIE-Intl Soc Optical Eng*, p. 9, feb 2021.

82. Crane, J. C., M. P. Olson, and S. J. Nelson, "SIVIC: Open-source, standards-based software for DICOM MR spectroscopy workflows," *International Journal of Biomedical Imaging*, Vol. 2013, 2013.

83. Naressi, A., *et al.*, "Java-based graphical user interface for MRUI, a software package for quantitation of in vivo/medical magnetic resonance spectroscopy signals," *Computers in Biology and Medicine*, Vol. 31, no. 4, pp. 269–286, 2001.

84. Poullet, J. B., *et al.*, "An automated quantitation of short echo time MRS spectra in an open source software environment: AQSES," *NMR in Biomedicine*, Vol. 20, pp. 493–504, aug 2007.

85. Simpson, R., *et al.*, "Advanced processing and simulation of MRS data using the FID appliance (FID-A)-An open source, MATLAB-based toolkit," *Magnetic Resonance in Medicine*, Vol. 77, pp. 23–33, jan 2017.

86. Soher, B. J., *et al.*, "VeSPA: Integrated applications for RF pulse design, spectral simulation and MRS data analysis," *J. Magn. Reson, Ser. A*, Vol. 12, no. 2, pp. 75–105, 1994.

87. Reynolds, G., M. Wilson, A. Peet, and T. N. Arvanitis, "An algorithm for the automated quantitation of metabolites in in vitro NMR signals," *Magnetic Resonance in Medicine*, Vol. 56, no. 6, pp. 1211–1219, 2006.

88. Maudsley, A. A., *et al.*, "Comprehensive processing, display and analysis for in vivo MR spectroscopic imaging," *NMR in Biomedicine*, Vol. 19, pp. 492–503, jun 2006.

89. Jiru, F., *et al.*, "jSIPRO - Analysis tool for magnetic resonance spectroscopic imaging," *Computer Methods and Programs in Biomedicine*, Vol. 112, pp. 173–188, oct 2013.

90. Mazziotta, J., *et al.*, "A probabilistic atlas and reference system for the human brain: International Consortium for Brain Mapping (ICBM)," *Philosophical Transactions of the Royal Society of London. Series B: Biological Sciences*, Vol. 356, pp. 1293–1322, aug 2001.

91. Jenkinson, M., *et al.*, "FSL," *NeuroImage*, Vol. 62, pp. 782–790, aug 2012.

92. Smith, S. M., *et al.*, "Advances in functional and structural MR image analysis and implementation as FSL," *Neuroimage*, Vol. 23 Suppl 1, pp. S208–19, 2004.

93. Woolrich, M. W., *et al.*, "Bayesian analysis of neuroimaging data in FSL," *NeuroImage*, Vol. 45, no. 1 Suppl, 2009.

94. Ashburner, J., "SPM: A history," *NeuroImage*, Vol. 62, pp. 791–800, aug 2012.

95. Schaefer, A., *et al.*, "Local-Global Parcellation of the Human Cerebral Cortex from Intrinsic Functional Connectivity MRI," *Cereb Cortex*, Vol. 28, no. 9, pp. 3095–3114, 2018.

96. Aarsland, D., *et al.*, "Prevalence and characteristics of dementia in parkinson disease: An 8-year prospective study," *Archives of Neurology*, Vol. 60, pp. 387–392, 3 2003.

97. Vogt, B. A., "Cingulate cortex in parkinson's disease," *Handbook of clinical neurology*, Vol. 166, pp. 253–266, 1 2019.

98. Arslan, D. B., *et al.*, "The cerebral blood flow deficits in Parkinson's disease with mild cognitive impairment using arterial spin labeling MRI," *J Neural Transm (Vienna)*, Vol. 127, no. 9, pp. 1285–1294, 2020.

99. Akbostanci, M. C., *et al.*, "Turkish Standardization of Movement Disorders Society Unified Parkinson's Disease Rating Scale and Unified Dyskinesia Rating Scale," *Mov Disord Clin Pract*, Vol. 5, no. 1, pp. 54–59, 2018.

100. Mioshi, E., *et al.*, "The Addenbrooke's Cognitive Examination Revised (ACE-R): a brief cognitive test battery for dementia screening," *Int J Geriatr Psychiatry*, Vol. 21, no. 11, pp. 1078–1085, 2006.

101. Folstein, M. F., S. E. Folstein, and P. R. McHugh, ""Mini-mental state". A practical method for grading the cognitive state of patients for the clinician," *J Psychiatr Res*, Vol. 12, no. 3, pp. 189–198, 1975.

102. Stroop, J. R., "Studies of interference in serial verbal reactions.," *Journal of Experimental Psychology.*, Vol. 18, pp. 643–662, 1935.

103. Benton, A. L., K. D. Hamsher, N. R. Varney, and O. Spreen, "Judgment of line orientation," *New York: Oxford University Press*, 1983.

104. Smith, A., "The Symbol-Digit Modalities Test: A Neuropsychologic Test of Learning and Other Cerebral Disorders," *J. Helmuth (Ed.), Learning Disorders, Special Child Publications, Seattle*, pp. 83–91, 1968.

105. Fey, E. T., "The performance of young schizophrenics and young normals on the Wisconsin Card Sorting Test," *J Consult Psychol*, Vol. 15, no. 4, pp. 311–319, 1951.

106. Bengio, Y., A. Courville, and P. Vincent, "Representation learning: a review and new perspectives," *IEEE Transactions on Pattern Analysis and Machine Intelligence*, Vol. 35, no. 8, pp. 1798–1828, 2013.

107. Lecun, Y., Y. Bengio, and G. Hinton, "Deep learning," *Nature 2015 521:7553*, Vol. 521, pp. 436–444, may 2015.

108. Schmidhuber, J., "Deep learning in neural networks: An overview," *Neural Networks*, Vol. 61, pp. 85–117, jan 2015.

109. Pang, S., and X. Yang, "Deep Convolutional Extreme Learning Machine and Its Application in Handwritten Digit Classification," *Computational Intelligence and Neuroscience*, Vol. 2016, 2016.

110. Lawrence, S., C. L. Giles, A. C. Tsoi, and A. D. Back, "Face recognition: A convolutional neural-network approach," *IEEE Transactions on Neural Networks*, Vol. 8, no. 1, pp. 98–113, 1997.

111. Xu, Z., and X. E. Cheng, "Zebrafish tracking using convolutional neural networks," *Scientific Reports 2017 7:1*, Vol. 7, pp. 1–11, feb 2017.

112. Pang, S., Z. Yu, and M. A. Orgun, "A novel end-to-end classifier using domain transferred deep convolutional neural networks for biomedical images," *Computer Methods and Programs in Biomedicine*, Vol. 140, pp. 283–293, mar 2017.

113. Chaudhari, A. S., *et al.*, "Super-resolution musculoskeletal MRI using deep learning," *Magnetic Resonance in Medicine*, Vol. 80, pp. 2139–2154, nov 2018.

114. Dong, C., C. C. Loy, and X. Tang, "Accelerating the super-resolution convolutional neural network," *arXiv:1608.00367*.

115. Ledig, C., *et al.*, "Photo-realistic single image super-resolution using a generative adversarial network," *Proceedings - 30th IEEE Conference on Computer Vision and Pattern Recognition, CVPR 2017*, Vol. 2017-January, pp. 105–114, 9 2016.

116. Dai, T., *et al.*, "Second-order attention network for single image super-resolution," *Proceedings of the IEEE Computer Society Conference on Computer Vision and Pattern Recognition*, Vol. 2019-June, pp. 11057–11066, 6 2019.

117. Zhong, X., *et al.*, "Multi-scale residual network for image classification," *ICASSP, IEEE International Conference on Acoustics, Speech and Signal Processing - Proceedings*, Vol. 2020-May, pp. 2023–2027, 5 2020.

118. Doelken, M. T., *et al.*, "Multi-voxel magnetic resonance spectroscopy at 3 T in patients with idiopathic generalised epilepsy," *Seizure*, Vol. 19, pp. 485–492, oct 2010.

119. Hess, A. T., *et al.*, "A comparison of spectral quality in magnetic resonance spectroscopy data acquired with and without a novel EPI-navigated PRESS sequence in school-aged children with fetal alcohol spectrum disorders," *Metabolic Brain Disease*, Vol. 29, no. 2, pp. 323–332, 2014.

120. Ozturk-Isik, E., and and, "Identification of IDH and TERTp mutation status using 1 H-MRS in 112 hemispheric diffuse gliomas," *Journal of Magnetic Resonance Imaging*, Vol. 51, pp. 1799–1809, jun 2020.

121. Andronesi, O. C., *et al.*, "Imaging Neurochemistry and Brain Structure Tracks Clinical Decline and Mechanisms of ALS in Patients," *Frontiers in Neurology*, Vol. 11, p. 590573, dec 2020.

122. Hangel, G., *et al.*, "Ultra-high resolution brain metabolite mapping at 7 T by short-TR Hadamard-encoded FID-MRSI," *NeuroImage*, Vol. 168, pp. 199–210, mar 2018.

123. Hingerl, L., *et al.*, "Clinical High-Resolution 3D-MR Spectroscopic Imaging of the Human Brain at 7 T," *Investigative Radiology*, Vol. 55, pp. 239–248, apr 2020.

124. Malaspina, D., *et al.*, "Preliminary Findings Associate Hippocampal 1 H-MR Spectroscopic Metabolite Concentrations with Psychotic and Manic Symptoms in Patients with Schizophrenia," *American Journal of Neuroradiology*, Vol. 42, pp. 88–93, jan 2021.

125. Parikh, J., *et al.*, "Proton spectroscopic imaging of brain metabolites in basal ganglia of healthy older adults," *Magma (New York, N.Y.)*, Vol. 28, pp. 251–257, jun 2015.

126. Solanky, B. S., *et al.*, "NAA is a Marker of Disability in Secondary-Progressive MS: A Proton MR Spectroscopic Imaging Study," *American Journal of Neuroradiology*, Vol. 41, pp. 2209–2218, dec 2020.

127. McCarthy, P., "Fsleyes," *Zenodo*, 2021.

128. Rorden, C., H. O. Karnath, and L. Bonilha, "Improving lesion-symptom mapping," *Journal of Cognitive Neuroscience*, Vol. 19, pp. 1081–1088, jul 2007.

129. Brett, M., *et al.*, "nibabel: 2.1.0," *Zenodo*, dec 2019.

130. Bonekamp, D., *et al.*, "Fast method for brain image segmentation: Application to proton magnetic resonance spectroscopic imaging," *Magnetic Resonance in Medicine*, Vol. 54, pp. 1268–1272, nov 2005.

131. Degaonkar, M. N., M. G. Pomper, and P. B. Barker, "Quantitative proton magnetic resonance spectroscopic imaging: regional variations in the corpus callosum and cortical gray matter," *Journal of Magnetic Resonance Imaging*, Vol. 22, pp. 175–179, aug 2005.

132. Horská, A., V. D. Calhoun, D. H. Bradshaw, and P. B. Barker, "Rapid method for correction of CSF partial volume in quantitative proton MR spectroscopic imaging," *Magn Reson Med*, Vol. 48, no. 3, pp. 555–558, 2002.

133. Tal, A., I. I. Kirov, R. I. Grossman, and O. Gonen, "The role of gray and white matter segmentation in quantitative proton MR spectroscopic imaging," *NMR in Biomedicine*, Vol. 25, pp. 1392–1400, dec 2012.

134. Bhogal, A. A., *et al.*, "Lipid-suppressed and tissue-fraction corrected metabolic distributions in human central brain structures using 2D 1 H magnetic resonance spectroscopic imaging at 7 T," *Brain and Behavior*, Vol. 10, dec 2020.

135. Dong, Z., W. Dreher, D. Leibfritz, and B. S. Peterson, "Challenges of using MR spectroscopy to detect neural progenitor cells in vivo," *American Journal of Neuroradiology*, Vol. 30, pp. 1096–1101, jun 2009.

136. Kreis, R., "The trouble with quality filtering based on relative Cramér-Rao lower bounds," *Magnetic Resonance in Medicine*, Vol. 75, pp. 15–18, jan 2016.

137. Yeo, B. T., *et al.*, "The organization of the human cerebral cortex estimated by intrinsic functional connectivity," *J Neurophysiol*, Vol. 106, no. 3, pp. 1125–1165, 2011.

138. Hughes, A. J., S. E. Daniel, L. Kilford, and A. J. Lees, "Accuracy of clinical diagnosis of idiopathic Parkinson's disease: a clinico-pathological study of 100 cases," *J Neurol Neurosurg Psychiatry*, Vol. 55, no. 3, pp. 181–184, 1992.

139. Litvan, I., *et al.*, "Diagnostic criteria for mild cognitive impairment in Parkinson's disease: Movement Disorder Society Task Force guidelines," *Mov Disord*, Vol. 27, no. 3, pp. 349–356, 2012.

140. Uysal-Canturk, P., *et al.*, "An assessment of Movement Disorder Society Task Force diagnostic criteria for mild cognitive impairment in Parkinson's disease," *Eur J Neurol*, Vol. 25, no. 1, pp. 148–153, 2018.

141. Shader, R. I., J. S. Harmatz, and C. Salzman, "A new scale for clinical assessment in geriatric populations: Sandoz Clinical Assessment–Geriatric (SCAG)," *J Am Geriatr Soc*, Vol. 22, no. 3, pp. 107–113, 1974.

142. Nasreddine, Z. S., *et al.*, "The Montreal Cognitive Assessment, MoCA: a brief screening tool for mild cognitive impairment," *J Am Geriatr Soc*, Vol. 53, no. 4, pp. 695–699, 2005.

143. Smith, S. M., "Fast robust automated brain extraction," *Hum Brain Mapp*, Vol. 17, no. 3, pp. 143–155, 2002.

144. Jenkinson, M., P. Bannister, J. M. Brady, and S. M. Smith, "Improved Optimisation for the Robust and Accurate Linear Registration and Motion Correction of Brain Images.," *Neuroimage*, Vol. 17(2), pp. 825–841, 2002.

145. Kamagata, K., *et al.*, "Posterior hypoperfusion in Parkinson's disease with and without dementia measured with arterial spin labeling MRI," *Journal of Magnetic Resonance Imaging*, Vol. 33, pp. 803–807, apr 2011.

146. Syrimi, Z. J., *et al.*, "Arterial spin labelling detects posterior cortical hypoperfusion in non-demented patients with Parkinson's disease," *Journal of Neural Transmission*, Vol. 124, pp. 551–557, may 2017.

147. Guan, J., *et al.*, "Detection and application of neurochemical profile by multiple regional (1)H-MRS in Parkinson's disease," *Brain Behav*, Vol. 7, no. 9, p. e00792, 2017.

148. Almuqbel, M., and others., "Metabolite ratios in the posterior cingulate cortex do not track cognitive decline in Parkinson's disease in a clinical setting," *Parkinsonism Relat Disord*, Vol. 22, pp. 54–61, 2016.

149. Seeley, W. W., *et al.*, "Dissociable Intrinsic Connectivity Networks for Salience Processing and Executive Control," *The Journal of Neuroscience*, Vol. 27, p. 2349, feb 2007.

150. Dosenbach, N. U., *et al.*, "Distinct brain networks for adaptive and stable task control in humans," *Proceedings of the National Academy of Sciences of the United States of America*, Vol. 104, p. 11073, jun 2007.

151. Anderson, D. E., D. A. Ghate, and M. Rizzo, "Vision, attention, and driving," *Handbook of Clinical Neurology*, Vol. 178, pp. 337–360, jan 2021.

152. Uddin, L. Q., *Salience Network of the Human Brain*, Elsevier Inc., aug 2016.

153. Norman, L. J., *et al.*, "Error-processing and inhibitory control in obsessive-compulsive disorder: a meta-analysis using statistical parametric maps," *Biological Psychiatry*, Vol. 85, p. 713, may 2019.

154. Van Eimeren, T., *et al.*, "Drug-induced deactivation of inhibitory networks predicts pathological gambling in PD," *Neurology*, Vol. 75, no. 19, pp. 1711–1716, 2010.

155. Buckner, R. L., J. R. Andrews-Hanna, and D. L. Schacter, "The brain's default network: anatomy, function, and relevance to disease," *Ann N Y Acad Sci*, Vol. 1124, pp. 1–38, 2008.

156. Raichle, M. E., "The brain's default mode network," *Annu Rev Neurosci*, Vol. 38, pp. 433–447, 2015.

157. Li, W., *et al.*, "Neurometabolic and functional changes of default-mode network relate to clinical recovery in first-episode psychosis patients: A longitudinal 1H-MRS and fMRI study," *NeuroImage: Clinical*, Vol. 34, p. 102970, jan 2022.

158. Voevodskaya, O., *et al.*, "Myo-inositol changes precede amyloid pathology and relate to APOE genotype in Alzheimer disease," *Neurology*, Vol. 86, pp. 1754–1761, may 2016.

159. Oeltzschner, G., *et al.*, "Neurometabolites and associations with cognitive deficits in mild cognitive impairment: a magnetic resonance spectroscopy study at 7 Tesla," *Neurobiol Aging*, Vol. 73, pp. 211–218, 2019.

160. Diez-Cirarda, M., *et al.*, "Dynamic functional connectivity in Parkinson's disease patients with mild cognitive impairment and normal cognition," *Neuroimage Clin*, Vol. 17, pp. 847–855, 2018.

161. Yau, Y., *et al.*, "Network connectivity determines cortical thinning in early Parkinson's disease progression," *Nat Commun*, Vol. 9, no. 1, p. 12, 2018.

162. Wolpert, D. H., "The relationship between pac, the statistical physics framework, the bayesian framework, and the vc framework," *The Mathematics of Generalization*, pp. 117–214, 10 2018.

163. Cox, S. R., *et al.*, "Associations between education and brain structure at age 73 years, adjusted for age 11 IQ," *Neurology*, Vol. 87, no. 17, pp. 1820–1826, 2016.

164. Park, Y. W., *et al.*, "AutoVOI: real-time automatic prescription of volume-of-interest for single voxel spectroscopy," *Magn Reson Med*, Vol. 80, no. 5, pp. 1787–1798, 2018.

165. Nelson, S. J., *et al.*, "Strategies for rapid in vivo 1H and hyperpolarized 13C MR spectroscopic imaging," *Journal of Magnetic Resonance*, Vol. 229, pp. 187–197, apr 2013.

166. Jia, Y., *et al.*, "Caffe: Convolutional architecture for fast feature embedding," in *Proceedings of the 22nd ACM International Conference on Multimedia*, MM '14, (New York, NY, USA), pp. 675–678, Association for Computing Machinery, 2014.

167. Nair, V., and G. E. Hinton, "Rectified linear units improve restricted boltzmann machines," in *Proceedings of the 27th International Conference on International Conference on Machine Learning*, ICML'10, (Madison, WI, USA), p. 807âĂŞ814, Omnipress, 2010.

168. Valdes, M. D. C., and M. Inamura, "Improvement of remotely sensed low spatial resolution images by back-propagated neural networks using data fusion techniques," *International Journal of Remote Sensing*, Vol. 22, no. 4, pp. 629–642, 2001.